Quantitative Acoustic Emission during Additive Manufacturing and Frictional Behavior of Heterogeneous Interfaces

A Dissertation

Presented to the Faculty of the Graduate School

of Cornell University

In Partial Fulfillment of the Requirements for the Degree of

Doctor of Philosophy

by

Jun Young Song

December 2025

Quantitative Acoustic Emission during Additive Manufacturing and Frictional Behavior of Heterogeneous Interfaces

Jun Young Song, Ph. D.

Cornell University 2025

This dissertation investigates acoustic emission (AE) monitoring as a unified framework for characterizing failure processes across material systems and scales. Through controlled laboratory experiments of additive manufacturing and laboratory earthquake experiments, AE sensors are shown to distinguish between slow and rapid stress transfer processes, enabling signal identification, quantification, and localization.

In additive manufacturing, AE monitoring differentiated tensile cracking from thermal expansion and powder effects, while porosity produced no detectable signals during laser spot welding. Using a calibration technique that uses a ball impact as a reference source, estimated crack sizes agreed with observations from scanning electron microscope images.

Laboratory earthquake experiments investigated frictional heterogeneity using meter-scale Polymethyl methacrylate (PMMA) blocks in a biaxial testing machine. On frictionally heterogeneous faults, velocity-weakening (VW) regions with bare PMMA surfaces produced seismic slip, whereas velocity-strengthening (VS) regions coated with Teflon tape exhibited stable, aseismic slip. A single VW patch surrounded by VS regions exhibited systematic transitions: aseismic slip, periodic slip, and non-periodic

slip, as identified through AE sensors.

To create a more heterogeneous and realistic fault system, multiple VW patches separated by VS barriers were implemented. This fault configuration produced complex seismicity including foreshocks, mainshocks, and aftershocks. Varying the loading rate illuminated an inverse trend to fault healing (i.e., an increase in seismic magnitude over time) due to variations in VS barrier effectiveness with loading rate. Foreshock sequences, identified from the hypocenters determined by AE signals, and quasi-dynamic earthquake simulations both exhibited bidirectional migration with back-propagation velocities about ten times faster than the main propagation velocity, resembling Rapid Tremor Reversals in subduction zones.

Fluid injection experiments using Teflon tape to confine flow revealed two migration mechanisms: pressure-diffusion-driven migration at slow injection rate or low-viscosity fluid, and volume-driven migration at fast injection rate or high-viscosity fluid. Poroelastic modeling reproduced experimental observations by coupling pressure-dependent permeability with fault opening.

Together, these results demonstrate AE monitoring's capability to bridge material science and geophysics, providing insights into failure mechanisms from microstructural defects to earthquake dynamics across vastly different temporal and spatial scales.

BIOGRAPHICAL SKETCH

Jun Young Song was born and raised in Seoul, South Korea. He received his B.S. and M.S. degrees in Civil and Environmental Engineering from Yonsei University, specializing in Geotechnical Engineering. During his undergraduate studies, he served in the Republic of Korea Army as an information operations soldier. Following the completion of his master's degree, he worked as a geophysical researcher at the Korea Polar Research Institute, where he participated in the 7th overwintering team at Jang Bogo Station in Antarctica. His experience studying seismic activity in Antarctica inspired his growing interest in earthquake processes, leading him to pursue a Ph.D. in Civil and Environmental Engineering at Cornell University, focusing on earthquake mechanics. Upon completion of his Ph.D., he will begin a Postdoctoral Fellow position in the Department of Civil and Environmental Engineering at the Colorado School of Mines.

ACKNOWLEDGEMENTS

I would like to express my deepest gratitude to my advisor, Prof. Gregory McLaskey. I used to rely heavily on others in conducting research, but under your guidance, I have become a much more independent researcher. Your passion for understanding earthquakes has inspired me to tackle meaningful scientific questions, and your high academic standards have motivated me to hold myself to the same level of excellence, which has greatly improved my writing and research. I will carry these lessons throughout my career. I would also like to thank my committee members, Prof. Patrick Fulton and Prof. Atieh Moridi, for their time and guidance as committee members, as well as for the insightful courses that greatly benefited my research.

I am grateful to my research collaborators, Prof. Camilla Cattania and Yudong Sun at MIT for their contributions to the earthquake simulation, and Prof. Chloe Arson and Dr. Lingfu Liu at Cornell University for their work on the poroelastic simulation collaborations. These simulations provided a comprehensive understanding of the experimental results and greatly enhanced the quality of our research papers.

To my research group colleagues – Dr. Sara Beth Cebry, Dibya Jyoti Basu, Joseph Van Linn, Sunny Yang, Youngjin Yang, and Han Chen – I am deeply grateful for your research insights, collaboration, and constructive feedback during group meetings, all of which have greatly enriched my understanding of earthquake mechanics.

For the colleagues I met at Cornell – Lyn Zemberekci, Swati Gupta, Yan-Ning Kuo, Joey Ryu, Woojeong Kim, Kyuseong Choi, Taesuh Kim, Yongjun Kim, Yuseok Kim,

Kyungmin Kim, and Anna Choi – thank you for hanging out with me and providing your support throughout my Ph.D.

I am also grateful to Jim Strait and all the members of the Bovay Lab. Your willingness to share your expertise and provide hands-on support with experiments greatly enriched my research at Cornell.

Finally, I wish to thank my parents, Dr. Dong-Seob Song and Gumsook Tak, for their unconditional support of my career and of my life.

TABLE OF CONTENTS

LIST OF FIGURES

LIST OF TABLES

CHAPTER 1

Introduction

1.1. Overview

The Acoustic Emission (AE) technique is a powerful nondestructive testing (NDT) and monitoring method that detects the transient elastic waves generated by rapid material processes (Grosse & Ohtsu, 2008). Its real-time monitoring potential and non-destructive nature further enhance its utility across a wide range of applications, from engineered materials to structural and geophysical systems. For example, it is commonly employed to detect and track damage progression (Barile et al., 2019), monitor the health of infrastructure (Balageas et al., 2010), investigate geotechnical and geological processes (Michlmayr et al., 2012), identify leaks in pressurized systems (Miller et al., 1999), and evaluate fatigue and fracture behavior (Noorsuhada, 2016).

To understand how the AE technique achieves this wide range of monitoring capabilities, it is essential to examine the sensors that make the technique possible. The AE sensors include the piezoelectric element in protective housing (Beattie, 1983). The piezoelectric element is a ceramic material (e.g., barium titanate or lead zirconate titanate) whose microscopic domains are aligned through a poling process, giving it a net polarity (Jaffe, 1958). This piezoelectric element converts mechanical stress into electric charge (direct effect) and deforms when an electric field is applied (converse effect), allowing it to function as both a sensor and an actuator.

AE sensors capture stress-induced electric signals caused by external forces, stress

redistribution, or changes in displacement or volume. Analysis of the frequency spectrum of these AE signals reflects the fundamental distinction between slow and rapid processes. Rapid processes generate broad-frequency spectra with significant high-frequency components, as the sharp temporal changes in stress create waves with fast rise times. In contrast, slow processes, when they do generate any detectable signals, produce predominantly low-frequency components that are often masked by ambient noise and fall outside the optimal sensitivity range of conventional AE sensors. The distinction between high- and low-frequency AE signals depends on the type of sensors employed. In laboratory experiments, AE sensors are typically designed to capture signals in the range of tens of kHz to several MHz, whereas field AE sensors usually cover a frequency range from about 1 Hz to several kHz, reflecting the different scales and characteristics of the observed processes.

However, not all material processes generate detectable AE signals. Slower motion that involves gradual, quasi-static stress changes that occur over extended time periods, including creep deformation (Neighbour & McEnaney, 1994; Xu et al., 2025), thermal expansion (Griffiths et al., 2024; Zhang et al., 2023), plastic flow (Louda et al., 2022), and stable sliding in frictional interface (Scuderi et al., 2016). While these processes may involve significant total energy changes, stress waves may be too weak or in such a low frequency range that they are not detectable.

This frequency-based distinction leads to the inherent selectivity of AE sensors for impulsive events, which enables discrimination between different types of material processes based on their temporal characteristics and stress release mechanisms.

This dissertation uses AE sensors during the additive manufacturing of metallic

materials to identify distinct signal types by linking physical events with their corresponding acoustic signals. AE sensors are also applied to investigate the slip behavior of frictionally heterogeneous faults, including Velocity-Weakening (VW) regions that promote seismic slip and Velocity-Strengthening (VS) regions that promote aseismic, stable sliding.

1.2. Objectives

The AE technique is a powerful tool for monitoring material responses, yet interpreting AE signals across different systems remains challenging due to the complex coupling between underlying physical source processes and the AE signals. To address this challenge, this study focuses on characterizing AE signals for identifying events, quantifying their sizes, and localizing their sources in additive manufacturing and laboratory earthquakes. Both applications exhibit a common phenomenon where material behavior transitions between stable, continuous processes and sudden, energetic failure events.

1. **Signal Identification:** Distinguish different types of events based on the detected signals, including detectable events such as cracks in additive manufacturing or slow- and fast-slip events in laboratory earthquakes, and non-detectable events such as pores in additive manufacturing or aseismic slip in laboratory earthquakes.
2. **Signal Quantification:** Analyze and quantify signals which can be used to estimate crack sizes in additive manufacturing and determining event magnitudes in laboratory earthquakes.

3. **Event Localization:** Identify the locations of defects in additive manufacturing and the hypocenters of seismic events in laboratory earthquakes, as well as track the migration of seismicity over time.

The successful completion of these objectives will demonstrate the potential of a unified AE analysis approach to provide comprehensive insights into failure mechanisms across vastly different material systems and temporal scales.

1.3. Outline of Chapters

The structure of this dissertation is organized into six chapters, which are briefly outlined below:

Chapter 2: Detection of Defects during Laser-Powder Interaction by Acoustic Emission Sensors and Signal Characteristics

This chapter investigates the use of AE sensors to monitor material responses during additive manufacturing. This study links AE signals to underlying physical processes, enabling the identification of different mechanisms such as cracking, material interaction, and thermal effects. The approach demonstrates how signal characteristics can provide insights into defect formation and establishes a method for quantitative evaluation of the physical crack size and validation of AE-based monitoring techniques.

Chapter 3: Laboratory Earthquake Ruptures Contained by Velocity Strengthening Fault Patches

This chapter examines the slip behavior of a single VW patch with surrounding VS regions, a conceptual approach commonly used in numerical earthquake simulations.

Laboratory experiments were designed to replicate this configuration and explore the conditions controlling slip behavior. The study demonstrates systematic transitions from stable to unstable slip depending on the length of the VW asperity and normal stress, highlighting the critical role of VS surroundings in modulating rupture dynamics and providing experimental validation for theoretical models of fault behavior.

Chapter 4: Fault Healing and Asperity Partitioning on a Frictionally Heterogeneous Laboratory Fault

This chapter explores the slip behavior of faults with multiple VW patches separated by VS regions, reflecting the heterogeneous nature of natural faults. The experiments reveal that complex patch distributions give rise to seismic clustering, including foreshocks and aftershocks, which are not observed on a fault with a single VW patch. Variations in loading rate highlight the role of VS barriers in modulating interactions between VW patches. The observed sequences, which share similarities with foreshock activity in subduction zones, are reinforced by numerical modeling and provide insight into the dynamics of heterogeneous fault systems.

Chapter 5: Seismicity Migration from Fluid Injection: Laboratory Experiments and Numerical Models Illuminate Volume-Driven versus Pressure-Diffusion-Driven Migration

This chapter investigates how fluid injection can reactivate shear faults under controlled laboratory conditions. By sealing fault edges with Teflon tape, fluid pressure was able to propagate along the fault interface without leakage, enabling the study of different seismicity migration patterns. The experiments demonstrate that

injection rate and fluid viscosity govern the patterns of seismic migration, with numerical simulations reproducing the observed behaviors and providing a basis for optimizing fluid injection strategies.

Chapter 6: Conclusion

Summary of the research in this dissertation.

REFERENCES

Balageas, D., Fritzen, C. P., & Güemes, A. (2010). *Structural Health Monitoring* (Vol. 90). John Wiley & Sons. https://doi.org/L-572093-6190484b7c

Barile, C., Casavola, C., Pappalettera, G., & Vimalathithan, P. K. (2019). Damage characterization in composite materials using acoustic emission signal-based and parameter-based data. *Composites Part B: Engineering*, *178*(September), 107469. https://doi.org/10.1016/j.compositesb.2019.107469

Beattie, A. G. (1983). Acoustic emission, principles and instrumentation (No. SAND-82-2825). Sandia National Labs., Albuquerque, NM (USA).

Dass, A., Gabourel, A., Pagan, D., & Moridi, A. (2022). Laser based directed energy deposition system for operando synchrotron x-ray experiments. *Review of Scientific Instruments*, *93*(7). https://doi.org/10.1063/5.0081186

Griffiths, L., Heap, M. J., Lengliné, O., Baud, P., Schmittbuhl, J., & Gilg, H. A. (2024). Thermal Stressing of Volcanic Rock: Microcracking and Crack Closure Monitored Through Acoustic Emission, Ultrasonic Velocity, and Thermal Expansion. *Journal of Geophysical Research: Solid Earth*, *129*(3). https://doi.org/10.1029/2023JB027766

Grosse, C. U., & Ohtsu, M. (2008). *Acoustic Emission Testing*. (C. Grosse & M. Ohtsu, Eds.). Berlin, Heidelberg: Springer Berlin Heidelberg. https://doi.org/10.1007/978-3-540-69972-9

Jaffe, H. (1958). Piezoelectric Ceramics. *Journal of the American Ceramic Society*, *41*(11), 494–498. https://doi.org/10.1111/j.1151-2916.1958.tb12903.x

Louda, P., Sharko, A., Stepanchikov, D., & Sharko, A. (2022). Experimental and Theoretical Study of Plastic Deformation of Epoxy Coatings on Metal Substrates Using the Acoustic Emission Method. *Materials*, *15*(11). https://doi.org/10.3390/ma15113791

Michlmayr, G., Cohen, D., & Or, D. (2012). Sources and characteristics of acoustic emissions from mechanically stressed geologic granular media - A review. *Earth-Science Reviews*, *112*(3–4), 97–114. https://doi.org/10.1016/j.earscirev.2012.02.009

Miller, R. K., Pollock, A. A., Watts, D. J., Carlyle, J. M., Tafuri, A. N., & Yezzi, J. J. (1999). A reference standard for the development of acoustic emission pipeline leak detection techniques. *NDT and E International*, *32*(1), 1–8. https://doi.org/10.1016/S0963-8695(98)00034-6

Neighbour, G. B., & McEnaney, B. (1994). Creep and recovery in graphites at ambient temperature: An acoustic emission study. *Carbon*, *32*(4), 553–558. https://doi.org/10.1016/0008-6223(94)90071-X

Noorsuhada, M. N. (2016). An overview on fatigue damage assessment of reinforced concrete structures with the aid of acoustic emission technique. *Construction and Building Materials*, *112*, 424–439. https://doi.org/10.1016/j.conbuildmat.2016.02.206

Scuderi, M. M., Marone, C., Tinti, E., Di Stefano, G., & Collettini, C. (2016). Precursory changes in seismic velocity for the spectrum of earthquake failure modes. *Nature Geoscience*, *9*(9), 695–700. https://doi.org/10.1038/ngeo2775

Xu, C., Khan, M., Daly, M., Gonzalez Nunez, M., & Ozevin, D. (2025). Detecting secondary to tertiary creep transitions by acoustic emission. *Measurement: Journal of the International Measurement Confederation*, *255*(May), 118096. https://doi.org/10.1016/j.measurement.2025.118096

Zhang, C., Feng, Z., Mi, C., Chen, Z., Geng, H., & Shen, C. (2023). Experimental study on acoustic emission characteristics of high temperature thermal shock directional fracturing of granite with different heating conditions. *Engineering Fracture Mechanics*, *289*(April), 109427. https://doi.org/10.1016/j.engfracmech.2023.109427

CHAPTER 2

Detection of Defects during Laser-Powder Interaction by Acoustic Emission Sensors and Signal Characteristics

This chapter is drawn from the peer-reviewed journal paper: *Song, J.Y., Dass, A., Moridi, A. and McLaskey, G.C., 2024. Detection of defects during laser-powder interaction by acoustic emission sensors and signal characteristics. Additive Manufacturing, 82, p.104035. https://doi.org/10.1016/j.addma.2024.104035*

2.1. Abstract

Acoustic Emission (AE) is an in-situ real-time nondestructive monitoring method proposed for Additive Manufacturing (AM) to detect defects such as cracks. Previous AE research in AM mainly focused on developing algorithms to automatically detect the defects from AE signals without understanding the physical mechanisms or the signal characteristics that could be used as identifiers. We study AE signals during a laser spot welding on a powder to clearly distinguish between different physical mechanisms using their signal characteristics. We identified specific signals associated with 1) tensile cracks from cooling, 2) a powder effect on the substrate, and 3) sudden thermal expansion of the substrate. We used the spectral ratio between high frequency (70 - 150 kHz) and low frequency (10 - 40 kHz) spectral amplitudes in the frequency domain to classify and differentiate the source types. We found that porosity due to insufficient energy density did not produce detectable AE signals. Using a ball drop calibration technique, we used AE signals to estimate the absolute sizes of the tensile

cracks. Crack sizes ranged from 40 μm to 1 mm and were in general agreement with scanning electron microscope images of the fractures. We performed a line scanning test and successfully validated its potential for the application. Our findings provide a basic understanding of AE signal characteristics in AM, as well as the practical parameters used to separate the signal types.

2.2. Introduction

Additive manufacturing (AM) is of interest to aerospace, automotive, and biomedical industries (Alipour et al., 2022; Caiazzo et al., 2013; Das et al., 1999; Dass et al., 2022; Gu et al., 2012; Mazumder et al., 1999; Yan et al., 2015; B. Zhang et al., 2017; L. C. Zhang et al., 2011) due to its advantages such as manufacturing complex geometries that cannot easily be made by traditional methods, saving energy and costs, reducing environmental impact, and expediting manufacturing time (Brandt et al., 2013). However, the quality of AM processing can vary as a function of laser energy, laser scan speed, hatch spacing, powder material, and thickness of the powder bed. If these parameters are not optimized, various types of defects can occur such as 1) keyhole porosity due to instability of the melt pool, 2) lack of fusion defects due to insufficient laser energy density, and 3) solidification cracks (B. Zhang et al., 2017). These defects lead to low quality of manufacturing (Gong et al., 2015; Liu et al., 2014), so many studies have been focused on the detection and suppression of defects for high mechanical performance of the printed material.

Acoustic Emission (AE) testing has been proposed as in-situ real-time nondestructive method for defect detection (Holford et al., 2017; Lu & Wong, 2018; McCann et al.,

2021). As described schematically in Figure 2.1, damage sources such as the sudden propagation of a crack can cause a rapid reorganization of the internal stress of the material. This causes the radiation of elastic waves and kHz-frequency vibrations that are detected with sensors and analyzed (Lu & Wong, 2018). Vibrations due to AEs are typically measured with piezoelectric sensors directly coupled or glued to the sample or substrate. Non-contact laser interferometers can also detect AEs (Enoki et al., 2000) and a fraction of the AE vibrations also travel through air and might be detected by a microphone or with the human ear (Ye et al., 2018) but those are far less sensitive than contact measurements.

Previous studies proposed using AE signal analysis to classify defects such as balling and spatter (Ye et al., 2018; Zhirnov & Kouprianoff, 2022), estimate the density of printed material (Eschner et al., 2020), or detect signals associated with keyholing (Seleznev et al., 2022; Tempelman et al., 2022). Some studies compared AE results to X-ray computed tomography (XCT) images (Seleznev et al., 2022; Wasmer et al., 2019) or cross section images (Ito et al., 2021). Most of these studies employed machine learning methods to relate continuously recorded AE signals to manufacturing quality and did not focus on the physics of how specific defects could create characteristic AE signals.

In this study, we isolated different mechanisms that produce AEs in an AM environment using simple experiments where defects such as tensile fracture and pores due to insufficient energy density could be unambiguously separated. Our methods do not replicate current industrial processes; they are a steppingstone toward better understanding the sources and signatures of AEs associated with Laser-powder

interaction. Our line scan experiments produced a variety of different signals, described in more detail in Section 2.6.5, but to further simplify the experiment, we conducted spot welds using SS304 and Ti-6Al-4V powders and used Scanning Electron Microscope (SEM) images of the cross sections to link the different recorded AE signals to visually observed defects. First, a ball drop calibration test was conducted as an absolute reference, and this allowed us to roughly estimate the seismic moment of the AE signals (a measure of the signal's amplitude at low frequencies) which was then used to estimate the physical sizes of the cracks. We also defined time-domain and frequency-domain parameters that were used to discriminate between signals due to tensile fracture from those associated with thermal expansion or powder effect. The spot weld experiments are the primary topic of this paper, but we also discuss how insights gained can be utilized for monitoring of experimental conditions that are more representative of industrial processes.

2.3. Background on the method of acoustic emission

Acoustic emission signals are recordings of kHz - MHz vibrations generated by rapidly varying forces acting on the surface or interior of a solid (i.e., from sudden crack propagation, ballistic impact, rapid thermal expansion, and other sources). Figure 2.1 shows a schematic diagram of an AE signal detected in an AM setting. The AE source, shown as an orange star, is a sudden and localized reorganization of stresses, such as due to the sudden propagation of a microcrack. Elastic waves radiate away from the source location in all directions, reflect off of free surfaces, and cause high frequency surface motions (vibrations) that can be detected by a piezoelectric

sensor directly coupled to the metal substrate. The direct arrivals, shown as blue dashed arrows in Figure 2.1b and the signals with blue background in Figure 2.1d, are the first to be detected by the sensor and contain the most undistorted information about the source. Later arriving reflections, shown as red dashed arrows and red background, also contain information about the source, but are more heavily influenced by the medium through which the waves propagated. Common sources of AE are at most a few μs in duration (Grosse & Ohtsu, 2008), but the elastic waves generated by AE sources can reflect and refract within the solid thousands of times (i.e. for a few ms) before they naturally decay in amplitude due to intrinsic attenuation in the material (grey background in Figure 2.1d). The direct analysis of AE signals can be quite challenging due to the overlap of direct arrivals, Rayleigh waves, and reflected waves; however, the mathematical framework described below and the ball drop calibration source, described in Section 2.4.3, allows us to quantify the source of the AE signals, despite complications associated with wave propagation.

The processes of AE source generation, wave propagation, and signal recording can be modeled as a set of linear and time invariant systems (Eitzen & Breckenridge, 1987; Hsu & Breckenridge, 1981; McLaskey & Glaser, 2012). This framework can be helpful for the inverse problem of characterizing the AE source mechanisms based on recorded signals. We utilize this framework to describe how the AE recording system was absolutely calibrated and how a ball impact source was used to quantify the magnitude of the AE sources, and the physical size of the tensile cracks that cause the AE signals.

As shown schematically in Figure 2.1, the signal recorded from an AE sensor, s(x, t),

can be expressed as the convolution of a source function, a wave propagation function, and an instrument response function. Sources that act on the external surfaces of a body are typically represented by a force vector f_j. In this case,

$$s(x, t) = f_j(\xi, \tau) \otimes G_{kj}(x, t; \xi, \tau) \otimes i_k(t) \quad (2.1)$$

where $\otimes$ is convolution in time, $G_{kj}(x, t; \xi, \tau)$ is the elastodynamic Green's function that describes how forces in the location ξ at time τ, produce vibrations (displacements) at location x and time t (Aki & Richards, 1980; McLaskey & Glaser, 2012), and $i_k(t)$ is the instrument response function that describes how a sensor converts a surface displacement vector into a scalar signal and also includes any distortions associated with frequency bandwidth limitations of the sensors, preamp, and digitizer.

Alternatively, sources that occur inside a body such as cracks and earthquakes impart no net linear moment and are typically represented with a moment tensor M_{jl} whose components are force couples acting with opposite sign in the j direction and separated by a distance in the l direction. In this case,

$$s(x, t) = M_{jl}(\xi, \tau) \otimes G_{kj,l}(x, t; \xi, \tau) \otimes i_k(t) \quad (2.2)$$

where $G_{kj,l}(x, t; \xi, \tau)$ is the first spatial derivative of the Green's function in the l direction.

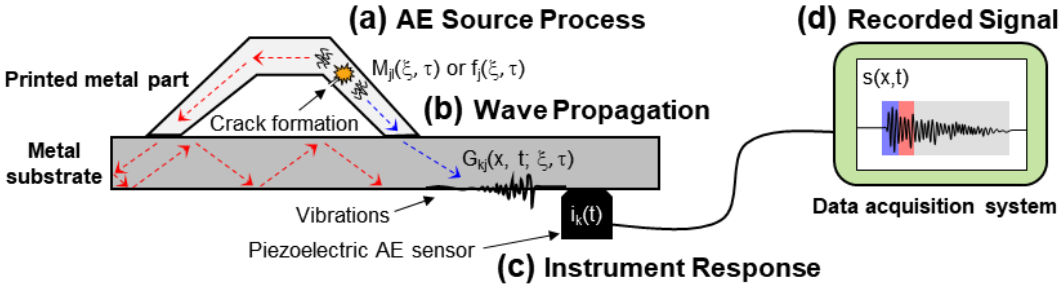

Figure 2.1. Schematic diagram of example AE monitoring of a printed part on a metal substrate. (a) The AE source process is exemplified by a tensile crack (orange star), $M_{jl}(\xi, \tau)$, which radiates elastic waves. (b) Wave propagation in the part and substrate is modeled with an elastodynamic Green's function $G_{kj}(x, t; \xi, \tau)$. (c) Piezoelectric sensors convert high frequency vibrations of the surface of the specimen into electrical signals, and this process is represented with an instrument response function $i_k(t)$. (d) Recorded digitized signals are the result of source processes, wave propagation effects, and instrument response (see text).

2.4. Materials and Methods

2.4.1. Experimental setup for AM

The experimental setup for the custom AM system is shown schematically in Figure 2.2, built at the Laboratory of Advanced Materials and Manufacturing at Cornell University detailed in Dass et al. (Dass, 2020; Dass et al., 2022). The system is equipped with a 500 W continuous wave laser from IPG Photonics (Model: YLR-MM-AC-500), 500 μm spot size, and 1070 nm wavelength. The laser's working distance to focus on the top of the powder was 207.7 mm. The chamber was made of a steel box (152.4 mm by 152.4 mm by 120.65 mm), which contained a UV-fused silica window at the top to ensure that the laser wavelength passed through the chamber. The chamber was purged with Argon gas to maintain an inert atmosphere during printing.

A Stainless steel (SS304) substrate with dimensions 101.6 mm by 69 mm by 12.7 mm in the x, y, and z directions, respectively, rested on top of four metallic supports (Figure 2.2). Four piezoelectric AE sensors (Panametrics V103, 12.7 mm diameter)

were attached to the bottom of the substrate using standard hot glue (Stanley Dualmelt, melting temperature ~135 °C). Sensors were still firmly attached to the substrate after the experiment. This indicated that the hot glue maintained its integrity. Some early experiments were conducted using vacuum grease as a couplant with similar results.) Sensors were connected to preamplifiers (Panametrics) with 40 dB gain and 10 kHz to 1 MHz bandwidth. The signals from the sensors were continuously recorded at 10 kHz (low-rate signal) and were simultaneously recorded in a triggered mode where 6 ms-long blocks of data were recorded at 10 MHz (high-rate, triggered signal) when the amplitude of the signal exceeded a specific threshold (above the noise level).

SEM images were obtained for an internal examination of the welded spots after the tests. The cross section of the printed spot was prepared following standard metallographic procedures: grinding and polishing up to 0.05 μm colloidal silica to remove surface imperfections. Then, the polished Back-Scattered Electron (BSE) image was taken using the Tescan Mira3 SEM machine.

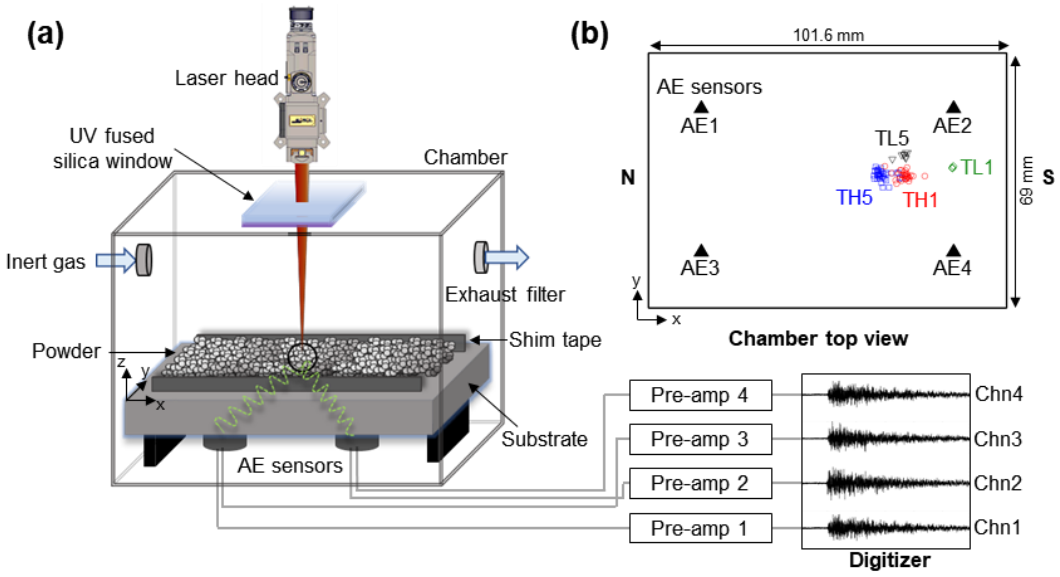

Figure 2.2. (a) Schematic diagram of custom AM experimental setup with AE monitoring. (b) Top view of the substrate with dimensions and location of the sensors. The open symbols (e.g., black, blue, red, and green) are AE source locations determined from the array of AE sensors (see Section 2.5.2).

2.4.2. Experimental conditions

We aimed to characterize the source of AE signals by using spot weld experiments and a wide range of processing parameters described in Table 2.1. In addition to tests with no powder (N), two different powders were used: Ti-6Al-4V (T) and SS304 (S) (Carpenter Additive, diameter: 15 - 45 μm). For the experiments, we use a multimode laser with a top-hat beam profile with laser power of 300 W (L) and 500 W (H) and dwell time of 1, 3, and 5 seconds. The parameters used here are not representative of current industrial processes. They are designed to repeatedly generate defects in a simplified environment where these processes can be unambiguously separated. There was not a specific reason for the choice of the spot weld locations except that they should be distinct from one another and carefully documented. The same Stainless steel substrate was used for all experiments, so that only a single calibration

experiment was needed, as described below.

Table 2.1. Experimental process parameters. Note that the powder layer thickness is 0.5 mm for all powder tests.

Test	Powder	Laser power [W]	Laser duration [s]
NH5	None	500	5
NL5		300	5
TH5	Ti-6Al-4V	500	5
TH3		500	3
TH1		500	1
TL5		300	5
TL3		300	3
TL1		300	1
SH5	SS304	500	5
SH3		500	3
SH1		500	1
SL5		300	5
SL3		300	3
SL1		300	1

2.4.3. Ball Impact Calibration Source

We performed a ball drop test prior to the experiments in order to introduce an AE source of known amplitude and frequency content. We dropped a 1 mm diameter steel ball 50 mm onto the substrate without a powder layer. The force-time function of the ball impact can be accurately described using Hertz theory (McLaskey & Glaser, 2010).

$$f(t) = F_{max} \cdot \sin(\pi t / t_c)^{3/2} \qquad \text{for } 0 \le t \le t_c \tag{2.3}$$

$$f(t) = 0 \qquad \text{otherwise}$$

In this expression, $F_{max} = 1.917\rho_1^{3/5}(\delta_1+\delta_2)^{-2/5}R_1^2v_0^{6/5}$, the contact duration, $t_c = 4.53(4\rho_1^3\pi(\delta_1+\delta_2)/3)^{2/5}R_1v_0^{-1/5}$, $\delta_i = (1-\mu_i^2)/(\pi E_i)$, E is Young's modulus, μ is Poisson's ratio, R_1 is radius of the ball, v_0 is initial velocity of the ball when it impacts, ρ_1 is the density of the ball, and subscripts 1 and 2 refer the material of the ball and the substrate, respectively. The force acts normal to the surface of the substrate (z direction, Figure 2.2). The AE sensors used in this work are sensitive to motions in the vertical direction and their instrument response has been previously determined using a ball drop calibration source (Wu & McLaskey, 2018).

In this work, we used the ball impact as an in-situ calibration source to verify all aspects of the monitoring system including sensor coupling and wave propagation in the substrate and to quantify the magnitude of the AE sources recorded during AM process. The magnitude of a seismic source is related to either the change in momentum for external sources or the seismic moment for internal sources and is estimated from the amplitude of the source at low frequencies. For the ball impact this is the change in momentum of the ball, $\Delta P = \int f(t)dt$, or, equivalently, $\Delta P = \Omega_{ball}$, which is the amplitude of the Fourier transform of f(t) at frequencies well below $f_0 = 1/t_c$ (Equation 2.3). ΔP can also be calculated from the ball's mass, m, and change in velocity Δv. The initial velocity can be estimated using drop height (h), $v_0 = \sqrt{2gh}$, and the rebound velocity can be measured using the time difference, Δt between the first and second impacts of the bouncing ball: $v_{rebound} = g\cdot\Delta t/2$.

The magnitude of an internal seismic source such as a crack or earthquake is related to the seismic moment, M_0 (Hanks & Kanamori, 1979), which is equal to the amplitude

of the Fourier transform of the source $M_{jl}(\xi, \tau)$ at low frequencies. These low-frequency amplitudes of external and internal seismic sources, ΔP and M_0 respectively, can be related to one another through a simple constant $C_{FM} = 2c$, where c is the wave velocity in the material where the source originates and the factor of 2 comes from the free surface effect (McLaskey et al., 2015). Using this relation, we estimate the equivalent seismic moment of the ball drop, $M_{0ball} = C_{FM} \cdot \Delta P$. Solids have both longitudinal and shear waves that travel at different speeds, so we assume c is equal to the average of those two waves speeds. Our assumed $C_{FM} = 9100$ m/s should be adequate for a variety of metals (e.g., Steel, Titanium, Inconel, etc.) since variations in wave velocity do not exceed 25 %. Variations in C_{FM} due to high temperatures are unlikely to exceed other sources of uncertainty associated with the method (McLaskey et al., 2015); rather, the absolute magnitudes reported here should be considered order-of-magnitude estimates. The 1 mm steel ball we used has $t_c = 3.5$ μs, therefore, $f_0 = 290$ kHz. We used the average amplitude of the Fourier transform of the ball drop signal in a low frequency band (10 – 40 kHz) to determine Ω_{ball}. The seismic moment of an arbitrary AE source, M_{0sig}, is calculated:

$$M_{0sig} = M_{0ball} \cdot \Omega_{sig} / \Omega_{ball} \tag{2.4}$$

where Ω_{sig}, is the average amplitude of the Fourier transform of the AE signal in the 10 - 40 kHz frequency range.

2.5. Results

2.5.1. Signal overview

Figure 2.3 shows representative examples of AE signals recorded from three different tests: Ti-6Al-4V powder, SS304 powder, and no powder. In each test, the 500 W laser was activated for a duration of 5 s while the stage remained stationary. The signals plotted in the left panels (Figures 2.3a, 2.3c, and 2.3e) are the low-rate, continuously recorded data from Channel 1 and insets show zoomed in sections of the signals generated when the laser was first turned on. Signals shown in the right panels (Figures 2.3b, 2.3d, and 2.3f) are from high-rate triggered data, also from Channel 1, with a zoomed-in time scale to highlight the differences.

We repeatedly observed significant differences in the types of signals produced by the tests on different powders. Tests on the Ti-6Al-4V powder produced swarms of impulsive AE events that primarily occurred when the laser was turned off and continued sporadically for tens of seconds. In contrast, tests on the SS304 powder and tests with no powder only produced AE signals when the laser was first turned on (Figures 2.3c and 2.3e). When no powder was present, this initial signal was abrupt and short-duration. It decayed back to the noise level after only ~3 ms (Figures 2.3e and 2.3f). When powder was present, the initial signal was not abrupt, was lower amplitude, had an extended duration (~200 ms), and consisted primarily of lower frequencies (Figures 2.3a inset, 2.3c inset, and 2.3d).

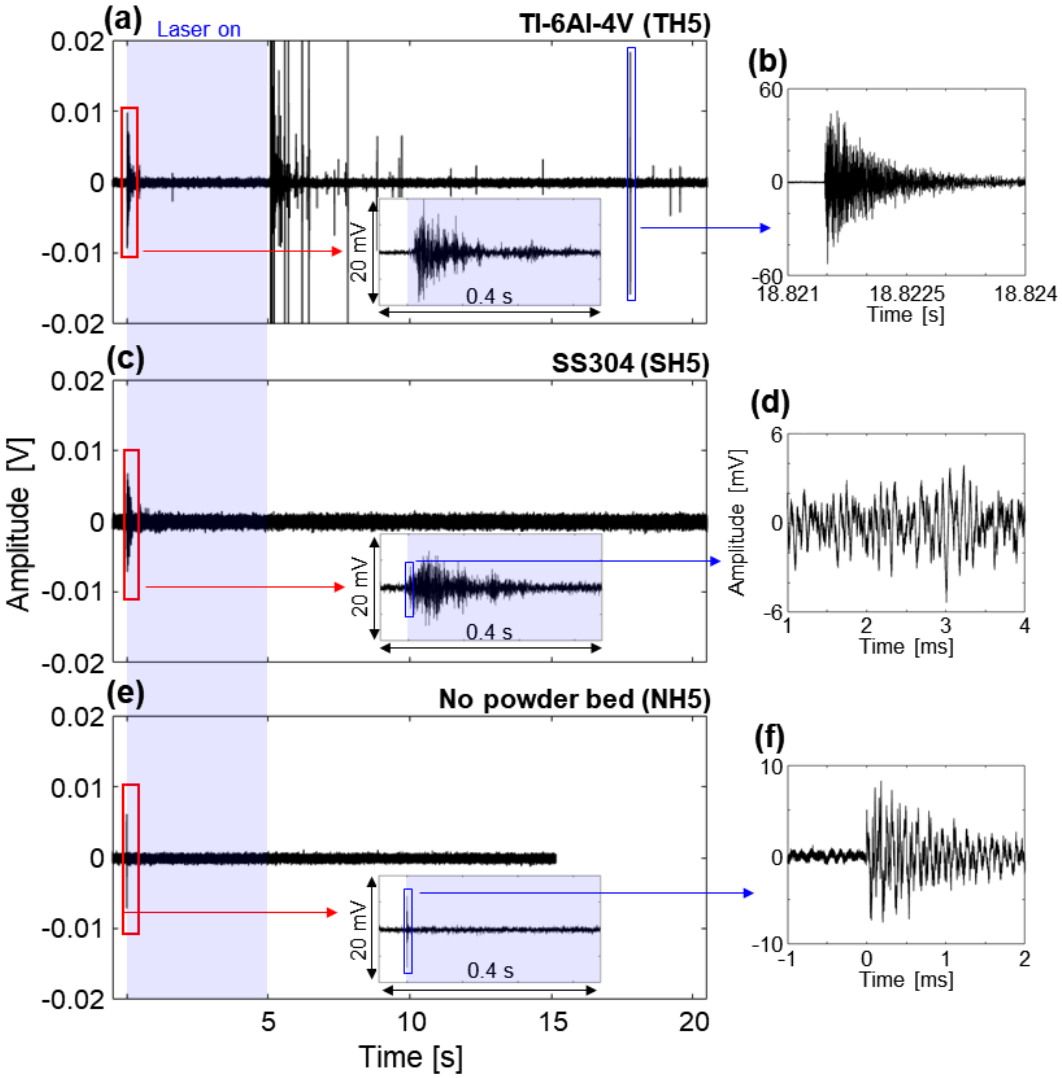

Figure 2.3. Overview of signals measured with different powders and 5 s laser duration (blue shaded area): (a and b) Ti-6Al-4V powder (TH5, see Table 2.1) and (c and d) SS304 powder (SH5) and (e and f) no powder (NH5). Note the swarm of impulsive AE signals in (a) that occurred just after the laser was turned off (see text). For the experiment shown in (e), the recording system was stopped after 15 seconds.

2.5.2. AEs and fractures in Ti-6Al-4V

Figure 2.4 shows the AE and SEM results of Ti-6Al-4V powder tests. The maximum amplitude of each triggered AE signal (black circles with stalks) is shown alongside the cumulative maximum amplitude of the AE signals (blue) and cumulative counts of

AE events (red) over time (Figures 2.4a to 2.4d). SEM cross section images were taken on the spot where the laser hit the substrate (Figures 2.4e and 2.4f). Recorded AEs were almost exclusively impulsive events that were rich in high frequency energy up to 1 MHz. We term these "crack" signals, since their features are similar to AEs observed to be associated with microcracks in rock and concrete (Manthei, 2005).

The maximum amplitude of the AE signals is larger in test TH5 (Figure 2.4b) than in TL5 (Figure 2.4d) and corresponding SEM images show larger cracks (~1 mm) in TH5 (Figure 2.4e) than in TL5 (Figure 2.4f), which are 20 - 70 μm. In Section 2.6.1.2, we outline how the physical size of the crack can be determined from the amplitude of the AE signal. We were able to use the timing of the abrupt first wave arrivals measured from signals recorded from the array of sensors to triangulate the source locations of the AEs, following standard techniques (Mclaskey & Glaser, 2007). Though there was some scatter in the results (+/- 1.4 mm standard deviation), we were able to confirm that signals originated from the designated weld spot, and we could clearly identify the separate locations of tests (see Figure 2.S1 for the method and Figure 2.2b for the result). The timing of the AEs generated during these tests indicates that the majority of the AEs and the largest AEs occurred soon after the laser was turned off, while AEs continued to occur sporadically for tens of seconds in a decaying manner. Some smaller AEs occurred immediately after the laser was turned on, but AEs were mostly absent while the laser remained on.

The melting mode can be delineated through the aspect ratio of the melt pool, which is defined by the ratio between the penetrated depth and width. The boundary of keyhole mode and conduction mode is characterized by the aspect ratio ranging from 0.4 to 0.8

(King et al., 2014; Tenbrock et al., 2020; Weckman et al., 1997). The SEM image clearly demonstrates that TH5 exhibits the aspect ratio of ~1, indicative of the keyhole mode. In contrast, TL5 barely penetrates the substrate, so it is closer to the conduction mode. The solidified melt was scattered with a solidified wing of Ti-6Al-4V powder in TH5 and many cracks in the melted part ranging from 50 μm to ~1 mm in length (Figure 2.4e). However, the solidified part in TL5 shows a more circular shape with small size of cracks, ~70 μm in length. As seen in AE counts (Figures 2.4b and 2.4d), the number of detected cracks in TH5 were ~3 times higher than that in TL5 and the amplitude of the largest AE signals in TH5 was also 10x higher than TL5. Likely, the SEM images show more cracks and larger cracks in TH5 (Figure 2.4e) than in TL5 (Figure 2.4f).

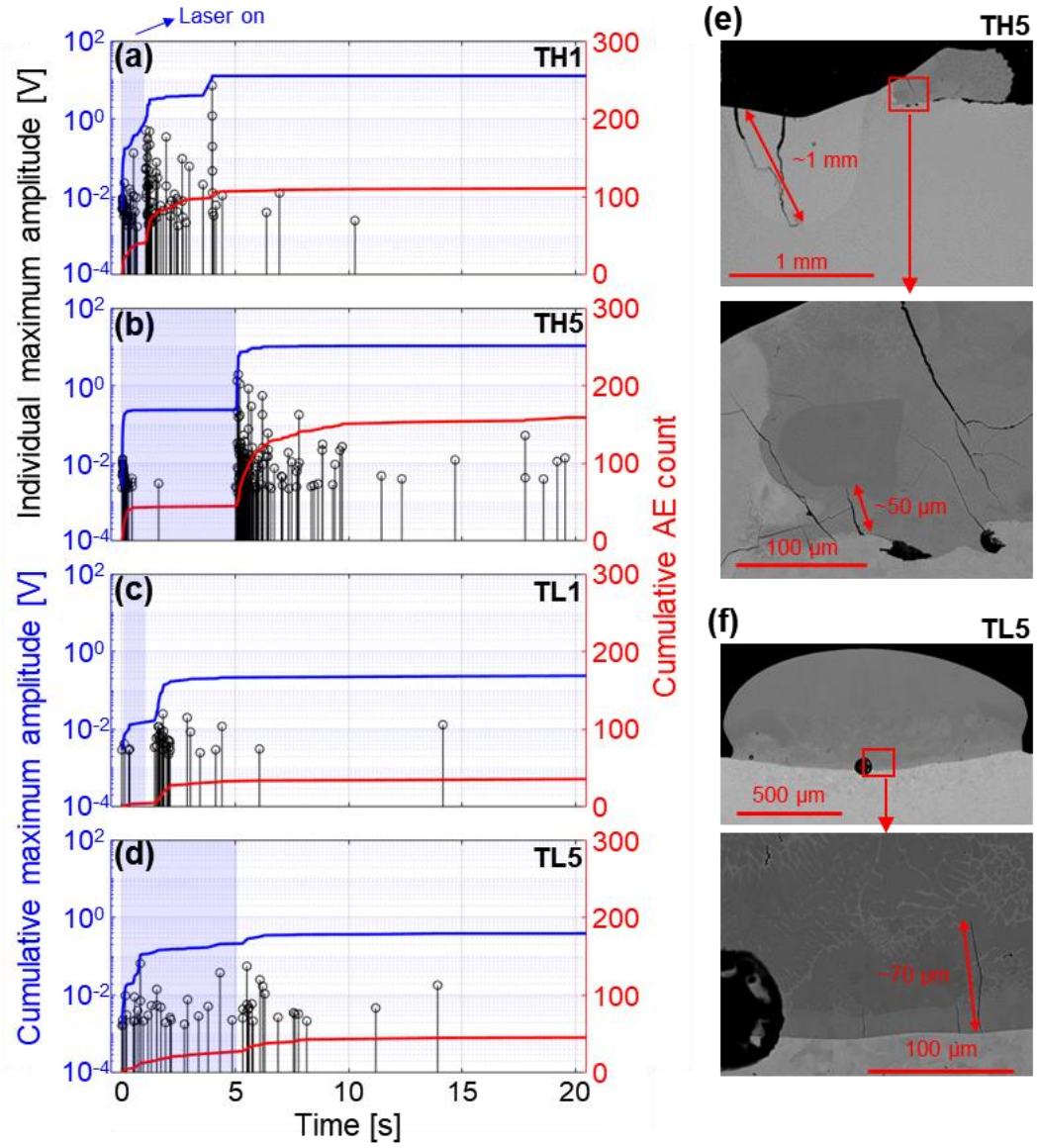

Figure 2.4. Maximum amplitude of each triggered signal (black), cumulative maximum amplitude (blue), and cumulative AE count (red) in Ti-6Al-4V powder tests (a) TH1, (b) TH5, (c) TL1, and (d) TL5. SEM images of welded cross section in (e) TH5 and (f) TL5.

2.5.3. Porosity and powder effect signal in SS304

Figure 2.5 shows SEM images and AE signal characteristics from tests with SS304 powder. Different from the Ti-6Al-4V samples, all the SEM cross-section images showed circular solidified melt (~1 mm diameter) with different amounts of porosity.

From the processing conditions listed in Table 2.1, the absorptivity of ~0.3, and the estimated 1-2 mm^3 volume, calculated volumetric energy densities indicate that SH1, SL3, and SL1 should exhibit porosity due to insufficient energy density, whereas SH5, SH3, and SL5 were closer to conduction modes. Pores were formed in most SS304 conditions presented here due to insufficient input of laser energy density, resulting in incomplete melting of the powder particles within the affected volume and causing irregular pore morphologies (Nudelis & Mayr, 2021). Consistent with expectations for defects due to insufficient energy density, we observe a reduction in porosity with increasing dwell time (SH5 and SL5) and increasing laser power. As mentioned previously, detectable AE signals were only produced when the laser was first turned on (Figure 2.3c). These signals were not typical AEs and were in many ways different from the "crack signals" described in the previous section. They have small amplitude, had an extended duration, were depleted of high frequency energy, and were not impulsive, so they could not be located. We do not consider them AE events; they are more similar to a transient noise and would not be detected by many AE monitoring systems. We term this category of signal "powder effect" signals since they were observed for tests with a powder layer (both Ti-6Al-4V and SS304), but not for tests without powder.

Figure 2.5g shows the +/- envelope of the amplitude of the acoustic signal over time. The envelope shown is a 10 ms moving average of the root-mean-square of the signal collected from the low-rate signals from Channel 1. The first signal in Figure 2.5g (black color) is derived from the same signal as Figure 2.3c. The AE signal amplitude was larger with higher laser energy. Note that our 10 ms moving average effectively

limits the bandwidth to 100 Hz, which allows us to use the continuous low-rate recorded signal sampled at 10 kHz. All other analyses in this study used high-rate signals sampled at 10 MHz.

To test if the AE signals were related to the observed porosity, Figure 2.5h shows the maximum amplitude of the AE signal envelope against the porosity, showing essentially no correlation. Porosity, defined as the ratio of the pore area and the area of the circular region, was quantified in the binarized image using the thresholding method. At the same laser duration, the maximum amplitude was smaller with 300 W laser energy than that with 500 W, but porosity was higher. This implies that the AE signal amplitude may be affected by the laser energy, but it does not have a direct correlation with porosity.

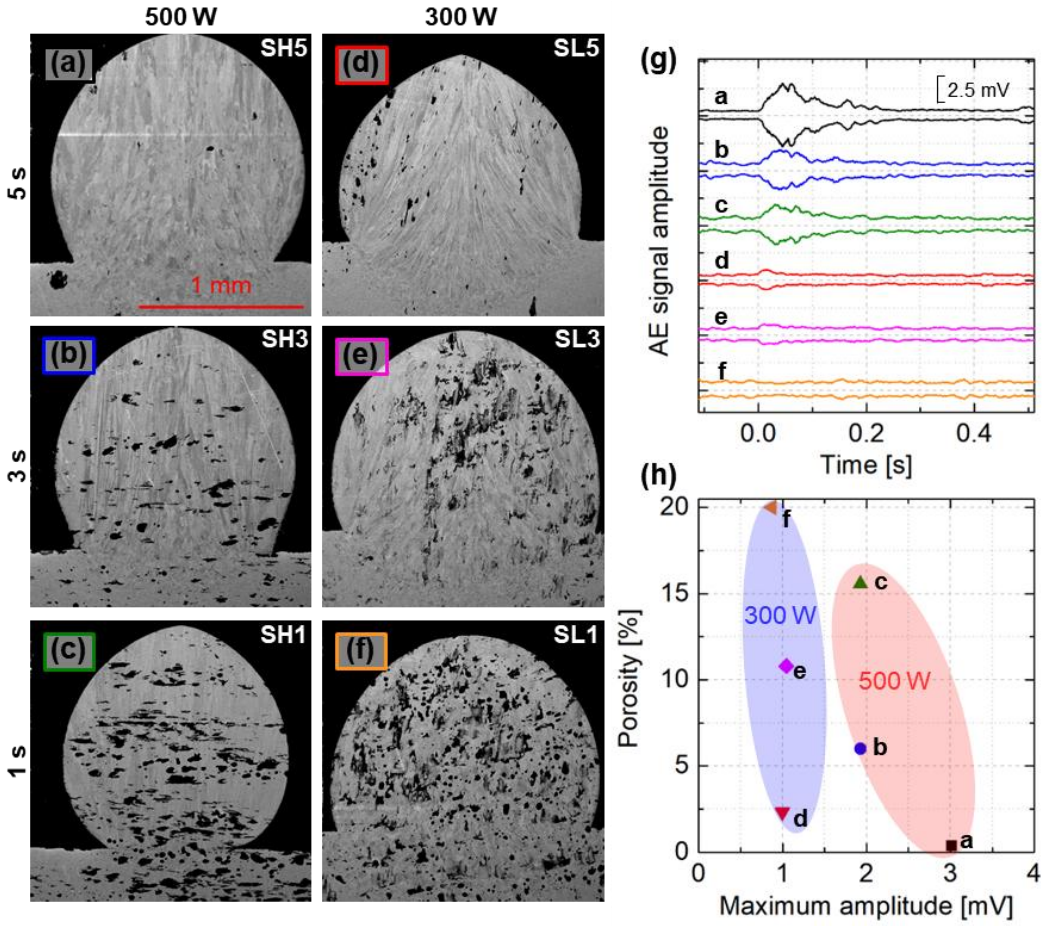

Figure 2.5. SEM images of cross sections of experiments with the SS304 powder with different laser energy and duration: (a) SH5, (b) SH3, (c) SH1, (d) SL5, (e) SL3, and (f) SL1 (See Table 2.1 for a list of tests). (g) The envelope of the signals, calculated from low-rate signals in Channel 1, see text. (h) The relationship between porosity calculated from SEM images and maximum amplitude from the envelope of the signals in (g).

2.5.4. Signal characteristics

In this section, we describe the different AE signals in both the time and frequency domain. Figure 2.6a shows representative examples of three different types of signals on an identical time scale: 1) crack signals, produced from the Ti-6Al-4V tests, 2) powder effect signals from SS304 and Ti-6Al-4V, and 3) the signals produced when the laser was first turned on during in tests with no powder, which we term “thermal

expansion". The example signals from the cracks are from the data shown in Figure 2.4b and occurred after the laser was deactivated at ~5.1 s for the large crack and ~5.8 s for the small crack. The example powder effect signals are from Figure 2.3c. The thermal expansion signal is the first arrival of the signal shown in Figure 2.3f. Similar to the crack signals, the thermal expansion exhibits an abrupt increase in amplitude upon the first arrival.

Figure 2.6b shows the Fourier transform of the signals in Figure 2.6a using a 2 ms time window. The different signals differ in both absolute amplitude and relative spectral shape. The crack signals contained the most high frequency energy while the thermal expansion and powder effect signals have spectra that are more depleted in the 100 kHz frequency band. We focused on two frequency bands denoted low (10 - 40 kHz) and high (70 - 150 kHz). We chose these frequency bands because of their good signal-to-noise ratio and because the low frequency band was below the corner frequency f_0 of the ball drop calibration source; however, different frequency bands that are sufficiently separated (i.e. 50 - 75 kHz and 300 - 450 kHz) could also be used for signal discrimination, depending on sensor properties or bandwidth limitations of the recording system. The average amplitude in the low frequency band was taken to be a measure of the size of the source or the seismic moment. We define the spectral ratio as a second discriminating parameter. It is the ratio of the average amplitude in the high frequencies band (A_{high}) to the average amplitude in the low frequency band (A_{low}), expressed in decibels (dB) such that spectral ratio = $20 \cdot \log_{10}(A_{high} / A_{low})$. The crack signals varied greatly in amplitude, but all exhibited a spectral ratio near 1. The thermal expansion had a distinctly smaller spectral ratio of 0.1 (-20 dB) while the

powder effect signal had a spectral ratio that was even lower.

Figure 2.6c maps the data blocks containing various AE signals using the maximum amplitude and spectral ratio. However, we used the signal maximum amplitude in the time domain instead of the seismic moment of the events (a frequency domain parameter), since those two quantities are generally proportional, as shown in Figure 2.7. For the cracks and thermal expansion, we confirmed that the signal-to-noise ratio (SNR) was greater than 10 dB in both the low frequency band and high frequency bands. For the powder effect signals, SNR was > 10 dB in the low frequency band, but not in the high frequency band. As a result, spectral ratios for powder effect signals shown here should be taken as upper bounds and could be much lower. Powder effect signals had spectral ratios of -25 dB to -35 dB meaning that the amplitude at low frequency band is at least 18 - 56 times higher than at high frequency band. An anomalous powder effect data point shown in Fig. 6c has a spectral ratio of -13 dB, much larger than the rest. This signal overlapped with some unknown source of 75 - 100 kHz energy that may have been due to a very small fracture or mechanical oscillation of some sort. Thermal expansion signals had intermediate spectral ratios that were larger than the powder effect signals, but far below the cracks.

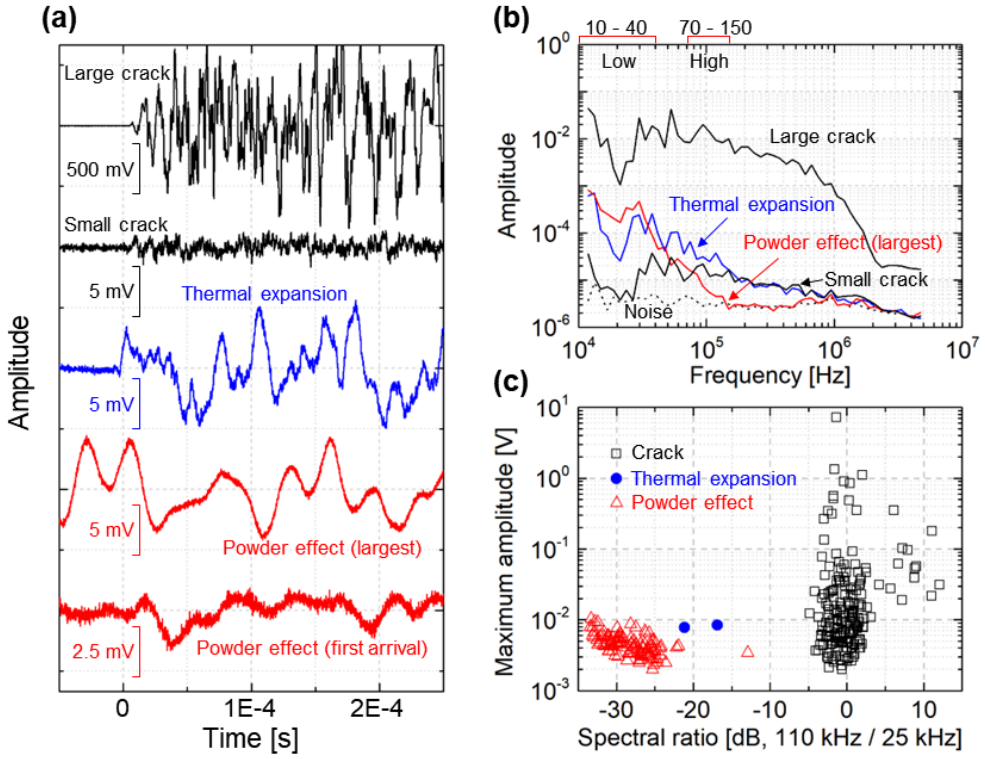

Figure 2.6. (a) Representative high-rate signals of large crack (TH5, see Table 2.1), small crack (TH5), thermal expansion (NH5), and powder effect showing both the first arrival and largest amplitude signals (SH5) and (b) the amplitude of the Fourier transform of the signals in (a). Note that the time window used to compute the Fourier transform was 2 ms. (c) Spectral ratio against the maximum amplitude in the time domain of all tests (see text).

2.6. Discussion

2.6.1. Cracks in Ti-6Al-4V

This study is not intended to identify the causes of cracks or to optimize printing parameters to prevent cracks or other defects. Instead, we chose parameters where defects could be consistently created and we focused on the discrimination of the AE signals associated with those defects. For tests on SS304, we did not observe microcracks in the SEM cross sections and we did not observe any impulsive AE events. However, for Ti-6Al-4V tests, we consistently observed many microcracks in

all the SEM cross sections and we detected sequences of impulsive AE events, as described in Section 2.5.2. This behavior happens because unlike SS304, Ti-6Al-4V forms intermetallic compounds with the SS304 substrate. These brittle compounds are prone to cracking due to tensile stresses induced by the cooling (Kempen et al., 2014; Yap et al., 2015). We also do not observe impulsive AE events during the tests without powder, except the single event when the laser was first turned on, labeled thermal expansion. We also located the AE sources to verify that they are coming from the location of the spot weld. This eliminates the possibility of spurious AE sources such as from sensor coupling, or the substrate supports. As shown in Figure 2.4, the majority of the impulsive AE events occurred when the laser was turned off and continued sporadically for tens of seconds. This time evolution suggests that the AEs are from thermal cracks that occurred due to tensile stresses induced by the cooling process (Kempen et al., 2014). Note that in experiment TL5 (Figures 2.4d and 2.4f) there are fewer cracks overall, but still a cluster of AEs were observed when the laser was turned off, between 5 and 6 seconds. We also note that AEs continued to occur for 10 s of seconds after the laser was turned off, and this is distinct from the decay of the reverberations that occurs after each individual AE event. It takes ~3 ms for the elastic waves generated from one impulsive AE event to decay back to approximately the noise level, shown schematically as the section of the signal with a gray background in Figure 2.1d. In contrast, impulsive AE events continued to occur, intermittently, at a rate that decayed over 10s of seconds, presumably as the specimen cooled.

2.6.1.1. Correlation of parameters in frequency domain and time domain

The correlation between seismic moment and maximum amplitude of triggered signals in Channel 1 is plotted in Figure 2.7. The maximum amplitude and seismic moment are linearly correlated (slope of 1 on log-log plot) regardless of laser energy and duration time. The Pearson correlation coefficient, γ_{xy}, can be used to estimate the linear statistical relationship (Bonamente, 2022; Kosiba et al., 2023). In Figure 2.7, the γ_{xy} value calculated for log-scale data is 0.924, indicating a strong linear correlation, as a value of 1 denotes perfect linearity. This linear proportionality exists because the low frequency range (10 - 40 kHz) used to estimate the seismic moment is also typically the frequency band with the largest amplitude (Figure 2.6b). Note that if a different frequency band was chosen or if a different sensor was used with a different frequency response, then seismic moment and maximum amplitude may not be linearly proportional or may have a different proportionality constant.

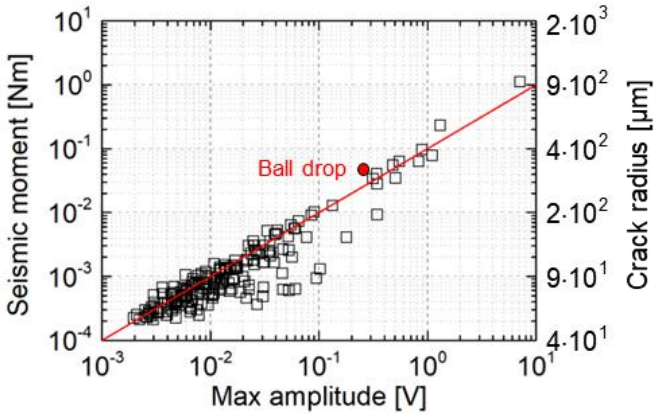

Figure 2.7. Maximum amplitude of high-rate signal in time domain and seismic moment calculated from the amplitude in frequency domain at low frequencies. Note that all the signals from Ti-6Al-4V powder tests in Channel 1.

2.6.1.2. Estimation of the physical size of cracks from the AE signal

We roughly estimated the physical size of cracks causing an AE signal by assuming that the seismic moment M_0 is approximately equal to the amplitude of the components of the time independent source moment tensor D_{ij}. Following (Scruby et al., 1985), the moment tensor of an opening crack has the form:

$$M_0 \approx D_{33} = (\lambda+2\mu)\cdot b\cdot dA \tag{2.5}$$

where 2b is the crack opening, dA is the fracture surface area, $\lambda = \nu\cdot E/(1+\nu)(1-2\nu)$ is the Lamé parameter, $\mu = E/2(1+\nu)$ is the shear modulus, E is the Young's modulus, and ν is the Poisson's ratio. This formulation assumes the area of the microcrack, dA, is in the x_1-x_2 plane and the crack opening direction is x_3, but changing this orientation will cause variations of only a factor of 2. We then assumed a circular elastic fracture of radius a with an elliptical cross section with maximum crack opening at the center (Green & Zerna, 1992; Scruby et al., 1985):

$$2b = [4(1-\nu)/(\pi E)]\cdot\sigma\cdot a \tag{2.6}$$

where σ is the stress change acting on the fracture surface. Plugging Equation 2.6 into Equation 2.5 and assuming the crack volume from a half-elliptical shape, we found:

$$dV = b\cdot dA = 2/3\pi\cdot a^2\cdot b \tag{2.7},$$

$$M_0 \approx K\cdot\sigma\cdot a^3 \tag{2.8},$$

where $K = 4(1-\nu)\cdot(\lambda+2\mu)/3E = 4(1-\nu)^2/[3(1+\nu)\cdot(1-2\nu)]$. Thus, $K \approx 1.3$ when $\nu \approx 0.3$. We can then solve for the crack radius a from Equation 2.8:

$$a \approx [M_0/(K\cdot\sigma)]^{1/3} \tag{2.9}$$

This is essentially identical to an expression used in the study of earthquakes derived

from the expressions $M_0 = \mu AD$ and $\Delta\sigma = C\mu D/a$ (Equations 1 and 5 from Kanamori and Anderson (Kanamori & Anderson, 1975)) by solving the second equation for D and inserting it into the first equation. In the previous expressions, A is the rupture area, D is the average fault slip over the rupture area, C is shape factor, and $\Delta\sigma$ is the shear stress drop.

For tensile fracture of metal, σ in Equation 2.9 is equal to the yield stress of the material, since the stresses felt on the crack surfaces likely drop from the yield stress to zero (free surfaces). Plugging realistic values for Ti-6Al-4V (σ = 880 MPa and ν = 0.34 so $K \approx 1.4$) into Equation 2.9, we obtained an expression for the crack radius in meters when the unit of M_0 is Nm:

$$a = (M_0/1.232e9)^{1/3} \tag{2.10}$$

Since the seismic moments varied from 10^{-4} Nm to 1 Nm (Figure 2.7), the corresponding crack radii ranged from ~40 μm to ~1 mm. This range is in reasonable agreement with the maximum crack length found from the SEM images (~1 mm in Figure 2.4e). Moreover, the triggered signals in TL5 (Figure 2.4d) exhibited $\sim 10^{-2}$ maximum amplitude, corresponding to ~90 μm crack radius, and this also aligns with the observations from the SEM image (~70 μm in Figure 2.4f). We admit that this corroboration between recorded AEs and SEM images is somewhat rough: we cannot know if the cracks in the SEM images opened in a single event or if they formed in multiple episodes and would therefore produce multiple AEs. There are also significant sources of uncertainty associated with the theory outlined above and with the absolute estimation of the M_0 from the recorded AE signals. We therefore consider the calculation of crack radii absolutely accurate only to a factor of 3, but we note that

the range of crack sizes estimated for our population of AE signals closely aligns with the sizes observed in SEM images.

2.6.2. Thermal expansion (Bare substrate)

Rapid thermal expansion of the substrate due to a laser pulse (Rose, 1984; Telschow & Conant, 1990) has previously been used as a standardized AE source (Scruby et al., 1981). In our experiments, we observed a signal when the laser was first turned on (Figure 2.3e), which we term "thermal expansion" (Section 2.5.4). We only found this signal in tests with no powder; the presence of the powder likely blocked the substrate from the laser and caused a longer-duration, lower-amplitude signal that we term "powder effect", described below. We can be sure of this result because a thermal expansion signal would have been detected based on its higher frequency content compared to the powder effect signal. While detection of this signal likely has little application in practical AM applications, it highlights how the AE signal parameters identified can be used to effectively discriminate cracks signals from other AE sources (Figure 2.6c).

2.6.3. Powder effect

As seen in Section 2.6.1, tests with powders did not produce abrupt thermal expansion signals, but did produce "powder effect" signals that were not impulsive, small in amplitude, and lasted ~0.2 s long. We do not fully understand the physical mechanism of this signal, but we know that it occurs when a laser first interacts with a powder layer. We observe such a powder effect signal with both the Ti-6Al-4V and SS powder

beds, despite those prints having extremely different quality. We do not observe the powder effect signal for the tests with no powder bed. The signal is likely due to the partially melted powder falling onto the substrate as the laser first hits it (Kaplan & Frostevarg, 2016). Such an AE source would be the cumulative effect of many tiny particle impacts or a diffuse thermal expansion effect, and this could account for the extended duration and low frequency dominance of the powder effect signal compared to the other signals. In fact, the extended duration, lack of high frequencies, and lack of abrupt onset observed for the powder effect signal are in many ways similar to tremor signals detected deep in the Earth, which are thought to be composed of myriad weak earthquake events (Shelly et al., 2007). The line scan results, described in Section 2.6.5, add further support for our interpretation because numerous powder effect signals were produced while the laser was actively scanning over new powder, and no powder effect signals were detected when the laser was stopped, despite the presence of crack signals and vibrations due to movement of the stage. Figure 2.5g shows that the amplitude of the powder effect signal increases with increasing laser power but is not affected by the laser duration or porosity of the print.

2.6.4. Pores

For the SS304 tests exhibited pervasive porosity; however, we found that the amount of porosity was not correlated with the amplitude or characteristics of the AE signals (Figure 2.5). Based on this, we conclude that porosity does not produce a detectable AE signal. However, Ito et al. (Ito et al., 2021) suggested that pores due to keyholes at high energy density were accompanied by strong AE signals. In that work, pores with

50 - 100 μm diameter presumably generated signals with ~100 mV maximum amplitude and were some of the largest signals detected in that study. Note that it is difficult to directly compare the amplitudes of AE signals collected using different sensors and experimental setups without taking into account differences in sensor sensitivity, amplification, and wave propagation. Seleznev et al. (Seleznev et al., 2022) found many residual pores when the powder was overly melted by the laser which is the same as the keyhole mechanism. However, there were no detectable AE signals in the overly melted zone. Instead, noticeable AEs were found in regions with cracks. Ito et al. (Ito et al., 2021) also showed many cracks around the pores, so there is a possibility that cracks (perhaps associated with the pores) generated the AEs rather than the pores themselves.

2.6.5. Extension to line scan and multilayer prints

The spot weld experiments presented so far in this study are not representative of current industrial practices. However, we believe that the signal discrimination techniques and insights made here can be applicable to more complicated cases of line scans and multilayer prints in an environment where additional noise sources are present. To demonstrate, we conducted a line scanning experiment (300 W laser energy, 15 mm/s scanning speed) using Ti-6Al-4V powder, as shown in Figure 2.8. The sensor distribution is similar to the spot weld experiments and the signals shown are from Channel 1 (Figure 2.S2). The maximum amplitude of each triggered AE signal is shown over time (Figure 2.8a) with red for powder effect and black for crack, based on the parameters described in Section 2.5.4, shown in Figure 2.8d. Different

from the spot weld experiments, we observed far more AEs and we observed numerous powder effect signals while the laser was actively scanning, rather than only when the laser was first turned on (Figure 2.3).

Similar to the spot weld experiments, we detected a swarm of crack signals after the laser was turned off, and these persisted sporadically for many seconds. Figure 2.8b presents representative signals of the powder effect and cracks. Figure 2.8c shows the recorded AE signals and focuses on the first few seconds of the experiment. The blue signal is from another sensor mounted near the laser head, far from the substrate. It shows vibrations due to movement of the stage. The laser was turned on at ~0.5 s before the stage started moving. The stage then moved for ~1 s, paused, and then returned to its original position after the laser was turned off. Figure 2.8d shows the AE signals mapped onto the same parameter space shown in Figure 2.6c. Once again, this allows for clear differentiation between cracks and other noise sources such as the powder effect signals. We note that with the application of a high-pass filter, crack signals can be detected even amid other simultaneous signal sources such as powder effect signals and mechanical vibrations.

While the application of these methods to multilayer builds and conditions similar to current AM practice is outside the scope of this study, we note that the addition of a complicated part, as shown schematically in Figure 2.1, will only add an additional effect to the wave propagation component (G_{kj}) of the recorded signal. Such an addition will likely distort signals on the 1 - 10 μs time scale and could potentially produce a resonance of the part that would affect the overall shape of the spectra of the AE signals. The former would make source location more difficult and the latter

would potentially affect the absolute value of the parameters of Figure 2.8d, but would not affect the relative differences that can be used to differentiate cracks from other sources. Overall, the changes outlined above would not have a strong effect on our ability to measure (1) the abruptness of the sources and the spectral ratio parameter, (2) the timing of the sources, (3) the absolute amplitude of the source (since attenuation is low in metallic materials), and (4) the variety of AE sizes observed. We believe that the main insights from this study remain unchanged. Cracks can be easily detected amid other, lower frequency sources associated with powder effects and mechanical noise, physical crack size can be estimated using absolute calibration, and pores do not produce detectable AE signals.

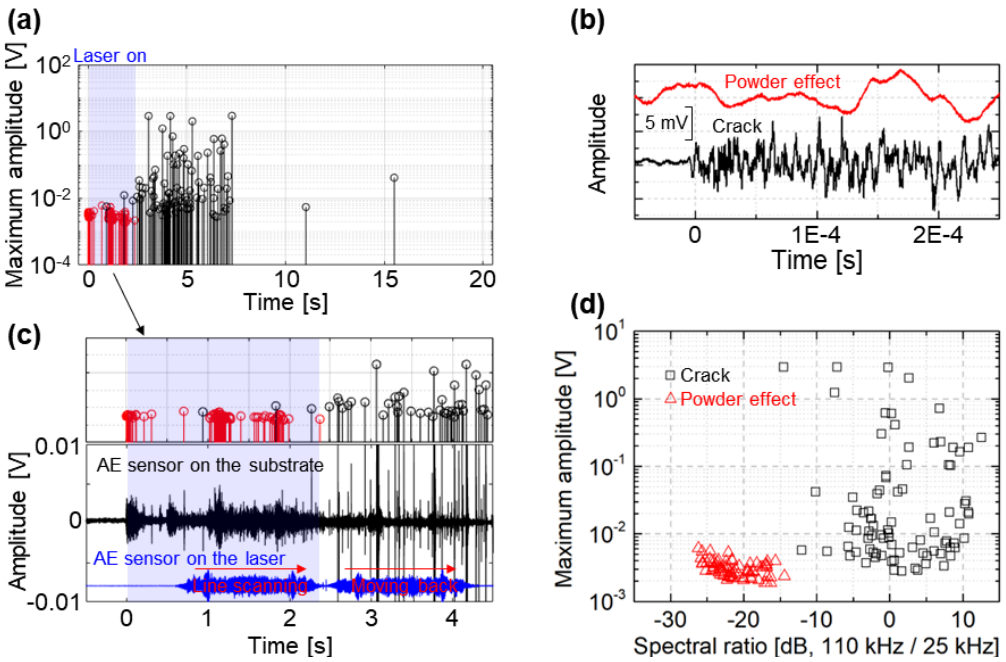

Figure 2.8. Line scanning experiment with 300 W laser energy and 15 mm/s scanning speed. (a) Maximum amplitude of triggered signals with time. (b) Powder effect signal (red) and crack signal (black) as representative examples. (c) Overview of the signal when the laser was activated, with the AE sensor on the laser (blue) capturing the laser movement. Note that the first movement (0.8 s to 2.3 s) is line scanning whereas the second movement (2.5 s to 4.2 s) is the stage moving back while the laser is off. (d) Spectral ratio plotted against the maximum amplitude in the time domain.

2.7. Summary and Conclusions

We studied the method of AE for monitoring defects during AM process due to its advantages of being a real-time nondestructive technique. Different from previous studies focused on signal classification without a proper understanding of the signal origins, we investigated the individual signal characteristics and underlying physical mechanisms of AEs generated during spot welds in a simplified experimental system that did not replicate current industrial processes but allowed us to link AE signal parameters to their physical mechanisms. Three types of AE signals could be clearly distinguished: 1) powder effect, 2) thermal expansion, and 3) cracks. We also utilized a ball drop test to calibrate the AE recording system and determine the absolute seismic moment of the AE sources, which was then used to estimate the physical size of the cracks that produced the AE signals. The calculated size distribution (40 μm - 1 mm) was generally consistent with the sizes of cracks observed in SEM images and tests with smaller observed cracks also had AEs with smaller maximum amplitude. From the analyzed data, the following observations and conclusions can be drawn:

1. A ball drop test was conducted for the absolute calibration of the AE recording setup and the calculation of seismic moment or size of the AE signals.
2. The physical size of the cracks was estimated from the absolute seismic moment of the recorded AEs. The calculated crack sizes approximately matched with crack sizes found from SEM images.
3. In tests with no powder, an abrupt, short duration (2 ms) signal was detected only at the beginning of the laser heating despite the fact that the laser continuously heated the substrate. This signal was induced by sudden thermal

expansion of the substrate. This type of signal did not occur for tests with powder.

4. In tests with a powder, an extended duration (~0.2 s) “power effect” signal was detected when the laser was first turned on. These signals were low amplitude, deficient in high frequency signal energy compared to other types of signals and lacked abrupt first arrivals. These characteristics, and the increased number of powder effect signals observed during line scans, are consistent with the idea that the source of the signal is from hot powder hitting the substrate and producing a diffuse thermal expansion signal.
5. Ti-6Al-4V powder tests produced tens to hundreds of abrupt, short duration AE signals with a range of amplitudes. They mostly occurred during solidification and for many seconds after the laser was turned off. SEM images of samples from these tests showed cracks.
6. Pores do not appear to produce AE signals; porosity was not correlated with the amplitude or characteristics of the signals recorded.
7. The spectral ratio of high-frequency (70 - 150 kHz) to low-frequency (10 - 40 kHz) energy in the AE signals was the primary parameter used to discriminate between different AE sources. Cracks had spectral ratios near 0, while the powder effect signals had spectral ratios that were at least 30 dB lower. Thermal expansion signals had an intermediate spectral ratio between that of the cracks and powder effect.
8. The line scanning experiment illustrates the utility of the spot experiment in identifying signal types within the line experiment.

While it is acknowledged that the spot experiment is not a direct representation of standard AM practice, our emphasis on fundamental mechanisms has helped us distinguish between various types of AE sources that could potentially occur during the AM process.

Our study has also allowed us to identify certain limitations of the method. For example, our study suggests that AE is a powerful technique to detect solidification cracking but is largely insensitive to pore detection. Another method, such as active source ultrasonic techniques (Felice & Fan, 2018), would likely be needed for direct detection of such pores. Furthermore, the low frequency "powder effect" signal will likely be a nearly continuous source of noise when printing lines (Figure 2.8c) and layers in more complex structures. Yet, this noise is primarily low frequency (< 30 kHz), so, with proper filtering, high frequency AEs associated with cracks can still be distinguished even below the noise level. Other sources of noise such as previously reported bursts associated with electronic control devices (Kononenko et al., 2023; Seleznev et al., 2022) may overlap with the frequency content of the crack signals described here. In this study, we used an array of four AE sensors, so we used the relative timing of wave arrivals between the sensors (i.e., source location) to distinguish AEs from electrical noise and other sources that originated from outside the printed part. However, when only one AE sensor is used, additional time- and frequency-domain parameters may be needed to distinguish between AEs associated with cracks and other noise sources.

Finally, the quantification of crack sizes from AE analysis is possible due to an absolute calibration technique and shows that we can detect cracks down to about 40

μm in size. We encourage other researchers to utilize a ball drop or similar calibration technique since this will facilitate meaningful comparisons between studies conducted in different laboratories, regardless of the sensors or materials used. Absolute quantification of the source size (in seismic moment) will allow researchers to check the accuracy and reproducibility of their results and will facilitate the advancement of this monitoring technique.

2.8. Supplementary Figures

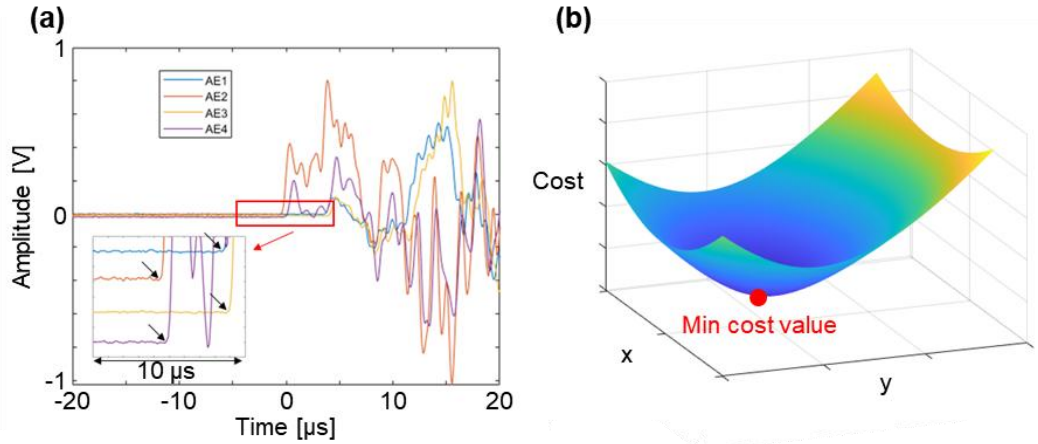

$$\text{Cost} = \sum_{i=1}^{n} \left| \sqrt{(x - xi)^2 + (y - y_i)^2 + (z - z_i)^2} - Vp(ti - t_0) \right|$$

x_i, y_i, z_i, and t_i = Coordinates for i^{th} sensor and P-wave arrival time

x, y, z, and t_0 = Coordinates for mesh point and arrival time

Figure 2.S1. Source location method using minimizing cost function. (a) The first arrival time for each signal and (b) contour of cost value. Assumed that all the events generated at the surface (i.e., z is fixed to 12.7 mm) and the gap between the mech point is 0.1337 mm in x and y directions.

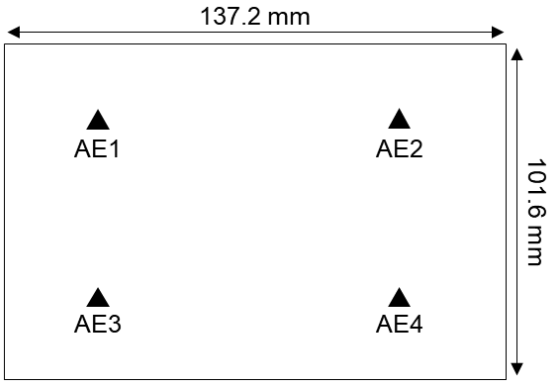

Figure 2.S2. Top view of the substrate with dimensions and location of the sensors.

REFERENCES

Aki, K., & Richards, P. (1980). *Quantitative Seismology: Theory and Methods*.

Alipour, S., Moridi, A., Liou, F., & Emdadi, A. (2022). The Trajectory of Additively Manufactured Titanium Alloys with Superior Mechanical Properties and Engineered Microstructures. *Additive Manufacturing*, *60*(PA), 103245. https://doi.org/10.1016/j.addma.2022.103245

Bonamente, M. (2022). *Statistics and Analysis of Scientific Data* (Vol. 34). Singapore: Springer Nature Singapore. https://doi.org/10.1007/978-981-19-0365-6

Brandt, M., Sun, S., Leary, M., Feih, S., Elambasseril, J., & Liu, Q. (2013). High-value SLM aerospace components: From design to manufacture. *Advanced Materials Research*, *633*(February 2015), 135–147. https://doi.org/10.4028/www.scientific.net/AMR.633.135

Caiazzo, F., Cardaropoli, F., Alfieri, V., Sergi, V., & Cuccaro, L. (2013). Experimental analysis of selective laser melting process for Ti-6Al-4V turbine blade manufacturing. *XIX International Symposium on High-Power Laser Systems and Applications 2012*, *8677*(January 2013), 86771H. https://doi.org/10.1117/12.2010577

Das, S., Wohlert, M., Beaman, J. J., & Bourell, D. L. (1999). Processing of titanium net shapes by SLS/HIP. *Materials and Design*, *20*(2–3), 115–121. https://doi.org/10.1016/s0261-3069(99)00017-5

Dass, A. (2020). *Fundamentals of Solidification in Directed Energy Deposition Type Additive Manufacturing of Inconel 625*. *Cornell University*. https://doi.org/https://doi.org/10.7298/f59s-yn90

Dass, A., Gabourel, A., Pagan, D., & Moridi, A. (2022). Laser based directed energy deposition system for operando synchrotron x-ray experiments. *Review of Scientific Instruments*, *93*(7). https://doi.org/10.1063/5.0081186

Eitzen, D., & Breckenridge, F. (1987). Acoustic emission sensors and their calibration. *American Society for Nondestructive Testing*, *5*, 121–132.

Enoki, M., Watanabe, M., Chivavibul, P., & Kishi, T. (2000). Non-contact measurement of acoustic emission in materials by laser interferometry. *Science and Technology of Advanced Materials*, *1*(3), 157–165. https://doi.org/10.1016/S1468-6996(00)00017-6

Eschner, N., Weiser, L., Häfner, B., & Lanza, G. (2020). Classification of specimen density in Laser Powder Bed Fusion (L-PBF) using in-process structure-borne

acoustic process emissions. *Additive Manufacturing*, *34*(March), 101324. https://doi.org/10.1016/j.addma.2020.101324

Felice, M. V., & Fan, Z. (2018). Sizing of flaws using ultrasonic bulk wave testing: A review. *Ultrasonics*, *88*, 26–42. https://doi.org/10.1016/j.ultras.2018.03.003

Gong, H., Rafi, K., Gu, H., Janaki Ram, G. D., Starr, T., & Stucker, B. (2015). Influence of defects on mechanical properties of Ti-6Al-4V components produced by selective laser melting and electron beam melting. *Materials and Design*, *86*, 545–554. https://doi.org/10.1016/j.matdes.2015.07.147

Green, A. E., & Zerna, W. (1992). *Theoretical elasticity*. Courier Corporation.

Grosse, C. U., & Ohtsu, M. (2008). *Acoustic Emission Testing: Basics for Research – Applications in Engineering*. Springer-Verlag Berlin Heidelberg.

Gu, D., Hagedorn, Y. C., Meiners, W., Meng, G., Batista, R. J. S., Wissenbach, K., & Poprawe, R. (2012). Densification behavior, microstructure evolution, and wear performance of selective laser melting processed commercially pure titanium. *Acta Materialia*, *60*(9), 3849–3860. https://doi.org/10.1016/j.actamat.2012.04.006

Hanks, T. C., & Kanamori, H. (1979). A moment magnitude scale. *Journal of Geophysical Research B: Solid Earth*, *84*(B5), 2348–2350. https://doi.org/10.1029/JB084iB05p02348

Holford, K. M., Eaton, M. J., Hensman, J. J., Pullin, R., Evans, S. L., Dervilis, N., & Worden, K. (2017). A new methodology for automating acoustic emission detection of metallic fatigue fractures in highly demanding aerospace environments: An overview. *Progress in Aerospace Sciences*, *90*(January), 1–11. https://doi.org/10.1016/j.paerosci.2016.11.003

Hsu, N., & Breckenridge, F. (1981). Characterization and calibration of acoustic emission sensors. *Materials Evaluation*, *39*, 60–68.

Ito, K., Kusano, M., Demura, M., & Watanabe, M. (2021). Detection and location of microdefects during selective laser melting by wireless acoustic emission measurement. *Additive Manufacturing*, *40*(September 2020), 101915. https://doi.org/10.1016/j.addma.2021.101915

Kanamori, H., & Anderson, D. L. (1975). Theoretical basis of some empirical relations in seismology. *Bulletin of the Seismological Society of America*, *65*(5), 1073–1095.

Kaplan, A. F. H., & Frostevarg, J. (2016). High speed imaging of powder incorporation into the melt pool in LAM. In *International Congress on Applications of Lasers & Electro-Optics* (Vol. 1, p. 1601). Laser Institute of

America. https://doi.org/10.2351/1.5118551

Kempen, K., Vrancken, B., Buls, S., Thijs, L., Van Humbeeck, J., & Kruth, J. P. (2014). Selective Laser Melting of Crack-Free High Density M2 High Speed Steel Parts by Baseplate Preheating. *Journal of Manufacturing Science and Engineering, Transactions of the ASME*, *136*(6). https://doi.org/10.1115/1.4028513

King, W. E., Barth, H. D., Castillo, V. M., Gallegos, G. F., Gibbs, J. W., Hahn, D. E., et al. (2014). Observation of keyhole-mode laser melting in laser powder-bed fusion additive manufacturing. *Journal of Materials Processing Technology*, *214*(12), 2915–2925. https://doi.org/10.1016/j.jmatprotec.2014.06.005

Kononenko, D. Y., Nikonova, V., Seleznev, M., van den Brink, J., & Chernyavsky, D. (2023). An in situ crack detection approach in additive manufacturing based on acoustic emission and machine learning. *Additive Manufacturing Letters*, *5*(December 2022), 100130. https://doi.org/10.1016/j.addlet.2023.100130

Kosiba, K., Kononenko, D. Y., Chernyavsky, D., Deng, L., Bednarcik, J., Han, J., et al. (2023). Maximizing vitrification and density of a Zr-based glass-forming alloy processed by laser powder bed fusion. *Journal of Alloys and Compounds*, *940*, 168946. https://doi.org/10.1016/j.jallcom.2023.168946

Liu, Q. C., Elambasseril, J., Sun, S. J., Leary, M., Brandt, M., & Sharp, P. K. (2014). The effect of manufacturing defects on the fatigue behaviour of Ti-6Al-4V specimens fabricated using selective laser melting. *Advanced Materials Research*, *891–892*(May 2019), 1519–1524. https://doi.org/10.4028/www.scientific.net/AMR.891-892.1519

Lu, Q. Y., & Wong, C. H. (2018). Additive manufacturing process monitoring and control by non-destructive testing techniques: challenges and in-process monitoring. *Virtual and Physical Prototyping*, *13*(2), 39–48. https://doi.org/10.1080/17452759.2017.1351201

Manthei, G. (2005). Characterization of acoustic emission sources in a rock salt specimen under triaxial compression. *Bulletin of the Seismological Society of America*, *95*(5), 1674–1700. https://doi.org/10.1785/0120040076

Mazumder, J., Schifferer, A., & Choi, J. (1999). Direct materials deposition: designed macro and microstructure. *Materials Research Society Symposium - Proceedings*, *542*, 51–63. https://doi.org/10.1557/proc-542-51

McCann, R., Obeidi, M. A., Hughes, C., McCarthy, É., Egan, D. S., Vijayaraghavan, R. K., et al. (2021). In-situ sensing, process monitoring and machine control in Laser Powder Bed Fusion: A review. *Additive Manufacturing*, *45*(April). https://doi.org/10.1016/j.addma.2021.102058

Mclaskey, G. C., & Glaser, S. D. (2007). Temporal Evolution and 3D Locations of Acoustic Emis- Sions Produced From the Drying Shrinkage of Concrete. *Advances in Acoustic Emission*, *6*, 52–57.

McLaskey, G. C., & Glaser, S. D. (2010). Hertzian impact: Experimental study of the force pulse and resulting stress waves. *The Journal of the Acoustical Society of America*, *128*(3), 1087. https://doi.org/10.1121/1.3466847

McLaskey, G. C., & Glaser, S. D. (2012). Acoustic emission sensor calibration for absolute source measurements. *Journal of Nondestructive Evaluation*, *31*(2), 157–168. https://doi.org/10.1007/s10921-012-0131-2

McLaskey, G. C., Lockner, D. A., Kilgore, B. D., & Beeler, N. M. (2015). A Robust Calibration Technique for Acoustic Emission Systems Based on Momentum Transfer from a Ball Drop. *Bulletin of the Seismological Society of America*, *105*(1), 257–271. https://doi.org/10.1785/0120140170

Nudelis, N., & Mayr, P. (2021). A novel classification method for pores in laser powder bed fusion. *Metals*, *11*(12), 1–16. https://doi.org/10.3390/met11121912

Rose, L. R. F. (1984). Point-source representation for laser-generated ultrasound. *Journal of the Acoustical Society of America*, *75*(3), 723–732. https://doi.org/10.1121/1.390583

Scruby, C. B., Wadley, H. N. G., Dewhurst, R. J., Palmer, S. B., & Hutchins, D. A. (1981). A laser-generated standard acoustic emission source. *Materials Evaluation*, *39*, 1250–1254.

Scruby, C. B., Baldwin, G. R., & Stacey, K. A. (1985). Characterisation of fatigue crack extension by quantitative acoustic emission. *International Journal of Fracture*, *28*(4), 201–222. https://doi.org/10.1007/BF00035216

Seleznev, M., Gustmann, T., Miriam, J., Alexander, U., Kühn, U., Kristin, J., et al. (2022). In situ detection of cracks during laser powder bed fusion using acoustic emission monitoring. *Additive Manufacturing Letters*, *3*(October), 100099. https://doi.org/10.1016/j.addlet.2022.100099

Shelly, D. R., Beroza, G. C., & Ide, S. (2007). Non-volcanic tremor and low-frequency earthquake swarms. *Nature*, *446*(7133), 305–307. https://doi.org/10.1038/nature05666

Telschow, K. L., & Conant, R. J. (1990). Optical and thermal parameter effects on laser-generated ultrasound. *The Journal of the Acoustical Society of America*, *88*(3), 1494–1502. https://doi.org/10.1121/1.400306

Tempelman, J. R., Wachtor, A. J., Flynn, E. B., Depond, P. J., Forien, J. B., Guss, G. M., et al. (2022). Detection of keyhole pore formations in laser powder-bed

fusion using acoustic process monitoring measurements. *Additive Manufacturing*, *55*(September 2021), 102735. https://doi.org/10.1016/j.addma.2022.102735

Tenbrock, C., Fischer, F. G., Wissenbach, K., Schleifenbaum, J. H., Wagenblast, P., Meiners, W., & Wagner, J. (2020). Influence of keyhole and conduction mode melting for top-hat shaped beam profiles in laser powder bed fusion. *Journal of Materials Processing Technology*, *278*(May 2019), 116514. https://doi.org/10.1016/j.jmatprotec.2019.116514

Wasmer, K., Le-Quang, T., Meylan, B., & Shevchik, S. A. (2019). In Situ Quality Monitoring in AM Using Acoustic Emission: A Reinforcement Learning Approach. *Journal of Materials Engineering and Performance*, *28*(2), 666–672. https://doi.org/10.1007/s11665-018-3690-2

Weckman, D. C., Kerr, H. W., & Liu, J. T. (1997). The effects of process variables on pulsed Nd:YAG laser spot welds: Part II. AA 1100 aluminum and comparison to AISI 409 stainless steel. *Metallurgical and Materials Transactions B: Process Metallurgy and Materials Processing Science*, *28*(4), 687–700. https://doi.org/10.1007/s11663-997-0043-1

Wu, B. S., & McLaskey, G. C. (2018). Broadband Calibration of Acoustic Emission and Ultrasonic Sensors from Generalized Ray Theory and Finite Element Models. *Journal of Nondestructive Evaluation*, *37*(1), 1–16. https://doi.org/10.1007/s10921-018-0462-8

Yan, C., Hao, L., Hussein, A., & Young, P. (2015). Ti-6Al-4V triply periodic minimal surface structures for bone implants fabricated via selective laser melting. *Journal of the Mechanical Behavior of Biomedical Materials*, *51*, 61–73. https://doi.org/10.1016/j.jmbbm.2015.06.024

Yap, C. Y., Chua, C. K., Dong, Z. L., Liu, Z. H., Zhang, D. Q., Loh, L. E., & Sing, S. L. (2015). Review of selective laser melting: Materials and applications. *Applied Physics Reviews*, *2*(4). https://doi.org/10.1063/1.4935926

Ye, D., Hong, G. S., Zhang, Y., Zhu, K., & Fuh, J. Y. H. (2018). Defect detection in selective laser melting technology by acoustic signals with deep belief networks. *International Journal of Advanced Manufacturing Technology*, *96*(5–8), 2791–2801. https://doi.org/10.1007/s00170-018-1728-0

Zhang, B., Li, Y., & Bai, Q. (2017). Defect Formation Mechanisms in Selective Laser Melting: A Review. *Chinese Journal of Mechanical Engineering (English Edition)*, *30*(3), 515–527. https://doi.org/10.1007/s10033-017-0121-5

Zhang, L. C., Klemm, D., Eckert, J., Hao, Y. L., & Sercombe, T. B. (2011). Manufacture by selective laser melting and mechanical behavior of a biomedical Ti-24Nb-4Zr-8Sn alloy. *Scripta Materialia*, *65*(1), 21–24. https://doi.org/10.1016/j.scriptamat.2011.03.024

Zhirnov, I., & Kouprianoff, D. (2022). Acoustic Diagnostic of Laser Powder Bed Fusion Processes. *Advances in Transdisciplinary Engineering*, *21*, 542–552. https://doi.org/10.3233/ATDE220173

CHAPTER 3

Laboratory earthquake ruptures contained by velocity strengthening fault patches

This chapter is drawn from the peer-reviewed journal paper: *Song, J.Y. and McLaskey, G.C., 2024. Laboratory earthquake ruptures contained by velocity strengthening fault patches. Journal of Geophysical Research: Solid Earth, 129(4), p.e2023JB028509. https://doi.org/10.1029/2023JB028509.*

3.1. Abstract

Many natural faults are believed to consist of velocity weakening (VW) patches surrounded by velocity strengthening (VS) sections. Numerical studies routinely employ this framework to study earthquake sequences including repeating earthquakes. In this laboratory study, we made a VW asperity, of length L, from a bare Poly(methyl methacrylate) PMMA frictional interface and coated the surrounding interface with Teflon to make VS fault sections. Behavior of this isolated asperity was studied as a function of L (ranging from 100 mm to 400 mm) and the critical nucleation length, h^*, which is inversely proportional to the applied normal stress (2-16 MPa). Consistent with recent numerical simulations, we observed aseismic slip for $L/h^* < 2$, periodic slip for $2 < L/h^* < 6$, and non-periodic slip for $10 < L/h^*$. Furthermore, we compared the experiments where L was contained by VS material to standard stick-slip events where L was bounded by free surfaces (i.e., L = the total sample length). The free surface case produced ~10 times larger slip during stick-slip

events compared to the contained fault ruptures, even with identical L/h^*. This disparity highlights how standard, complete-rupture stick-slip events differ from contained events expected in nature, due to both the free surface conditions and the heterogeneous normal stress along the fault near the free ends, as confirmed by Digital Image Correlation (DIC) analysis. This study not only introduces the Teflon coating experimental technique for containing laboratory earthquake ruptures, but also highlights the utility of L/h^* as a predictive parameter for earthquake behavior.

3.2. Introduction

Fault zones are composed of various minerals which can be divided into two main classes: velocity strengthening (VS) fault sections that slide stably and velocity weakening (VW) fault sections that slip unstably and nucleate earthquakes (Dieterich, 1992; Rice & Ruina, 1983). Depending on the arrangement of VS and VW sections, a variety of earthquake behavior has been observed on the same fault. In subduction zones, for example, there is a locked zone (VW) that causes megathrust earthquakes and also other zones, usually in shallower or deeper areas (VS) that produce slow slip events (Ito et al., 2007; Obara et al., 2004; Obara & Kato, 2016; Wallace et al., 2016). Slow slip is also found on transform boundaries in the San Andreas fault system within the serpentine zones, creeping at ~30 mm/year (Moore & Rymer, 2007; Titus et al., 2006). Therefore, VS and VW materials are prevalently distributed in natural faults.

Advances in numerical simulation have provided valuable insights into the diverse slip behavior that can occur on heterogeneous faults (e.g. Luo & Ampuero, 2018). In

particular, if the length (L) of a single VW fault section (i.e., seismic asperity) surrounded by VS sections is less than the critical nucleation length scale (h^*), then only quasi-stable sliding occurs. Both slow and fast ruptures occur when $L \approx h^*$ (Veedu & Barbot, 2016). As the ratio L/h^* increases, a wide range of slip behaviors is observed, ranging from periodic slow slips to chaotic fast ruptures (Barbot, 2019). Simulations involving multiple asperities have been employed to study complex natural faults (Luo & Ampuero, 2018; Nakata et al., 2011).

Laboratory experiments also explored this behavior. Fault gouges of different composition were employed to make a VW fault section surrounded by VS gouges (Bedford et al., 2022; Buijze et al., 2021). However, these experiments showed that nonuniform compaction of the gouges can cause heterogeneous normal stress distributions that complicate the interpretation of the results (Buijze et al., 2020, 2021). Despite this added complexity, those authors do see rupture confinement in the velocity strengthening patches, as well as transitional slip modes from aseismic to seismic as a function of L/h^* that are generally consistent with theory and numerical models.

More commonly, lab experiments use a VW fault surface using rocks or plastic materials, surrounded by the free surfaces of the sample (i.e., L = total sample length). These experiments also reported fast and slow stick-slip events (Leeman et al., 2016; Mclaskey & Yamashita, 2017; Mei et al., 2021, 2022; Yamashita et al., 2022). However, in this case, the free ends of the sample are more unstable than the interior of the sample, so the fault ends can act as asperities (Cebry et al., 2022), which does not correctly simulate natural seismic zones.

In this study, we contained the dynamic rupture using a Teflon VS surface treatment on a 760 mm long PMMA sample and used a bare PMMA/PMMA section as a VW asperity. We investigated the slip behavior in relation to L/h^* by adjusting both the size L of the VW patch and the applied normal stress (σ_n) (since $h^* \sim 1/\sigma_n$, see Section 2). We observed aseismic slip at $L/h^* < 2$, periodic slip at $2 < L/h^* < 6$, and non-periodic at $L/h^* > 10$. Furthermore, we compared the contained and partially contained slip behavior to that of a free fault without VS material on the ends.

3.3. Theory of nucleation length

The behavior of fault systems is frequently modeled using rate-and-state friction (RSF), an empirical relationship, expressed as (Dieterich, 1979):

$$\mu = \mu' + a\ln\frac{V}{V'} + b\ln\frac{V'\theta}{D_c} \tag{3.1}$$

where μ is the friction coefficient, a and b are constitutive RSF parameters, V is the slip velocity, μ' is the reference friction coefficient, V' is the reference slip velocity, θ is a state variable related to the contact age, and D_c is the characteristic slip weakening distance. The aging law, which captures the process of contact healing (Marone, 1998), is:

$$\frac{d\theta}{dt} = 1 - \frac{V\theta}{D_c}, \tag{3.2}$$

though other forms of Equation 3.2, such as the slip law, are also common. For the steady-state sliding ($d\theta/dt = 0$) and $V\theta/D_c = 1$, Equation 1 reduces to

$$\mu = \mu' + (a - b)\ln\frac{V}{V'}. \tag{3.3}$$

When considering fault stability, the factor (a–b) plays a crucial role (Dieterich &

Kilgore, 1994; Marone, 1998; Scholz, 1998). When (a–b) is greater than 0, the fault exhibits velocity-strengthening (VS) behavior, which acts to inhibit seismic stick-slip events. Conversely, when (a–b) is less than 0, it displays velocity-weakening (VW) behavior. In VW faults, the stability of the slip behavior is governed by the system stiffness, k, and the critical stiffness, k_c (Rice & Ruina, 1983; Ruina, 1983), where

$$k_c = \frac{\sigma_n(b-a)}{D_c} \quad . \tag{3.4}$$

The slip behavior is considered unstable when $k/k_c < 1$ and stable when $k/k_c > 1$. Considering the stiffness of a fault embedded in a material with shear modulus G, the critical nucleation length, h^* is inversely proportional to the critical stiffness:

$$h^* = \frac{G}{k_c} = \frac{GD_c}{\sigma_n(b-a)} \tag{3.5}$$

An alternative expression of h^* contains the parameter $R_b = (b–a)/b$ (Ampuero & Rubin, 2008; Rubin & Ampuero, 2005)

$$h^*_\infty = \frac{h^*}{\pi R_b} = \frac{bGD_c}{\pi\sigma_n(b-a)^2}. \tag{3.6}$$

3.4. Materials and Methods

3.4.1. Sample and experimental setup

Two PMMA blocks were loaded with the biaxial machine shown in Figure 3.1a and previously described in detail (Cebry & McLaskey, 2021; Mclaskey & Yamashita, 2017). In this study, the moving block has the dimensions of 760 mm by 203 mm by 38 mm in x, y, and z directions, respectively, and the stationary block has the dimensions of 790 mm by 152 mm by 38 mm in x, y, and z directions, respectively. The PMMA ($G_{PMMA\_dynamic} \approx 2$ GPa) is more compliant than granite rock ($G_{rock\_dynamic}$

≈ 30 GPa) and is used for the experiments, so that, elastically, we can simulate ~11 m of rock (760 mm * $G_{rock\_dynamic}$ / $G_{PMMA\_dynamic}$). Normal stress was applied to the fault using four hydraulic cylinders and shear stress was applied with a fifth cylinder located at forcing end (i.e., North, N). The opposite side of the sample is called the leading end (i.e., South, S).

3.4.2. Sensors and instrumentation

As depicted in Figure 3.1a, local fault slip was measured using eight eddy current sensors attached with hot glue, located at 100 mm intervals in the x-direction (E1 to E8). Each eddy sensor measures the gap between a probe and a steel target at a resolution of ~0.15 μm and 20 kHz sampling rate. To measure the local slip of the fault, the probes were attached to the stationary block and the steel targets were glued to the moving block. Four Piezoelectric sensors (Panametrics, V103) were mounted on the surface of the stationary block, situated 30 mm away from the fault in the y-direction, with a spacing of 200 mm in the x-direction (P1 to P4). These piezoelectric sensors were capable of capturing ground motion in the z-direction of the PMMA blocks. The signal was continuously recorded at 20 kHz and also recorded in triggered mode at 2 MHz for 50-ms-long data blocks. The sample-average shear and normal stresses applied to the interface were calculated from hydraulic pressure measurements in the hydraulic cylinders.

3.4.3. Initial sample preparation

The fault surfaces of the moving and stationary blocks were prepared by fly cutting in a mill to first make flat surfaces and then roughening them with 80 grit abrasive. Those blocks were then positioned in the biaxial machine, subjected to a normal stress σ_n = 16 MPa, and sheared at ~3 μm/s for 2.5 mm of slip. This shearing was repeated twice with realigned moving blocks. Finally, the fault surfaces of both blocks were washed with water.

3.4.4. Teflon surface treatment

To prepare the heterogeneous fault sample, the entire fault area of both blocks was first covered with Teflon (Taegatech, PTFE tape, 0.813 mm (0.032 in) thickness and 50.8 mm (2 in) wide), affixed using cellophane tape on the top and bottom of the PMMA blocks. To prevent the two Teflon-covered PMMA surfaces from sticking together, plastic wrap (GLAD, Clingwrap) was placed between them. The assembly was then subjected to σ_n = 16 MPa normal stress and sheared for 1 mm to adhere the Teflon to the PMMA, after which the Teflon layer was carefully removed on part of the fault to create the desired size of the bare PMMA patch to make a single asperity (Figures 3.1b and 3.1c). The prepared specimen was then placed in the testing machine, with plastic wrap inserted only at the Teflon patches.

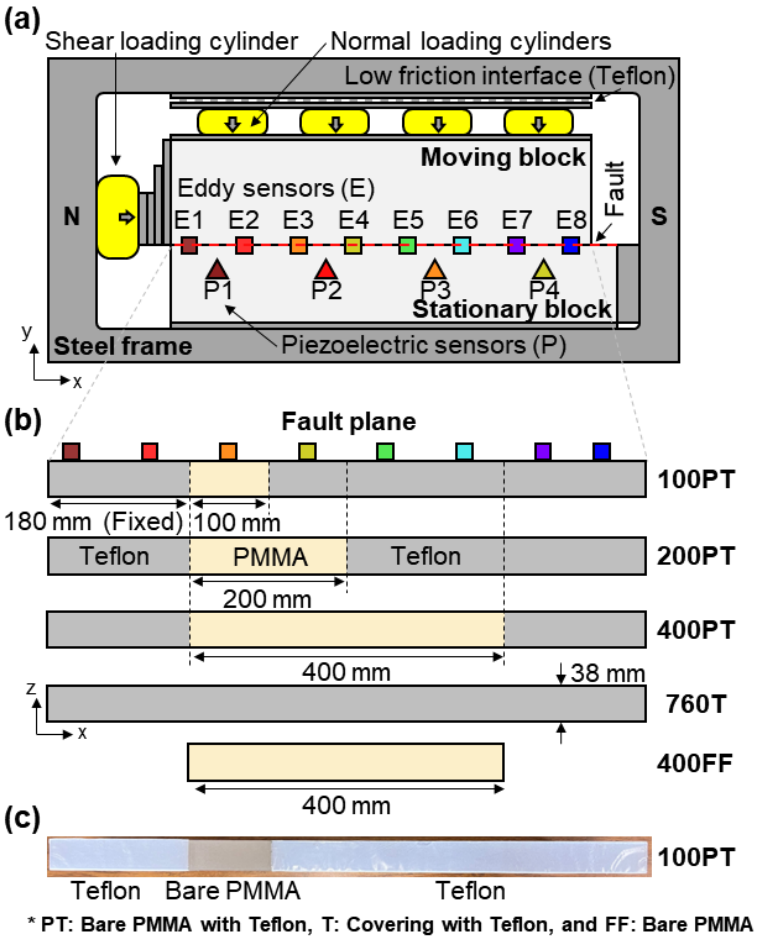

Figure 3.1. The biaxial experimental setup and various samples. (a) Schematic diagram of the biaxial apparatus showing the sensor locations and the moving and stationary PMMA blocks subjected to shear and normal stresses. (b) Side views showing the fault plane with the dimensions of the bare PMMA (VW) and Teflon (VS) patches for different experimental configurations. (c) Photograph showing the Teflon on the moving block after experiment 100PT.

The friction properties of the Teflon/plastic wrap interface were determined from a sample where the entire fault area was Teflon/plastic wrap (760T in Figure 3.1b). Some evolution of friction (i.e., a run-in phase) was observed with cumulative slip, but properties stabilized after ~4 mm of slip to a VS behavior, as shown in Figure 3.A1. We found $(a–b) \approx 0.0025$ at $\sigma_n = 2$ MPa, and the interface became more velocity neutral with increasing σ_n such that $(a–b) \approx 0.001$ at $\sigma_n = 16$ MPa. The friction

coefficient derived from the sample-averaged shear and normal stresses of Teflon ranges from 0.05 to 0.08 (Figure 3.A1c). In contrast, the friction coefficient for bare PMMA, ~0.7 (see Table 3.1, $\tau_{mech\_max}/\sigma_{n\_max}$), is ~10 times higher compared to that of the Teflon patch.

3.4.5. Experimental Procedure

To promote consistent results, we conducted a run-in phase before all experiments involving Teflon (see details in Figure 3.A1). After the desired σ_n was applied (ranging from 2 MPa to 16 MPa), the sample was sheared for ~4 mm before recording data. All experiments were loaded with an electric pump (ReaXus LS-Class, TELEDYNE ISCO) at a constant long-term slip rate of ~3 μm/s. To help distinguish between the effects of σ_n and any effects of cumulative wear of the interface, experiments with a given Teflon-PMMA geometry were conducted in the sequence: 4 MPa, 8 MPa, 2 MPa, and 16 MPa.

3.4.6. Free fault (400FF)

To directly compare our experiments with rupture contained by VS Teflon to a case with free end conditions, we also conducted experiments using a bare PMMA moving block of length 400 mm (400FF) without Teflon covering the ends (Figure 3.1b). Thus, configuration 400PT and 400FF have the same asperity size L and the same h^*. For 400 FF, we attached four Eddy sensors and four Piezoelectric sensors to the block, utilizing the same sensor geometry as the 400PT setup.

3.4.7. Digital Image Correlation (DIC)

The Digital Image Correlation (DIC) technique was adopted to measure strain along the fault (Figure 3.S1). Red speckles were painted on a white background painted on the surface of the moving block. Images were taken using a camera (Nikon, D850) with a resolution of ~93 μm/pixel. A reference image (i.e., undeformed image) was taken while the sample was at σ_n = ~0.1 MPa and deformed images were captured close to the peak shear stress, measured from the hydraulic pressure in the shear loading cylinder. 2D cross-correlation was used to match speckles between the reference and deformed images. This was used to create a deformation field and strain fields were derived from the deformation (see details in Figures 3.S1b and 3.S1c). The shear and normal stresses were calculated using Hook's law for plane strain, assuming Young's modulus, E_{PMMA_static} = 2.3 GPa and Poisson's ratio, ν = 0.3. We achieved sub-pixel resolution by upsampling by a factor of 20. Assuming a minimum resolvable displacement of ±4.7 μm/pixel, we estimate a minimum resolvable normal stress and shear stress of ±0.6 MPa and ±0.1 MPa, respectively (Figure 3.S1). These values are consistent with Cebry et al. (2023) who conducted DIC analysis with similar parameters.

3.5. Results

3.5.1. Example of slip behavior

We first present an example of a typical stick-slip sequence in order to define parameters and illustrate the general results. Figures 3.2a, 3.2b, and 3.2c show the slip, ground motion, and the sample-average shear stress (τ_{mech}) derived from hydraulic pressure in the shear cylinder from the 100PT experiment at σ_n = 8 MPa. Note that τ_{mech} is computed by dividing the force supplied by the shear cylinder by the fault area (760 mm x 38 mm). Stick-slip events are defined as the sudden drop of shear stress ($\Delta\tau_{mech}$) accompanied by rapid fault movement (Figures 3.2a and 3.2c). Notably, the sensor E3 moves more than other sensors, as it is located in the bare PMMA region (inset in Figure 3.2a). The drop in $\Delta\tau_{mech}$ does not correspond to the abrupt slip of sensor E3 (inset in Figure 3.2c). It decreases more gradually with time due to accelerated slow slip near the forcing end (E1). The period between stick-slip events is referred to as the interseismic period and the recurrence time (T_r) denotes the time between successive stick-slip events. Ground motion during each stick-slip event is captured by four piezoelectric sensors (e.g., P1, P2, P3, and P4) as shown in Figure 3.2b. The sensor P2 first detects the ground motions (inset in Figure 3.2b) since it is closest to the bare PMMA region (Figure 3.1a).

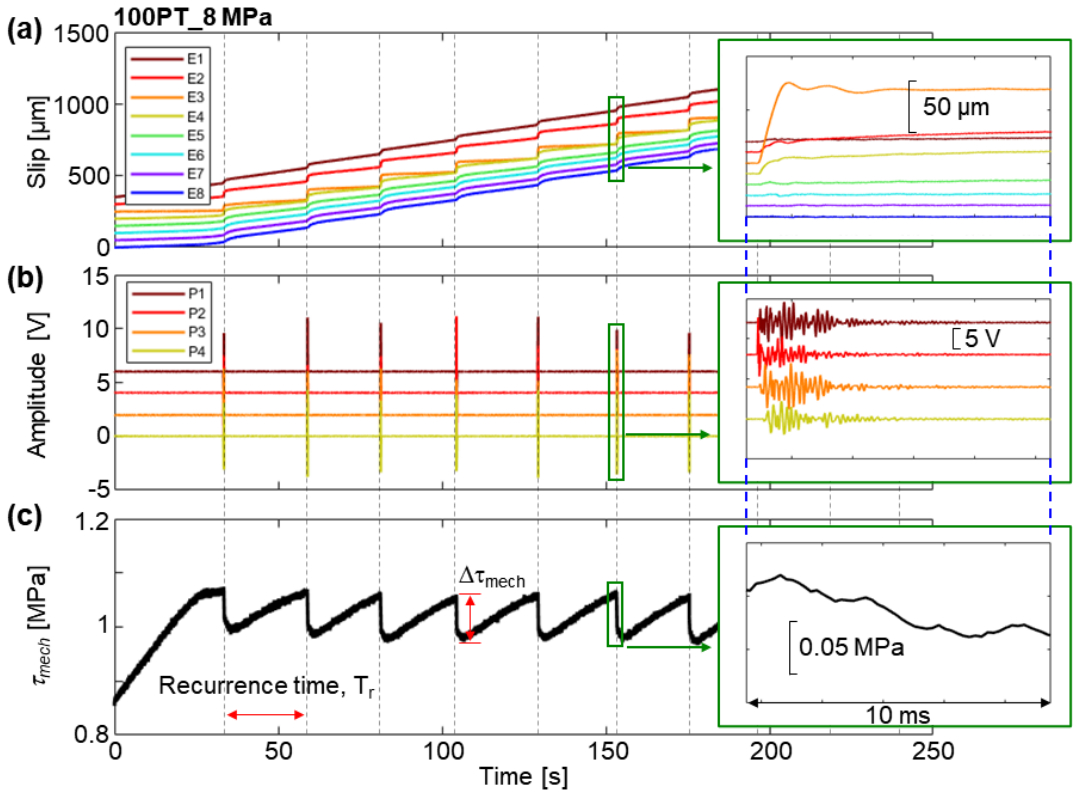

Figure 3.2. Representative behavior including (a) local fault slip, (b) acoustic signals, and (c) sample-average shear stress (τ_{mech}) of 100PT at σ_n = 8 MPa. The sudden drop of shear stress associated with a slip event is denoted $\Delta\tau_{mech}$. The stick-slip events are indicated by dotted vertical lines and the time interval between events is referred to as the recurrence time, T_r.

Figure 3.3 presents the evolution of the τ_{mech} over time for 100PT at 2 MPa, 4 MPa, 8 MPa, and 16 MPa normal stresses. Note that the scale of time and shear stress is different for each normal stress level. At 2 MPa normal stress, the shear stress remains constant at ~0.2 MPa, without showing any stick-slip events. In contrast, at 4 MPa normal stress, it starts to show slow slip events. The T_r and $\Delta\tau_{mech}$ increase with increasing normal stress. Notably, the sample undergoes regular and periodic slip cycles at σ_n = 4 MPa and 8 MPa, whereas the sample behavior is non-periodic and more variable at σ_n = 16 MPa.

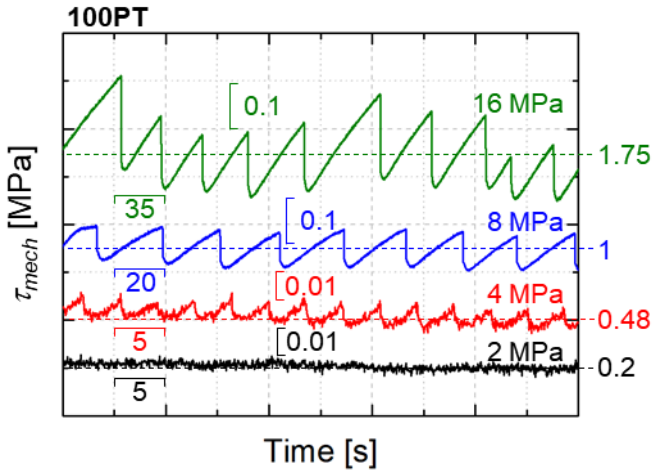

Figure 3.3. The τ_{mech} with time of 100PT under different normal stresses. Note the different time and amplitude scalebars and reference shear stress (dotted line) for each test. As the normal stress increases, L/h* increases, and the sample behavior transitions from steady sliding (2 MPa) to periodic slow (4 MPa) and fast (8 MPa) slip events, to aperiodic sequences (16 MPa).

Figures 3.4a to 3.4c present examples of the spatial distribution of slip over five consecutive stick-slip cycles. Closely spaced pink and purple bands indicate slower slip while widely spaced pink and purple bands indicate faster slip. The black lines show the slip distribution plotted every 100 μs to show the rapid slip during stick-slip events. A low normal stress and a small bare PMMA patch (e.g., 200PT with 4 MPa normal stress) shows periodic slip (Figure 3.4a). However, at higher normal stress (16 MPa), Figures 3.4b and 3.4c show non-periodic sequences.

Figures 3.4d to 3.4f show the slip rate derived from the same Eddy current sensor data shown in Figures 3.4a to 3.4c. The loading rate at the forcing end (E1) matches our applied loading rate and remains constant at ~3 μm/s (yellow dotted line) during the interseismic period regardless of the normal stress and PMMA patch sizes. The shear loading rate is known to influence the slip nucleation process (Guérin-Marthe et al.,

2019; Yoshihiro Kaneko et al., 2016; Xu et al., 2018), so this constant slip rate at E1 helps ensure a constant loading rate on the bare PMMA patch and more consistent conditions for the nucleation process. During the interseismic period, the slip rate in the bare PMMA region (e.g., E3 and E4) is lower compared to the Teflon region (Figure 3.4d) but gradually increases before each stick-slip event. During the slip event, it reaches ~100 mm/s. For experiments at higher normal stress, the slip rate in the bare PMMA region is even lower during the interseismic period (Figure 3.4e). In the 400PT experiment, it is clear that interseismic slip rates are variable across the VW asperity, with the lowest slip rate occurs closer to the center of the bare PMMA region, at E4 (Figure 3.4f).

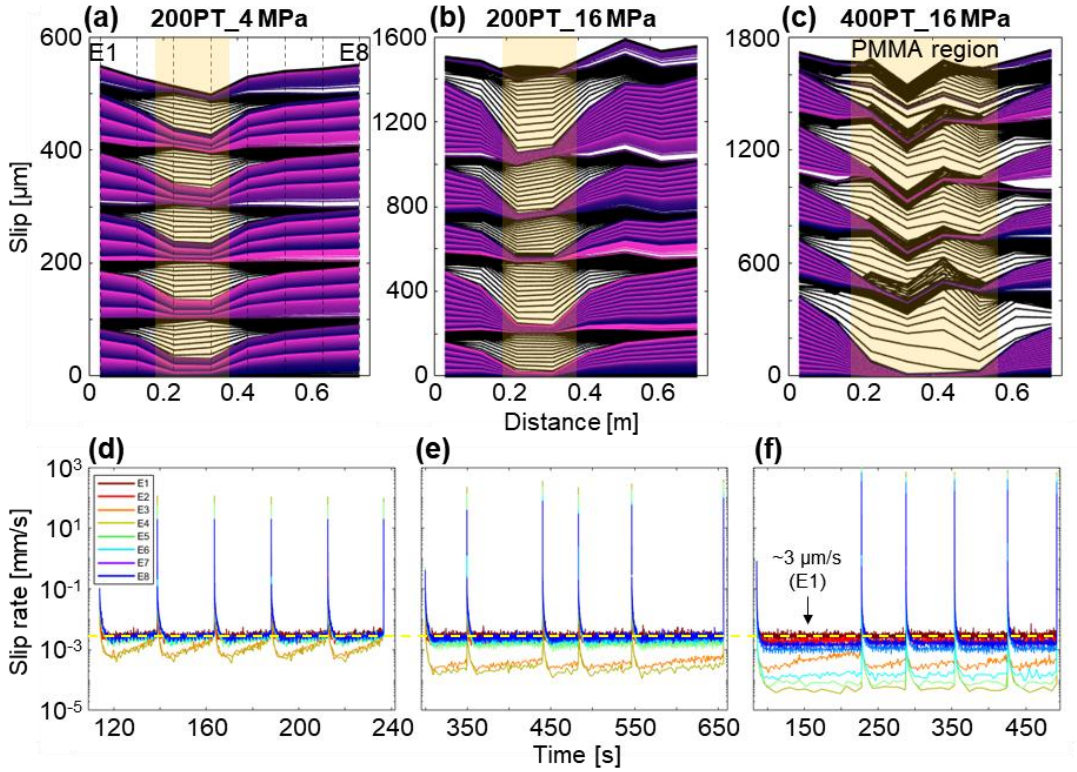

Figure 3.4. Accumulated slip along the fault for five stick-slip cycles. (a-c) The distribution of slip along the fault from E1 to E8. For the pink and purple lines, a line is plotted every 100 ms with a 10 s color cycle. The black lines show slip distribution plotted every 100 μs during a slip event. The yellow shaded area indicates the location of the PMMA patch. Experiment names and σ_n levels are indicated above each plot. (d-e) The slip rate over the five stick-slip cycles, derived from the same data as in (a-c). Stick-slip events show up as spikes of high slip rate. During the interseismic period, the slip rate near the forcing end (E1) remains constant at the driving rate of ~3 μm/s (yellow dotted line), while the slip rate on the asperity is lower, indicating relative locking and accumulation of slip deficit.

3.5.2. Maximum slip rate

Figure 3.5 shows the maximum slip rate of each Eddy sensor along the fault throughout the entire stick-slip cycle. Each data point shows the average maximum slip rate based on 6 to 12 stick-slip events. Following previous work, we set a boundary of 10 mm/s to differentiate between seismic (or dynamic) slip and aseismic slip (McLaskey, 2019; Wu & McLaskey, 2019). The distribution of the maximum slip

rate exhibits a symmetric configuration, with its peak at the center of the bare PMMA patch. For the 100PT_4 MPa, seismic slip is observed within the bare PMMA region, while the Teflon patch shows aseismic slip. As the normal stress increases or the size of the bare PMMA patch increases, seismic slip extends further and further into the Teflon region. However, even when the entire fault slips at seismic rates, the Teflon regions near the sample ends are still limiting the slip rate. This contrasts with the experiment with free ends and no Teflon, 400FF_8 MPa, which shows consistent slip rates across the entire fault, or even increased slip rates at the sample ends.

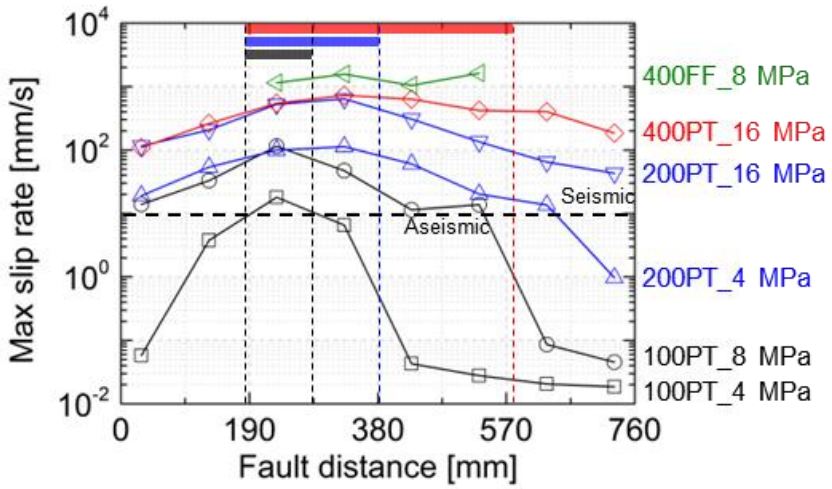

Figure 3.5. The maximum slip rate of each sensor during the stick-slip event with respect to the fault distance. Note that black, blue, and red shaded areas present the bare PMMA region in 100PT, 200PT, and 400PT, respectively.

Figure 3.6a illustrates the maximum slip rate measured anywhere on the fault, $\dot{D}_{max}$, during each stick-slip event and how this changes as a function of normal stress. At 2 MPa normal stress, both 100PT and 200PT exhibit aseismic slow slip events, with $\dot{D}_{max}$ of ~20 μm/s (still far larger than the applied loading rate of 3 μm/s). The results demonstrate an increase of the $\dot{D}_{max}$ as the normal stress increases.

Figure 3.6b shows the same data plotted against L/h^*. The $\dot{D}_{max}$ roughly collapses to a single curve. In this study, we only controlled the dimensions of the asperity while keeping the frictional properties of the material constant. Therefore, we assumed that $G_{dynamic}$, D_c, and (b–a) remain the same and, therefore, h^* is only influenced by the normal stress (Equation 3.5). From previous studies of the friction parameters of glassy polymers, we assume (b–a) ≈ 0.005 and D_c ≈ 0.35 μm (Lu, 2009), such that $G_{dynamic} \cdot D_c/(b–a)$ ≈ 140 mm·MPa. From this, we find that the transition from seismic to aseismic slip occurs at L/h^* ≈ 2.8. With increasing L/h^*, $\dot{D}_{max}$ gradually increases from ~20 mm/s to ~1 m/s at L/h^* ≈ 45. Figure 3.6b also compares our experimental results to the numerical simulations of Barbot (2019) (green arrow). Variations in the geometry and boundary conditions of Barbot's (2019) model (such as anti-plane strain versus 2D fault) resulted in variations in the values of L/h^* at the boundary between seismic and aseismic slip; however, the general trend in $\dot{D}_{max}$ remains similar to our experimental findings.

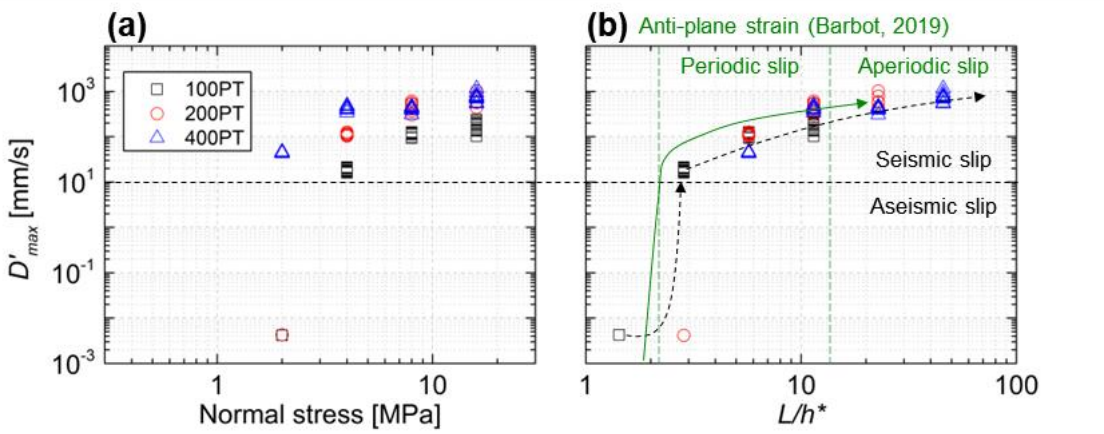

Figure 3.6. Maximum slip rate at the PMMA patch with various PMMA patch sizes, showing its relationship with (a) the normal stress and (b) L/h^*. Each symbol is a slip event. We assumed that h^* is 140 mm at 1 MPa. We compared our results (symbols and black dashed lines) to those from the anti-plane strain numerical simulation results from Barbot, (2019) in green.

3.5.3. Variation in recurrence time and seismic moment with L/h^*

Figure 3.7a depicts the recurrence time, T_r, against L/h^* for the same experiments as shown in Figure 3.6, except experiments that exhibit aseismic slip are not plotted. As L/h^* increases, the recurrence time increases and the variation in recurrence time also increases. The inset in Figure 3.7a shows the normalized standard deviation of T_r (Norm_SD) defined, for each sequence of slip events, as the standard deviation of the T_r divided by the average T_r. For $L/h^* < 6$, the Norm_SD is less than ~0.06, indicating highly periodic slip behavior. However, for $L/h^* > 10$, the Norm_SD increases up to 0.75 indicating non-periodic slip. Based on these results, we denote the transition from periodic to non-periodic slip behavior at $L/h^* \approx 8$, although the Norm_SD results suggest that this specific transition might be arbitrary.

Figure 3.7b shows how the seismic moment, M_{0_seis}, obtained from the piezoelectric sensors, varies with L/h^*. M_{0_seis} is calibrated using a ball drop empirical Green's

function (see details in Figure 3.S2). Note the large reduction in seismic moment observed at low L/h^*, close to the boundary. In the 'non-periodic slip' region, we observe a greater variability in event sizes during the same test.

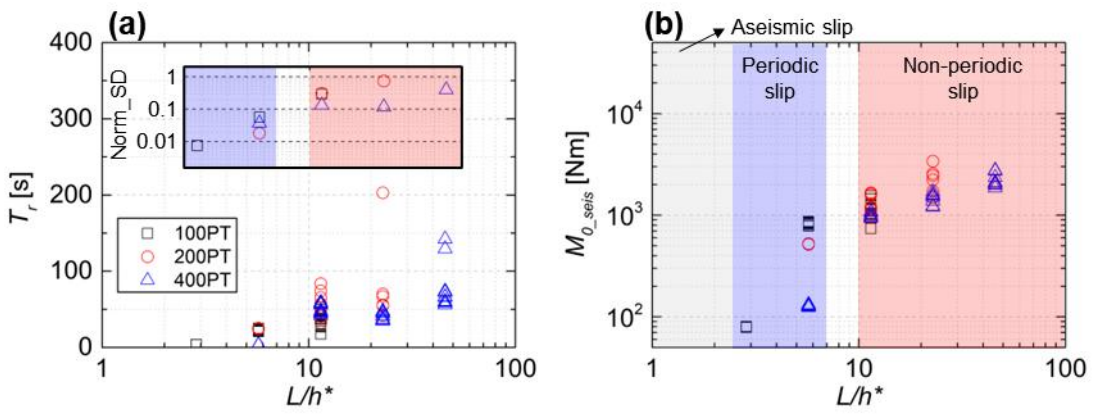

Figure 3.7. (a) Recurrence time against L/h^* for each stick-slip event in all tests. Inset shows the standard deviation (SD) of recurrence time for events in each test. (b) Seismic moment (from spectra of recorded ground motions) against the L/h^* for each stick-slip event. The area is divided into three regions: aseismic slip (gray shaded area with $L/h^* < 2$), periodic slip (blue shaded area with $2 < L/h^* < 6$), and non-periodic slip (red shaded area with $L/h^* > 10$).

3.5.4. Slip behavior of the free fault compared to the contained fault

To further investigate the effects of rupture containment with a VS region, we directly compared slip behaviors between a contained fault (CF, 400PT_8 MPa) and a free fault (FF, 400FF_8 MPa) with the same L and same h^*, described in Table 3.1. Values presented in the table are the average of many stick-slip events, along with minimum and maximum values in parentheses. A is the fault area. σ_{n_max} and τ_{mech_max} are the maximum sample-average normal and shear stresses, respectively, just prior to a slip event, derived from hydraulic pressure measurements. $F_{max} = \tau_{mech\_max} \cdot A$ is the maximum sample-average shear force. The parameters T_r and $\Delta\tau_{mech}$ were described

previously. $D_{avg\_dynamic}$ is the average dynamic slip expressed as

$$D_{avg\_dynamic} = \frac{1}{n}\sum_{i=1}^{n} D_{i\_dynamic} = \frac{1}{n}\sum_{i=1}^{n} \int_{t_1}^{t_2} \delta_i(t)dt, \quad (3.7)$$

where δ_i is the slip measured with the ith eddy current sensor when the slip rate exceeds 10 mm/s for 0.1 ms duration and n = 8 is the number of eddy current sensors, t_1 is when $d\delta/dt > 10$ mm/s, and t_2 is when $d\delta/dt < 10$ mm/s. The M_{0_mech} is modified from the standard M_0 = GAD expression (Aki, 1966), to be

$$M_{0\_mech} = G_{dynamic} W \int_0^{0.76\ m} D_{dynamic}(x)\, dx, \quad (3.8)$$

where W = 38 mm is the sample thickness and $D_{dynamic}(x)$ is the distribution of dynamic slip derived from the interpolation of $D_{i\_dynamic}$. M_{0_seis}, is determined from piezoelectric sensor measurements, as described in Figure 3.S2. Note that we analyzed 5 and 9 consecutive stick-slip events in FF and CF, respectively.

From Table 3.1, significant differences are observed despite them having the same VW patch size and h^*. Specifically, the mechanical properties such as T_r, $\Delta\tau_{mech}$, $D_{avg\_dynamic}$, and M_{0_mech} in the FF are found to be 6 - 11 times higher compared to the CF. However, the observed difference in M_{0_seis} is only 2.3 times.

Table 3.1. Comparison between free fault (FF, 400FF_8 MPa) conditions and contained fault (CF, 400PT_8 MPa).

	A [cm^2]	σ_{n_max} [MPa]	τ_{mech_max} [MPa]	F_{max} [kN]	T_r [s]	$\Delta\tau_{mech}$ [MPa]	$D_{avg\_dynamic}$ [μm]	M_{0_mech} [kN·m]	M_{0_seis} [kN·m]
FF	152.4	8.2 (8.0-8.3)	5.7 (5.4-5.9)	87 (83-90)	259 (236-280)	3.1 (2.6-3.4)	1119 (910-1274)	39 (32-45)	3.4 (2.0-3.8)
CF	289.6	7.8 (7.7-7.8)	2.6 (2.6-2.7)	77 (76-78)	41 (35-47)	0.36 (0.3-0.4)	103 (71-123)	6.2 (4.3-7.3)	1.5 (1.2-1.7)
FF/CF	**0.53**	**1.1**	**2.2**	**1.1**	**6.4**	**8.6**	**10.8**	**6.3**	**2.3**

Figure 3.8 shows the Digital Image Correlation (DIC) results of both the contained fault and the free fault (see method in Section 3.4.7). In addition to the reference image, deformed images were captured when only normal stress was applied to the block (dashed line in Figure 3.8a) and at τ_{mech_max}, prior to the occurrence of a stick-slip event. When τ_{mech_max} was applied, as depicted by the solid lines, the normal stress decreased near the forcing end and increased at the leading end due to the shear-force-induced torque in this single direct shear biaxial setup. Nevertheless, in the CF case, a nearly constant normal stress is observed within a bare PMMA region since it is sufficiently from the sample ends. The shear stress distribution in the FF resembles the normal stress distribution because the friction properties are uniform along the fault (Figure 3.8b). However, the shear stress at both ends in the CF is comparably lower than in the middle because the Teflon has a lower friction coefficient than the bare PMMA interface. Although the center of the sample involves the same bare PMMA region, the stress levels are lower in the CF case than in FF (Figure 3.8c).

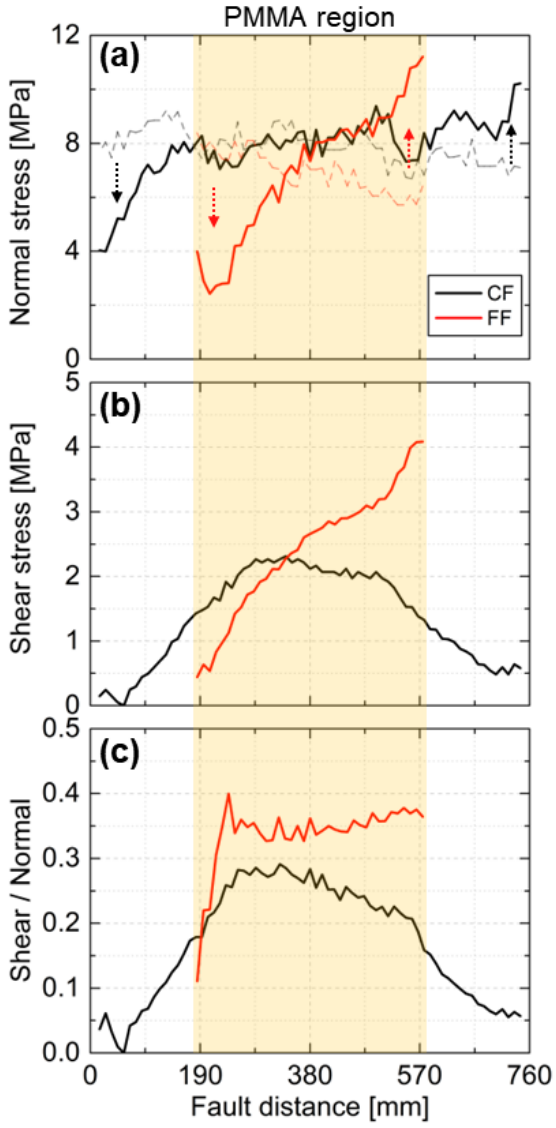

Figure 3.8. Stress distributions obtained by DIC under 8 MPa normal stress. (a) Normal stress distribution at τ_{mech_max}. Note that the dotted lines are the normal stress when the only normal stress was applied without shear stress. (b) Shear stress distribution at the τ_{mech_max}. (c) Friction coefficient of shear and normal stresses. The yellow shaded area is the PMMA region.

3.6. Discussion

In these experiments, instead of employing a sample with uniform VW properties, we introduced Teflon tape as VS patches at the fault ends to establish a more contained fault rupture condition (Figure 3.1). This experimental condition corresponds more

closely to the condition of previous numerical simulations (Barbot, 2019; Cattania, 2019; Chen & Lapusta, 2009; Y. Kaneko & Lapusta, 2008; Lapusta & Liu, 2009; Lapusta & Rice, 2003; Lui & Lapusta, 2016, 2018). Our setup is somewhat similar to experimental studies that utilized fault gouge, which is effective for the confinement of the rupture (Bedford et al., 2022; Buijze et al., 2021); however, differential compaction of different gouge materials can produce heterogeneous normal stress, and we have shown that the normal stress is relatively uniform within the VW patch in our experiments (Figure 3.8a). We altered the size of the bare PMMA region and normal stress to systematically control L/h^* on the fault system. Our observations closely match numerical studies and highlight a range of slip behaviors depending on L/h^*, ranging from aseismic slip at low L/h^* to non-periodic slip at high L/h^*. Also, we found significant differences in slip behavior, depending on different fault constraint conditions (e.g., FF and CF conditions) even within the same L/h^* values.

3.6.1. Various slip behaviors as a function of L/h^*

Our results show a distinct transition in behavior (Transition 1) from aseismic slip at low L/h^* to seismic slip at higher L/h^* and other, less-well-defined boundary (Transition 2) at higher L/h^* where periodic slip events become more aperiodic. In previous laboratory studies, Transition 1 was investigated by changing the stiffness ratio of the system, k/k_c (see Section 3.3) within the range of ~0.5 to ~1.1 which can be converted to $0.9 \leq L/h^* \leq 2$ since $k_c/k = L/h^*$ (Leeman et al., 2016; Scuderi et al., 2016; Veedu et al., 2020). All of those studies employed homogeneous fault properties with free end conditions. Transition 1 was found to occur at $L/h^* \approx 1$ - 1.3, which is

similar to our observation of $L/h^* \approx 2$ despite differences in boundary conditions between previous experiments and our contained ruptures. Note that all of these quantitative estimates of Transition 1 are limited by our poor ability to quantitatively estimate h^* since direct measurement of friction parameters (b–a) and D_c for bare PMMA are not achievable in our experimental setup. Inaccurate h^* would simply shift the data along the x-axis in Figure 3.6b and Figure 3.7, but would not affect the general trends. Near Transition 1, all studies found sharp changes in $\dot{D}_{max}$ in response to minor changes in L/h^*. For example, we find $\dot{D}_{max} \sim 4$ μm/s at $L/h^* = 1.4$ and ~10 mm/s at $L/h^* = 2.8$ (Figure 3.6b). For Transition 2, a bifurcation in slip behavior (e.g., alternation of slow and fast slips) has been reported (Mei et al., 2022; Veedu et al., 2020) under a narrow range of conditions. In addition to L/h^*, Luo & Ampuero (2018) found the relative strength parameter, $\alpha = (b–a)_{VW}/(a–b)_{VS}$, to be an important factor in determining slip behavior. We assumed that $(b–a)_{VW}$ for bare PMMA remains constant regardless of normal stress, while $(a–b)_{VS}$ for Teflon decreases as normal stress increases (Figure 3.A1). As a result, α ranges from 1.9 to 3.3 at $L/h^* = 5.6$, placing it within the P-instability region. In this area of parameter space, the limited variation of α does not significantly alter the slip behavior in comparison to changes in L/h^*.

Fault stability has also been investigated using numerical simulations, which commonly model a single VW asperity bounded by the VS materials (Barbot, 2019; Cattania, 2019). Cattania (2019) reported results in terms of h^*_∞ and used a = 0.015 and b = 0.02 ($R_b = 0.25$) for the analysis, which results in $h^* \approx 0.8h^*_\infty$ (Equation 3.6). That study reported Transition 1 at $L/h^* \approx 0.8$ and Transition 2 near $L/h^* \sim 5$, with increasing numbers of earthquakes per supercycle progressively increasing for $L/h^* \geq$

~5 (Cattania, 2019). Barbot (2019) found Transition 1 at $2 < L/h^* < 6$, depending on boundary conditions, and Transition 2 at $L/h^* \approx 6$, but this varied depending on R_b (Barbot, 2019). The above numerical results are in reasonable agreement with our observations (Transition 1 at $L/h^* \approx 2$ and Transition 2 at $L/h^* \approx 8$). The two transitions are evident across both numerical and experimental studies, and this suggests that L/h^* is a reliable parameter to determine a sample behavior.

3.6.2. Contained rupture versus free fault rupture

In this Section, we discuss the effect of slip behavior between the CF, where a VW patch is contained by VS material and the FF, where the VW patch is bounded by free surfaces. We made the same area of the bare PMMA for both the FF and CF tests. In terms of strength, we observed that F_{max} is 13 % larger for FF while the normal stress is only 5 % larger (Table 3.1). This shows that not only did the Teflon patches added in the CF case provide minimal shear resistance, they acted to weaken the surrounding VW fault sections. The DIC results also demonstrate this effect when examining the ratio of local shear stress to normal stress in the bare PMMA region: FF condition exhibits an average value of ~0.35, whereas the CF condition has a lower average value of ~0.25 (Figure 3.8c). We also found that the sample-average friction coefficient in these heterogeneous tests is generally comparable to or slightly less than the area-averaged mixture of the friction coefficients of bare PMMA (0.7) and Teflon (~0.07). Thus, the addition of the weak VS material effectively weakened the nearby VW material. In nature faults, VW gouges (e.g., Quartz and Calcite) exhibit friction coefficient of ~0.7, while VS gouges (e.g., Clay and Talc) exhibit friction coefficient

of ~0.2 (Bedford et al., 2022; Giorgetti et al., 2015). The friction coefficients of those natural materials are similar to those of PMMA and Teflon, thereby implying that similar asperity erosion patterns could be found in natural faults.

This can be at least partially explained by the sliding during the interseismic period. In the FF case, the entire fault remains locked during the interseismic period (Figure 3.S3), whereas in the CF case, the VW region creeps at 0.06 - 0.6 μm/s. Numerical simulations (Chen & Lapusta, 2009) have also shown how creep in the VS region can penetrate into the VW region and "erode" the asperity and mitigate the accumulation of shear stress relative to areas that are fully locked.

We note that the local friction coefficient estimated by DIC (μ_{DIC}) is significantly lower than the sample-average friction coefficient (μ) estimated from the hydraulic pressure measurements. For example, the 400FF_8MPa experiment produced $\mu_{DIC} \approx 0.4$ (Figure 3.8c) while $\mu \approx 0.7$ (Table 3.1). Our estimate of μ is a slight overestimate of the true friction coefficient on the fault, μ_{fault}, due to the contribution from the Low Friction Interface (LFI, see Figure 3.1a) which likely has a friction coefficient $\mu_{LFI} \approx 0.02$ between Steel and Teflon (Dieterich & Kilgore, 1994), the sample-average friction coefficient of the fault ($\mu_{fault} \approx 0.68 = \mu - \mu_{LFI}$). Additionally, μ_{DIC} might be an underestimate since the measurements are made 20 mm from the fault (Figure 3.S1) and we found that the measured shear strain decreases with increasing distance from the fault, especially near the forcing end of the sample. However, these effects don't seem to explain the large differences between $\mu_{DIC} \approx 0.4$ and $\mu \approx 0.7$. Despite this concern, our observations consistently show that the fault is weaker in the CF configuration than in the FF configuration.

The mechanical properties during slip events such as $\Delta\tau_{mech}$ and $D_{avg\_dynamic}$ are 8 - 10 times higher in the FF experiment compared to the CF. In this case, the Teflon appears to serve a dual purpose: it weakens the fault, as described above, and it also acts to arrest or decelerate slip during slip events by providing increased frictional resistance as the slip rate increases. Consequently, the presence of Teflon at both ends in the CF condition helps to reduce the amount of slip and the amount of $\Delta\tau_{mech}$ during slip events.

3.6.3. Rapid slip in VS regions causes imperfect containment

As shown in Figures 3.4a to 3.4c, the dynamic slip, (>10 mm/s) is primarily found in the bare PMMA region, but dynamic slip also extended into the VS patches. This is more evident in Figure 3.5, which delineates the $\dot{D}_{max}$ along the fault distance. At small L/h^* (i.e., 100PT_4 MPa) seismic slip is confined to the bare PMMA region, but with increasing L/h^*, the slip rate in the Teflon patches increases even to seismic slip rates (>10 mm/s). Although we used Teflon to contain the rupture to within the sample, it was not fully contained. Nevertheless, the presence of Teflon decelerated the slip in the region where it was applied. In contrast, in the FF condition, the slip rate can remain constant or even increase when it approaches the ends of the fault (see Figure 4 in Wu and McLaskey (2019) or Figure 3.5 in this study). In numerical simulations, it is also common to observe dynamic slip in VS regions next to VW regions, and the extent of dynamic slip in VS areas increases with an increase of L/h^* (Barbot, 2019; Cattania, 2019; Chen & Lapusta, 2009; Lapusta & Liu, 2009; Lui & Lapusta, 2016, 2018).

3.6.4. Comparison of mechanical moment and seismic moment

We calculated M_{0_mech} derived from mechanical measurements (Equation 3.8) and compared it to M_{0_seis} based on ground motions detected with the piezoelectric measurements. The ratio of M_{0_mech}/M_{0_seis} was 11.5 and 4.1 for the FF and CF conditions, respectively, reported in Table 3.1. Thus, the mechanical moment overestimated seismic moment in both cases, but particularly in the FF condition, indicating that the efficiency of seismic wave radiation with respect to the amount of slip was lower in the FF condition compared to the CF condition. This may be attributed to the CF condition inducing more abrupt variations in slip rate, which could enhance wave radiation efficiency with respect to the slip. Our results are consistent with those of Wu and McLaskey (2019) who found the M_{0_mech}/M_{0_seis} ~10 for complete rupture of a 3-m granite sample (i.e., FF conditions) and generally smaller values (1.5 - 4) for contained ruptures (i.e., CF rupture). Equation 3.8 is derived from a case where fault slip is zero over the entire perimeter of the rupture region. For the FF, the shear modulus G should be replaced in some way, by the effectively lower stiffness that the rupture feels from the loading apparatus compared to the case of completely contained rupture. When the rupture approaches a truly contained fault condition, M_{0_mech} / M_{0_seis} should approach unity.

The presence of the VS material on the fault ends does not guarantee a perfect contained fault condition, it is a closer approximation to the expected conditions of natural earthquakes than FF conditions, and this affects both the frictional behavior and seismic energy release. We encourage researchers to adopt the Teflon surface

treatment since it can help contain the rupture and reduce edge effects associated with the free surfaces at the ends of the sample. It also facilitates a more homogeneous normal stress distribution within the VW patch simply because it moves the VW patch away from the sample ends where nonuniform normal stress is common.

3.7. Conclusions

We performed biaxial experiments on a 760 mm PMMA sample and created contained rupture using a Teflon surface treatment to make as a VS barrier. We varied both the size of the bare PMMA region (L) and the normal stress on the sample to study the various slip behaviors in relation to L/h^*, which ranged from 1.4 to 45 in our experiments. Similar to previous studies, we observed behavioral changes with increasing L/h^* going from aseismic slip to periodic slip to non-periodic slip. These changes were also accompanied by an increase maximum slip velocity during the slip events. The fact that similar behavior is observed in a variety of numerical simulations and previous laboratory experiments, indicates that L/h^* is one of the most robust metrics for classifying the behavior of relatively isolated VW fault sections, even under somewhat varied boundary conditions.

Experimentally, the Teflon surface treatment proposed here offers a relatively simple method for containing laboratory earthquake ruptures. This practice moves seismic slip away from the sample ends, where a nonuniform distribution of normal stress often occurs during standard direct shear experiments. This promotes a more uniform normal stress distribution on the VW patch, which more closely aligns with the conditions observed in numerical studies. Teflon on the fault ends also reduces the

amplification of slip velocity that occurs when a dynamic rupture meets a free surface, and effect that is not expected for natural earthquakes whose ruptures are contained within the earth. By comparing the measured fault slip to the seismic moment calculated from measured ground motions, we found that uncontained ruptures associated with slip all the way to the free surfaces did not radiate seismic waves as efficiently, with respect to the slip, as did contained ruptures. The VS regions near the sample ends slowed down dynamic rupture, even if it did not always stop it completely, and this produced earthquake ruptures whose seismically estimated moment more closely matched their mechanically estimated moment.

Our experiments also provide insights into the interactions between VS and VW fault sections, showing that a weak, VS region weakens an adjacent VW region because interseismic creep in the VS region can penetrate into the VW section effectively causing "asperity erosion". Overall, this study significantly contributes to the understanding of basic slip behavior in relation to the L/h^*. It serves as a foundation for further experimental investigation into higher L/h^* (e.g., larger than 100), which more closely matches the behavior of large earthquakes on mature faults as explored in numerical studies (Michel et al., 2017; Sathiakumar & Barbot, 2021).

3.8. Appendix

We refer to the first ~4 mm of slip on the interface as a run-in phase since a constant τ_{mech} has not been reached, as shown in Figure 3.A1. When exploring if friction properties changed with longer-term displacement, we found that a run-in phase at a higher level of normal stress (i.e., σ_n = 16 MPa) was required to produce consistent results. To illustrate this, a set of six experimental runs are shown in Figure 3.A1, performed in the following order (2 MPa, 16 MPa, 4 MPa, 8 MPa, 2 MPa, and 16 MPa). The first two experiments are denoted "1st Exp" to distinguish them from others ("2nd Exp") performed at the same σ_n levels. By comparing the results at σ_n = 2 MPa between the 1st and 2nd experiments, it is evident that the friction coefficient and (a–b) significantly vary, whereas similar values were observed at 16 MPa (Figures 3.A1c and 3.A1d). The value of (a–b) gradually reduced with an increase in normal stress. This means that the slip behavior is changed becomes more velocity neutral with an increase in normal stress. Nonetheless, it shows VS slip behavior even at 16 MPa.

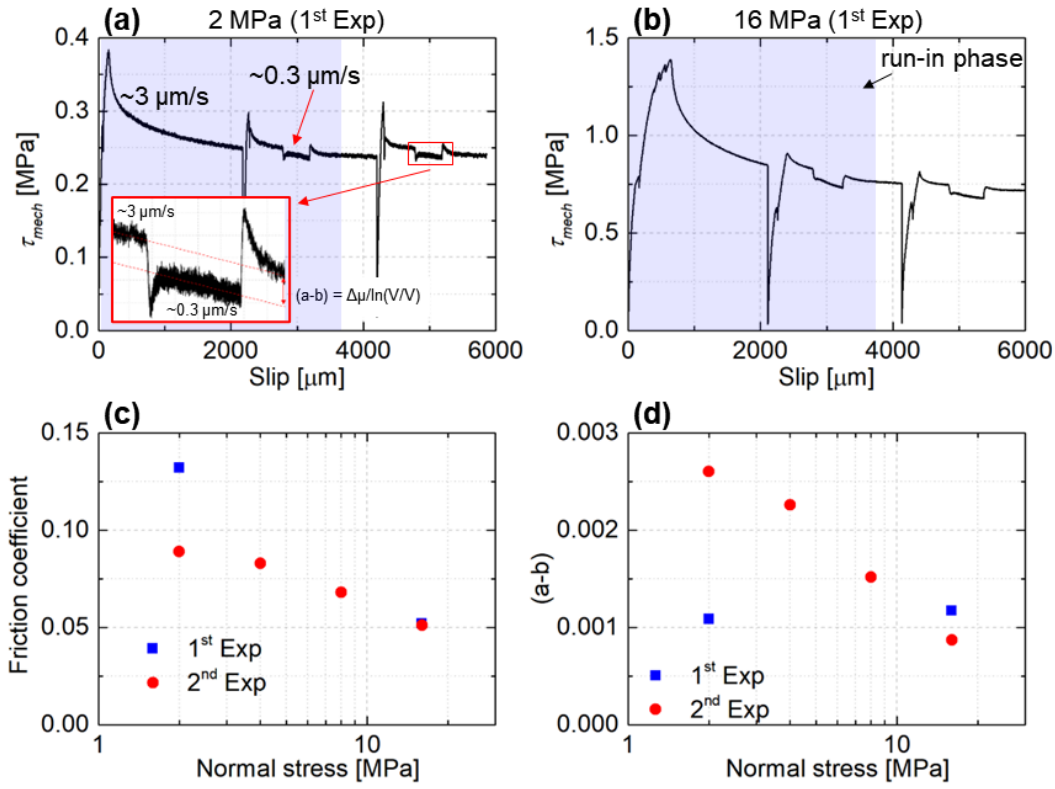

Figure 3.A1. Velocity step tests for experiments with 760T configuration (Figure 3.1b) where the Teflon surface treatment was applied to the entire 760 mm fault. (a-b) Friction curves show ~4 mm of slip is required before properties stabilize. The imposed loading velocity was alternated between ~3 um/s and ~0.3 um/s to obtain the RSF parameter. The shear stress was applied up to 2 mm, released, and then re-applied. (c) The friction coefficient found from sample-average shear and normal stresses and (d) RSF parameter (a–b) found from velocity step tests are shown at different normal stress levels.

3.9. Supplementary Figures

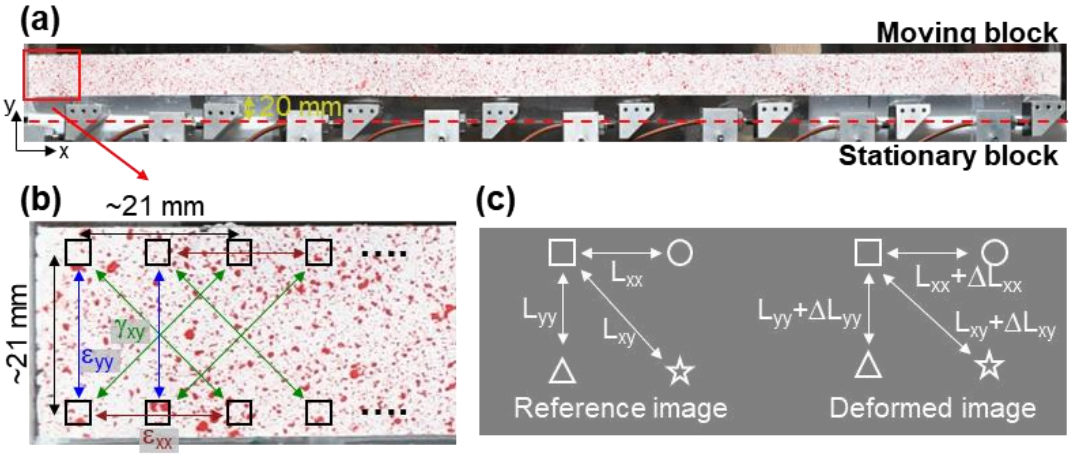

Figure 3.S1. (a) Top view of the 760 mm moving block with red speckles on a white background for DIC analysis. Note that the image was captured using a Nikon D850 camera with a resolution of 93 μm/pixel and the speckled region is located 20 mm away from the fault (red dashed line). (b) Zoomed-in image near the forcing end with black boxes showing the locations of sub images used for pixel tracking and for the calculation of strain in the x-, y-, and xy-directions. (c) The reference image was taken under ~0.1 MPa normal stress for strain calculation. The location of the reference white box can be identified in deformed blocks by using cross correlation between the reference image and the deformed image. For the calculation of the minimum strain in DIC, we assumed a resolution of ±1/20th of a pixel differential displacement between two boxes separated by 21 mm. The minimum normal strain (ε_{yy}) calculated is ±4.7 μm/21 mm ≈ ±2.2e-4 and the corresponding normal stress change is ±0.6 MPa. In the case of shear strain, the calculated shear strain (ε_{xy}) is ±3.3 μm/29.7 mm ≈ ±1.1e-4 and the corresponding shear stress change is ±0.1 MPa.

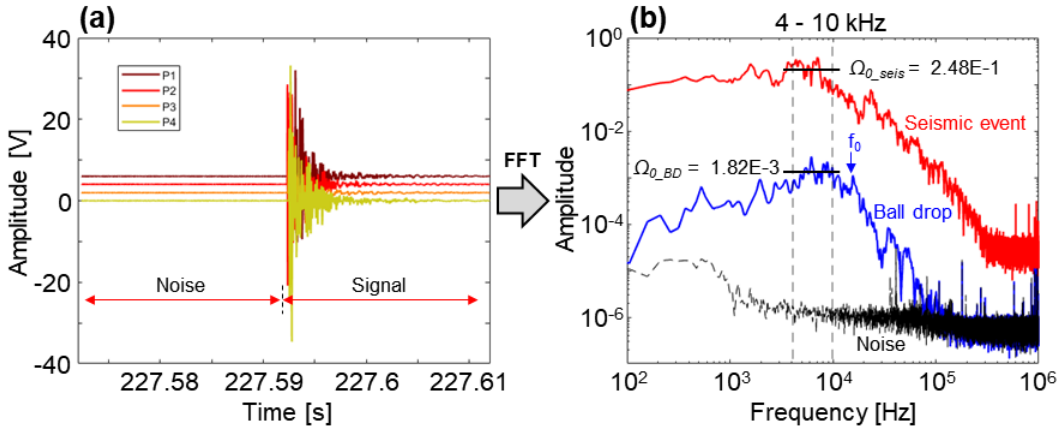

Figure 3.S2. An example of stick slip event recorded by piezoelectric sensors from 400PT_16 MPa. (a) Signal amplitude in the time domain. The time window for the noise and signal analysis is 19 ms for Fourier Transform. (b) Signal amplitude in the frequency domain obtained from Fourier Transform. Note that the spectra were generated using the average values from P1 to P4 sensors. The solid black line represents the average value between 4 kHz to 10 kHz and is used for the comparison between the ball drop and seismic event. The ball drop method was adapted to calibrate the ground motion of seismic events and the calibration process was detailed in the previous studies (Cebry & McLaskey, 2021; Wu & McLaskey, 2019).

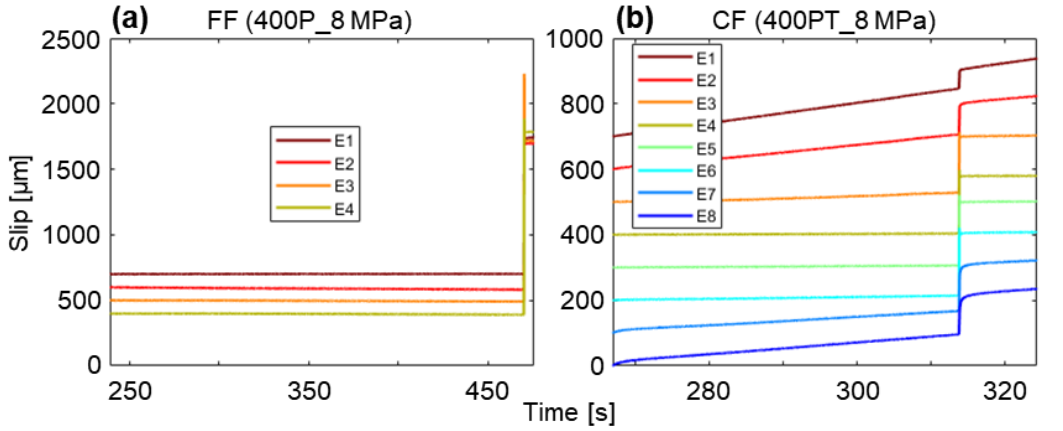

Figure 3.S3. Representative local fault slips during the interseismic period with stick slip events in (a) FF and (b) CF. In the free fault, the entire fault remains locked during the interseismic period. On the other hand, in the contained fault, the PMMA patch slowly creeps during this period.

REFERENCES

Aki, K. (1966). Estimation of earthquake moment released energy and stress-strain drop from G-wave spectrum. *Bulletin of the Earthquake Research Institute*.

Ampuero, J.-P., & Rubin, A. M. (2008). Earthquake nucleation on rate and state faults – Aging and slip laws. *Journal of Geophysical Research*, *113*(B1), B01302. https://doi.org/10.1029/2007JB005082

Barbot, S. (2019). Slow-slip, slow earthquakes, period-two cycles, full and partial ruptures, and deterministic chaos in a single asperity fault. *Tectonophysics*, *768*(July), 228171. https://doi.org/10.1016/j.tecto.2019.228171

Bedford, J. D., Faulkner, D. R., & Lapusta, N. (2022). Fault rock heterogeneity can produce fault weakness and reduce fault stability. *Nature Communications*, *13*(1), 326. https://doi.org/10.1038/s41467-022-27998-2

Buijze, L., Guo, Y., Niemeijer, A. R., Ma, S., & Spiers, C. J. (2020). Nucleation of Stick-Slip Instability Within a Large-Scale Experimental Fault: Effects of Stress Heterogeneities Due to Loading and Gouge Layer Compaction. *Journal of Geophysical Research: Solid Earth*, *125*(8). https://doi.org/10.1029/2019JB018429

Buijze, L., Guo, Y., Niemeijer, A. R., Ma, S., & Spiers, C. J. (2021). Effects of heterogeneous gouge segments on the slip behavior of experimental faults at dm scale. *Earth and Planetary Science Letters*, *554*(December 2020). https://doi.org/10.1016/j.epsl.2020.116652

Cattania, C. (2019). Complex Earthquake Sequences On Simple Faults. *Geophysical Research Letters*, *46*(17–18), 10384–10393. https://doi.org/10.1029/2019GL083628

Cebry, S. B. L., & McLaskey, G. C. (2021). Seismic swarms produced by rapid fluid injection into a low permeability laboratory fault. *Earth and Planetary Science Letters*, *557*, 116726. https://doi.org/10.1016/j.epsl.2020.116726

Cebry, S. B. L., Ke, C. Y., Shreedharan, S., Marone, C., Kammer, D. S., & McLaskey, G. C. (2022). Creep fronts and complexity in laboratory earthquake sequences illuminate delayed earthquake triggering. *Nature Communications*, *13*(1), 1–9. https://doi.org/10.1038/s41467-022-34397-0

Cebry, S. B. L., Sorhaindo, K., & McLaskey, G. C. (2023). Laboratory Earthquake Rupture Interactions With a High Normal Stress Bump. *Journal of Geophysical Research: Solid Earth*, *128*(11), 1–24. https://doi.org/10.1029/2023JB027297

Chen, T., & Lapusta, N. (2009). Scaling of small repeating earthquakes explained by interaction of seismic and aseismic slip in a rate and state fault model. *Journal of Geophysical Research: Solid Earth*, *114*(1), 1–12. https://doi.org/10.1029/2008JB005749

Dieterich, J. H. (1979). Modeling of rock friction: 1. Experimental results and constitutive equations. *Journal of Geophysical Research*, *84*(B5), 2161. https://doi.org/10.1029/JB084iB05p02161

Dieterich, J. H. (1992). Earthquake nucleation on faults with rate-and state-dependent strength. *Tectonophysics*, *211*(1–4), 115–134. https://doi.org/10.1016/0040-1951(92)90055-B

Dieterich, J. H., & Kilgore, B. D. (1994). Direct observation of frictional contacts: New insights for state-dependent properties. *Pure and Applied Geophysics PAGEOPH*, *143*(1–3), 283–302. https://doi.org/10.1007/BF00874332

Giorgetti, C., Carpenter, B. M., & Collettini, C. (2015). Frictional behavior of talc-calcite mixtures. *Journal of Geophysical Research: Solid Earth*, *120*(9), 6614–6633. https://doi.org/10.1002/2015JB011970

Guérin-Marthe, S., Nielsen, S., Bird, R., Giani, S., & Di Toro, G. (2019). Earthquake Nucleation Size: Evidence of Loading Rate Dependence in Laboratory Faults. *Journal of Geophysical Research: Solid Earth*, *124*(1), 689–708. https://doi.org/10.1029/2018JB016803

Ito, Y., Obara, K., Shiomi, K., Sekine, S., & Hirose, H. (2007). Slow Earthquakes Coincident with Episodic Tremors and Slow Slip Events. *Science*, *315*(5811), 503–506. https://doi.org/10.1126/science.1134454

Kaneko, Y., & Lapusta, N. (2008). Variability of earthquake nucleation in continuum models of rate-and-state faults and implications for aftershock rates. *Journal of Geophysical Research: Solid Earth*, *113*(12), 1–25. https://doi.org/10.1029/2007JB005154

Kaneko, Yoshihiro, Nielsen, S. B., & Carpenter, B. M. (2016). The onset of laboratory earthquakes explained by nucleating rupture on a rate-and-state fault. *Journal of Geophysical Research: Solid Earth*, *121*(8), 6071–6091. https://doi.org/10.1002/2016JB013143

Lapusta, N., & Liu, Y. (2009). Three-dimensional boundary integral modeling of spontaneous earthquake sequences and aseismic slip. *Journal of Geophysical Research: Solid Earth*, *114*(9), 1–25. https://doi.org/10.1029/2008JB005934

Lapusta, N., & Rice, J. R. (2003). Nucleation and early seismic propagation of small and large events in a crustal earthquake model. *Journal of Geophysical Research: Solid Earth*, *108*(B4), 1–18. https://doi.org/10.1029/2001jb000793

Leeman, J. R., Saffer, D. M., Scuderi, M. M., & Marone, C. (2016). Laboratory observations of slow earthquakes and the spectrum of tectonic fault slip modes. *Nature Communications*, *7*(1), 11104. https://doi.org/10.1038/ncomms11104

Lu, X. (2009). Combined experimental and numerical study of spontaneous dynamic rupture on frictional interfaces. *California Institute of Technology*.

Lui, S. K. Y., & Lapusta, N. (2016). Repeating microearthquake sequences interact predominantly through postseismic slip. *Nature Communications*, *7*, 1–7. https://doi.org/10.1038/ncomms13020

Lui, S. K. Y., & Lapusta, N. (2018). Modeling High Stress Drops, Scaling, Interaction, and Irregularity of Repeating Earthquake Sequences Near Parkfield. *Journal of Geophysical Research: Solid Earth*, *123*(12), 10,854-10,879. https://doi.org/10.1029/2018JB016472

Luo, Y., & Ampuero, J.-P. (2018). Stability of faults with heterogeneous friction properties and effective normal stress. *Tectonophysics*, *733*(October 2017), 257–272. https://doi.org/10.1016/j.tecto.2017.11.006

Marone, C. (1998). Laboratory-derived friction laws and their application to seismic faulting. *Annual Review of Earth and Planetary Sciences*, *26*(1), 643–696. https://doi.org/10.1146/annurev.earth.26.1.643

Mclaskey, G. C., & Yamashita, F. (2017). Slow and fast ruptures on a laboratory fault controlled by loading characteristics. *Journal of Geophysical Research: Solid Earth*, *122*(5), 3719–3738. https://doi.org/10.1002/2016JB013681

McLaskey, G. C. (2019). Earthquake Initiation From Laboratory Observations and Implications for Foreshocks. *Journal of Geophysical Research: Solid Earth*, *124*(12), 12882–12904. https://doi.org/10.1029/2019JB018363

Mei, C., Barbot, S., & Wu, W. (2021). Period-Multiplying Cycles at the Transition Between Stick-Slip and Stable Sliding and Implications for the Parkfield Period-Doubling Tremors. *Geophysical Research Letters*, *48*(7), 1–13. https://doi.org/10.1029/2020GL091807

Mei, C., Barbot, S., Jia, Y., & Wu, W. (2022). Experimental evidence for multiple controls on fault stability and rupture dynamics. *Earth and Planetary Science Letters*, *577*, 117252. https://doi.org/10.1016/j.epsl.2021.117252

Michel, S., Avouac, J., Lapusta, N., & Jiang, J. (2017). Pulse-like partial ruptures and high-frequency radiation at creeping-locked transition during megathrust earthquakes. *Geophysical Research Letters*, *44*(16), 8345–8351. https://doi.org/10.1002/2017GL074725

Moore, D. E., & Rymer, M. J. (2007). Talc-bearing serpentinite and the creeping

section of the San Andreas fault. *Nature*, *448*(7155), 795–797. https://doi.org/10.1038/nature06064

Nakata, R., Ando, R., Hori, T., & Ide, S. (2011). Generation mechanism of slow earthquakes: Numerical analysis based on a dynamic model with brittle-ductile mixed fault heterogeneity. *Journal of Geophysical Research*, *116*(B8), B08308. https://doi.org/10.1029/2010JB008188

Obara, K., & Kato, A. (2016). Connecting slow earthquakes to huge earthquakes. *Science*, *353*(6296), 253–257. https://doi.org/10.1126/science.aaf1512

Obara, K., Hirose, H., Yamamizu, F., & Kasahara, K. (2004). Episodic slow slip events accompanied by non-volcanic tremors in southwest Japan subduction zone. *Geophysical Research Letters*, *31*(23), 1–4. https://doi.org/10.1029/2004GL020848

Rice, J. R., & Ruina, A. L. (1983). Stability of Steady Frictional Slipping. *Journal of Applied Mechanics*, *50*(2), 343–349. https://doi.org/10.1115/1.3167042

Rubin, A. M., & Ampuero, J.-P. (2005). Earthquake nucleation on (aging) rate and state faults. *Journal of Geophysical Research: Solid Earth*, *110*(B11), 1–24. https://doi.org/10.1029/2005JB003686

Ruina, A. (1983). Slip instability and state variable friction laws. *Journal of Geophysical Research: Solid Earth*, *88*(B12), 10359–10370. https://doi.org/10.1029/JB088iB12p10359

Sathiakumar, S., & Barbot, S. (2021). The stop-start control of seismicity by fault bends along the Main Himalayan Thrust. *Communications Earth & Environment*, *2*(1), 87. https://doi.org/10.1038/s43247-021-00153-3

Scholz, C. H. (1998). Earthquakes and friction laws. *Nature*, *391*(6662), 37–42. https://doi.org/10.1038/34097

Scuderi, M. M., Marone, C., Tinti, E., Di Stefano, G., & Collettini, C. (2016). Precursory changes in seismic velocity for the spectrum of earthquake failure modes. *Nature Geoscience*, *9*(9), 695–700. https://doi.org/10.1038/ngeo2775

Titus, S. J., DeMets, C., & Tikoff, B. (2006). Thirty-Five-Year Creep Rates for the Creeping Segment of the San Andreas Fault and the Effects of the 2004 Parkfield Earthquake: Constraints from Alignment Arrays, Continuous Global Positioning System, and Creepmeters. *Bulletin of the Seismological Society of America*, *96*(4B), S250–S268. https://doi.org/10.1785/0120050811

Veedu, D. M., & Barbot, S. (2016). The Parkfield tremors reveal slow and fast ruptures on the same asperity. *Nature*, *532*(7599), 361–365. https://doi.org/10.1038/nature17190

Veedu, D. M., Giorgetti, C., Scuderi, M., Barbot, S., Marone, C., & Collettini, C. (2020). Bifurcations at the Stability Transition of Earthquake Faulting. *Geophysical Research Letters*, *47*(19), 1–10. https://doi.org/10.1029/2020GL087985

Wallace, L. M., Webb, S. C., Ito, Y., Mochizuki, K., Hino, R., Henrys, S., et al. (2016). Slow slip near the trench at the Hikurangi subduction zone, New Zealand. *Science*, *352*(6286), 701–704. https://doi.org/10.1126/science.aaf2349

Wu, B. S., & McLaskey, G. C. (2019). Contained Laboratory Earthquakes Ranging From Slow to Fast. *Journal of Geophysical Research: Solid Earth*, *124*(10), 10270–10291. https://doi.org/10.1029/2019JB017865

Xu, S., Fukuyama, E., Yamashita, F., Mizoguchi, K., Takizawa, S., & Kawakata, H. (2018). Strain rate effect on fault slip and rupture evolution: Insight from meter-scale rock friction experiments. *Tectonophysics*, *733*(November 2017), 209–231. https://doi.org/10.1016/j.tecto.2017.11.039

Yamashita, F., Fukuyama, E., & Xu, S. (2022). Foreshock Activity Promoted by Locally Elevated Loading Rate on a 4-m-Long Laboratory Fault. *Journal of Geophysical Research: Solid Earth*, *127*(3). https://doi.org/10.1029/2021JB023336

CHAPTER 4

Fault healing and asperity partitioning on a frictionally heterogeneous laboratory fault

This chapter is drawn from the Preprinted paper: *Song, J.Y., Cattania, C. and McLaskey, G.C., 2025. Fault healing and asperity partitioning on a frictionally heterogeneous laboratory fault. Journal of Geophysical Research: Solid Earth (Accepted for publication).*

4.1. Abstract

Natural faults likely include both Velocity-Weakening (VW) and Velocity-Strengthening (VS) areas. We developed a laboratory method to replicate this frictional heterogeneity using a 760 mm long Polymethyl methacrylate (PMMA) block with eleven VW patches (bare PMMA) separated by VS barriers (Teflon tape). We compared the behavior of this Multiple Patches (MP) arrangement to those from One single VW Patch (OP) with the same total VW fault area. Seismic events that occurred in clusters with foreshocks and aftershocks were observed only in the MP tests, and total slip, maximum slip rate, seismic moment, and recurrence time of the largest event (termed the mainshock) in a slip cycle, were an order of magnitude smaller in the MP tests compared to the OP tests. Slower loading rates, corresponding to longer recurrence time, produced larger mainshock magnitudes in the OP tests, as expected due to fault healing. In contrast, the mainshock magnitude in the MP tests decreased with increasing recurrence time due to the increased effectiveness of VS barriers at

slower loading rates. In some MP tests, foreshock-like events migrated at ~0.7 m/s, followed by faster reverse migration at ~7 m/s, resembling Rapid Tremor Reversal (RTR) in subduction zones. We used a numerical simulation to quantitatively reproduce the RTR-like behavior, help explain its mechanics, and constrain the friction properties of the laboratory system. Overall, our findings highlight how identical structural features on heterogeneous faults can behave differently under different loading conditions due to the velocity dependence of VS barriers.

4.2. Introduction

Earthquakes are significantly influenced by structural features of fault systems, such as the thickness and mineralogy of pulverized rock known as gouge that is present in the fault core. Fault sections can be categorized into velocity-strengthening (VS) and velocity-weakening (VW) types and these characteristics play pivotal roles in fault mechanics and the generation of seismic activity (Dieterich, 1992; Rice & Ruina, 1983). Laboratory experiments have shown that VW gouges (e.g., Quartz rich minerals) are closely associated with the initiation of unstable stick-slip events, which are essential for the development of seismic earthquakes (Carpenter et al., 2016; Collettini et al., 2011; Ikari et al., 2011). In contrast, VS gouges (e.g., Phyllosilicates or unconsolidated layers) are associated with stabilizing fault behavior, which mitigates dynamic slip and promotes stable sliding (Carpenter et al., 2016; Collettini et al., 2011; Ikari et al., 2011). These types of gouges on the fault have been documented across various geological settings (Carpenter et al., 2016; Tesei et al., 2014).

Previous modeling studies have explored slip behaviors by employing a model that

consists of a single VW patch surrounded by VS regions (Barbot, 2019; Cattania, 2019; Cattania & Segall, 2021; Chen et al., 2010; Chen & Lapusta, 2009; Kaneko et al., 2008; Kaneko & Lapusta, 2010; Marone et al., 1991). This simplified framework has proven to be a valuable tool for investigating diverse phenomena, such as varying slip behaviors as a function of source dimension relative to the nucleation length (Barbot, 2019; Cattania, 2019), cycles of repeating earthquakes (Cattania & Segall, 2021; Chen et al., 2010; Chen & Lapusta, 2009), dynamic rupture processes (Kaneko et al., 2008; Kaneko & Lapusta, 2010), and afterslip (Marone et al., 1991). The behavior of two VW asperities separated and surrounded by a VS matrix has been investigated, further advancing our understanding of fault interactions (Kaneko et al., 2010; Kato, 2004; Kato & Yoshida, 2011; Lui & Lapusta, 2016, 2018; Wei & Shi, 2021).

The geometrical complexities of natural faults significantly surpass the simplified framework often used to represent them. For instance, subduction zones are not uniformly distributed across one or two VW patches; rather, they are thought of as a diverse array of VW asperities (Konca et al., 2008; Yamanaka & Kikuchi, 2004). To better understand the dynamic behaviors of earthquakes, recent models have increased the complexity of fault friction by varying the frictional properties across multiple patches. These investigations included the initiation of rupture and the complexity of foreshock activities prior to the mainshocks (Cattania & Segall, 2021; Dublanchet, 2018; Ito & Kaneko, 2023), characteristics of slow earthquakes along subduction zones (Nakata et al., 2011), and patterns of microseismicity in repeating earthquakes (Dublanchet et al., 2013). These studies aimed to clarify how seismic activity might

occur on frictionally heterogeneous faults, thereby advancing our understanding of earthquake mechanics.

Experimental studies on slip behaviors, spanning scales from centimeters to meters, have generally been conducted on frictionally homogeneous faults. In small-scale experiments (smaller than 1 m in length), researchers have explored slip behaviors by varying loading rates (Anthony & Marone, 2005; Guérin-Marthe et al., 2019; Leeman et al., 2018; Marone et al., 1990; Zhou et al., 2021), normal stress (Leeman et al., 2016, 2018; Marone et al., 1990; McLaskey et al., 2012; Mclaskey & Yamashita, 2017; Mei et al., 2022; Zhou et al., 2021), and fault roughness (Anthony & Marone, 2005; Dresen et al., 2020; Fryer et al., 2022; Goebel et al., 2017, 2023; Marone et al., 1990; Zhou et al., 2021), enabling them to explore transitions from slow to dynamic slip behaviors. However, the limited sample size and homogeneous fault conditions make it challenging to observe contained ruptures that do not propagate through the entire laboratory fault. Large-scale experiments (larger than 1 meter in length) have focused on the initiation of earthquakes, taking advantage of the scale (McLaskey, 2019; Yamashita et al., 2021). However, because these large-scale experiments have been conducted under frictionally homogeneous fault conditions, they only sporadically produced contained ruptures (McLaskey, 2019; Wu & McLaskey, 2019), making it difficult to study more realistic rupture behaviors within a repetitive stick-slip cycle. While foreshock activity has been documented in many laboratory experiments, it is usually associated with rough faults made from natural fractures (e.g., Dresen et al., 2020; Goebel et al., 2017; Scholz, 1968), wear processes on saw cut faults (e.g., McLaskey & Lockner, 2014; Passelègue et al., 2017; Yamashita et al.,

2021), or comminution of gouge layers (e.g., Bolton et al., 2023). Generating repeating seismic cycles that consistently include foreshocks and aftershocks whose mechanisms are distinct from grain-scale wear processes has proven challenging.

Instead of frictionally homogeneous fault conditions, a frictionally heterogeneous fault (e.g., a VW patch surrounded by the VS patches) has been recently achieved via different gouge mineralogy (Bedford et al., 2022; Buijze et al., 2021), different granular materials (Corbi et al., 2024), or Teflon (Song & McLaskey, 2024). Although the VS patches on the fault ends do not always ensure a completely contained rupture, they do slow down rupture and help create fault conditions that are more similar to natural faults (Song & McLaskey, 2024). Nevertheless, a fault with a single VW patch is typically unable to generate the complexity of natural seismic activity.

In this study, we focused on creating frictionally heterogeneous samples to investigate the interaction of multiple VW patches separated by VS patches. We adapted the method described by Song & McLaskey (2024) to create VS and VW patches, using bare PMMA for VW patches and Teflon tape for VS patches. Along the 760 mm long PMMA laboratory fault, we created eleven VW patches by separating VS patches (i.e., multiple patches, MP), as shown in Figure 4.1. We compared that configuration to a single VW patch surrounded by VS patches (i.e., one patch, OP), ensuring that the total VW area remained equal to that of the MP tests, in order to directly compare the effect of the VS barriers within the VW patch. The MP tests exhibited a noticeable mainshock accompanied by multiple foreshocks and aftershocks, whereas the OP tests generally exhibited one event in each slip cycle. We found that fault behavior such as recurrence time, total slip, and maximum slip rate in the OP tests were roughly an

order of magnitude larger than those in the MP tests, indicating that the VS barriers significantly reduced the slip of the VW patches. When exploring the effect of the loading rate (e.g., 4.5 μm/s, 1.4 μm/s, and 0.45 μm/s), longer recurrence time, resulting from slower loading rates, led to larger magnitude of the mainshock in the OP tests, consistent with the well-known fault healing effect (Anthony & Marone, 2005; Karner & Marone, 2000; Leeman et al., 2018). In contrast, longer recurrence time led to smaller magnitude of the mainshock in the MP tests. In some MP tests, we observed sequences of foreshocks whose hypocenters migrated along the sample in a main front that propagated at ~0.7 m/s. We also observed fronts that propagated backwards from the main front propagation in a manner that resembles Rapid Tremor Reversals (RTRs) observed in subduction zones (Houston et al., 2011; Thomas et al., 2013; Yamashita et al., 2015). We used a numerical model that quantitatively reproduced many aspects of the RTRs to better understand the mechanics of this behavior and to better constrain the friction properties of the laboratory system.

4.3. Materials and Methods

4.3.1. Experimental setup

We positioned two PMMA blocks within a biaxial machine (Figure 4.1a), with a detailed description provided in previous studies (Cebry et al., 2023; Cebry & McLaskey, 2021; Mclaskey & Yamashita, 2017; Song & McLaskey, 2024). The dimensions of the moving block were 760 mm by 203 mm by 38 mm and the dimensions of the stationary block were 790 mm by 152 mm by 38 mm, in the x, y, and z directions, respectively. Normal stress was applied to the fault using four

hydraulic cylinders, while shear stress was applied by a cylinder located at forcing end or North (N), with its opposite leading end or South (S). To minimize the effect of friction from surfaces other than the fault surfaces, we placed Teflon between one steel-to-steel interface (Low Friction Interface, LFI) and all of the PMMA-to-steel interfaces.

4.3.2. Fault conditions

The fault surfaces of both PMMA blocks were first machined flat via fly cutting and then roughened with 80 grit abrasive before the test. We covered part of the fault with Teflon tape to create velocity-strengthening (VS) patches, while the bare surface of the PMMA served as velocity-weakening (VW) patches. To achieve this, we trimmed the specified length of Teflon tape (Taegatech, PTFE tape, 0.813 mm thick and 50.8 mm wide) to cover the fault surface on both PMMA blocks. The Teflon was secured to the top and bottom of the block using transparent tape. Then, we placed plastic wrap between the Teflon-attached region to prevent the Teflon surfaces from adhering together. A more detailed description for Teflon surface treatment is described in Song & McLaskey (2024).

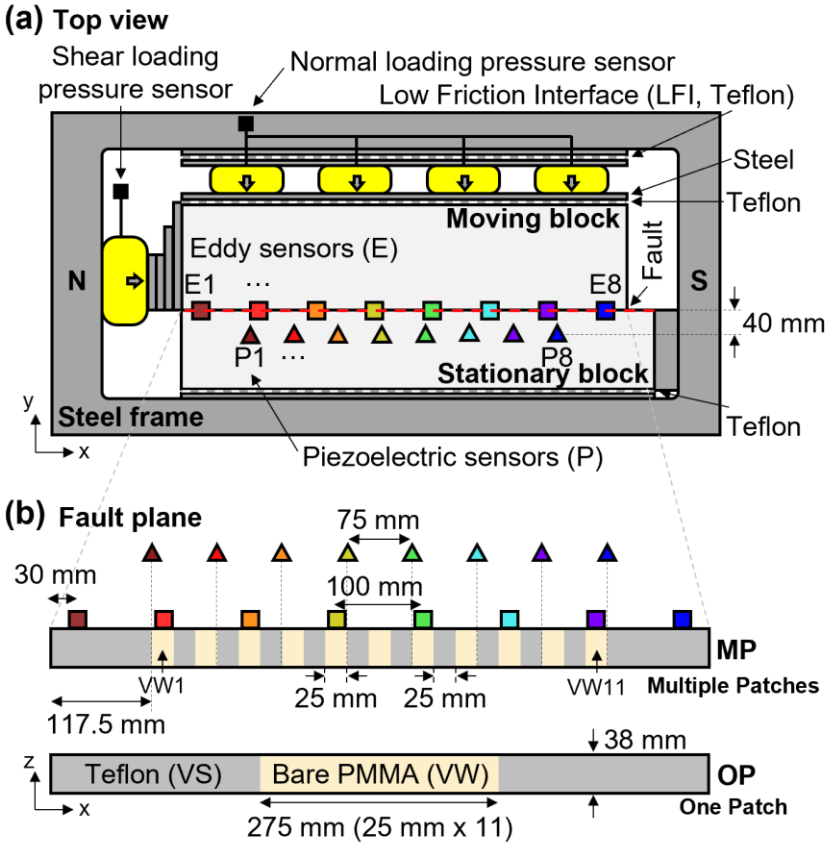

Figure 4.1. Experimental setup and fault conditions. (a) Top view of the biaxial experimental setup. The sensors (E1 to E8 and P1 to P8) were attached to the top surface of the blocks. (b) Fault conditions with respect to VW patch size (e.g., MP and OP). Note that the PMMA patches in the MP test were designated from VW1 to VW11.

The friction properties of Teflon were determined through a double-direct shear test (Figure 4.A1a). The sample-average friction coefficient, the ratio between shear and normal stresses, varied systematically with normal stress, ranging from 0.016 to 0.05 and the (a - b) values ranged from 0.001 to 0.002 (Figure 4.A1c). The friction coefficient of the LFI was ~0.04, similar to that between steel and Teflon observed in a previous study (Dieterich & Kilgore, 1994).

We performed two distinct sets of experiments with different arrangements of Teflon patches on the fault (Figure 4.1b). The first condition, termed Multiple Patches (MP),

consisted of eleven VW patches, each 25 mm in length, interspersed with VS patches. The VW patches were labeled from VW1 to VW11. The second condition, referred to as One Patch (OP), included a single 275 mm VW patch, surrounded by VS patches, having the same total VW patch area as the MP condition.

4.3.3. Measurement sensors

The sample-average shear stress (τ_{mech}) and normal stress (σ_{mech}) were determined using pressure sensors connected to the yellow hydraulic cylinders (Figure 4.1a). Fault slip measurements were carried out using eight Eddy current sensors, attached with hot glue (Stanley, DualMelt glue stick). The first sensor, E1, was positioned 30 mm from the forcing end, with subsequent sensors spaced 100 mm apart in the x-direction (Figure 4.1b). The Eddy current sensor included a probe (attached ~10 mm from the fault trace on the top surface of the stationary block) and measured the distance to the steel target (attached ~10 mm from the fault trace on the top surface of the moving block) with a resolution of ~0.15 μm and a sampling rate of 20 kHz. To measure and quantify laboratory earthquakes (labquakes), eight Piezoelectric sensors (Panametrics, V103) were attached to the top of the stationary block using hot glue. Those sensors measure ground motion in the z-direction and they were positioned 40 mm away from the fault in the y-direction, starting at 117.5 mm from the forcing end with 75 mm intervals between them in the x-direction (P1 to P8) (Figure 4.1b). The Piezoelectric sensors with odd numbers measured a range from -50 V to 50 V for the large magnitude events, whereas the sensors with even numbers (e.g., P2, P4, P6, and P8) measured a range from -1 V to 1 V for the small magnitude events. The data from P1

to P8 were continuously recorded at a rate of 20 kHz and also captured data in triggered mode at 2 MHz for 50 ms blocks. The triggered mode was activated when it reached a certain threshold, which was slightly above the noise level. Only four piezoelectric sensors (-50 V to 50 V) were attached in the OP test at the same locations of the odd numbered sensors (P1, P3, P5, and P7) in the MP tests. We presented the ground motion response in voltage (e.g., Figure 4.3) instead of physical units because the connection to physical units changes as a function of frequency (Wu & McLaskey, 2018).

4.3.4. Experimental procedure

The assembly was subjected to $\sigma_{mech} = 15 \pm 1$ MPa and sheared 2 mm at 4.5 μm/s to adhere the Teflon to the PMMA and allow for any run-in phase (see Song & McLaskey, 2024). Then we recorded three runs at different loading rates: 0.45 μm/s, 1.4 μm/s, and 4.5 μm/s, in that order. The loading rate was determined by dividing the total recorded slip by the corresponding time interval. This procedure was applied to both the MP and OP tests. In each run, we analyzed five consecutive slip events for the OP tests and ten consecutive slip events for the MP tests, as described in Section 4.4. Initially, the Teflon-covered patches on each side of the fault were offset by 2 mm so that they would be perfectly aligned after the 2 mm run-in period. With continued fault slip, there can be misalignment of Teflon-covered patches on each side of the fault. We recorded only 5 to 10 slip events in order to minimize the sample offset, so that this misalignment of Teflon patches accounted for less than ~10 % of the original length of VW patches.

4.3.5. Calculation of magnitude

The seismic moment of labquakes was calculated from the piezoelectric sensor data and absolutely calibrated using a ball drop technique as a reference source or empirical Green's function (EGF) (Cebry & McLaskey, 2024; McLaskey et al., 2015; Song & McLaskey, 2024; Wu & McLaskey, 2019). In this technique, the absolute source spectrum of the labquakes was obtained by comparing their ground motions to those generated by a ball impact, a well-characterized seismic source of known amplitude and frequency content.

For the ball drop calibration, a steel ball with 6.35 mm diameter was dropped from 130 mm height onto the fault surface of the moving block when normal stress was not applied to the sample. We chose this configuration, rather than dropping the ball onto the top surface of the sample (where the AE sensors were attached) under realistic normal stress conditions, because we found that ball drops that impacted the same surface as AE sensors generated strong Rayleigh waves that biased our estimates 3 to 8 times too high, consistent with the findings of McLaskey et al. (2015). Similar Rayleigh waves would not be produced by labquakes. We also found that normal stress conditions had minimal effects on ball drop recordings for these PMMA samples. The calculated change in momentum, ΔP (= $m \cdot \Delta v$), was 3.32E-3 Ns, where the mass of the steel ball (m) was 1.05E-3 kg and the change in velocity (Δv) was 3.18 m/s. The Δv was estimated using initial ball drop height as initial impact velocity was $\sqrt{2 \cdot g \cdot h}$ and the rebound velocity was $g \cdot \Delta t/2$ where h is dropping height of the ball, g is gravitational acceleration, and Δt is the time difference between the first and second impacts of the ball. The seismic moment of the ball drop, M_{0_BD}, is equal to $C_{FM} \cdot \Delta P$,

where C_{FM} is equal to the twice the wave speed in the material due to the free surface effect (McLaskey et al., 2015). For PMMA, the C_{FM} was ~4200 m/s, so the calculated M_0 for the ball drop was 13.93 Nm. The corner frequency (f_0) of the ball impact in this study was 16 kHz as the contact time (t_c) was 63 μs (methods described in Wu & McLaskey, 2018). The low-frequency range (4 - 9 kHz) was chosen as a reference because it had a good Signal-to-Noise Ratio (SNR) and was below the f_0 of the ball impact. Therefore, using the average value in the frequency domain (Ω_0), the calculated seismic moment (M_0_seis) of a seismic event was M_0_BD·(Ω_0_seis / Ω_0_BD) = 13.93 Nm·(1.01E-1/1.31E-3) = 1074 Nm (Figure 4.S1). The corresponding magnitude (**M**) was -4.05 which was calculated using the equation below (Hanks & Kanamori, 1979):

$$\mathbf{M} = 2/3 \cdot \log(M_{0\_Seis}) - 6.067 \quad (4.1)$$

4.4. Results

4.4.1. Effect of partitioning the VW patches by VS patches

We investigated the effects of partitioning VS patches between VW patches by comparing the OP and MP tests. Figure 4.2 shows the sample-average friction coefficient (τ_{mech} / σ_{mech}) and slip from E1 to E8 for the OP and MP tests at 0.45 μm/s loading rate. The τ_{mech} / σ_{mech} repeatedly reaches a peak and then drops, with corresponding increases in slip indicating stick-slip events (Figure 4.2a). The recurrence time (T_r) is the interval between each slip event. Despite having the same total areas of VW and VS patches, the OP fault exhibits ~40 % greater frictional strength, with sample-average stress changes ($\Delta\tau_{mech}$) that are ~25 times larger and slip

that is ~15 times larger compared to the MP fault (see also Figure 4.3).

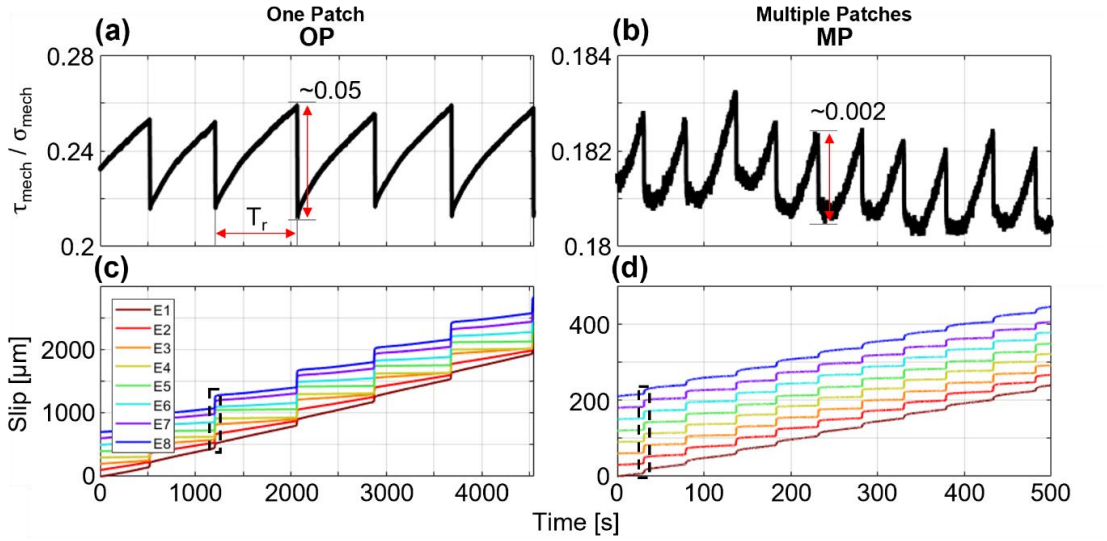

Figure 4.2. Sample-average friction coefficient (τ_{mech} / σ_{mech}) of (a) the OP and (b) MP tests and the corresponding slip of (c) the OP and (d) MP tests at 0.45 μm/s loading rate. The σ_{mech} remained at a consistent level of 15 ± 1 MPa. Note that the black dotted boxes are shown in detail in Figure 4.3.

We also compared a fault coupling ratio, defined as the ratio of dynamic slip (slip rates exceeding 10 mm/s) to the total slip within one recurrence interval. The threshold slip rate above which slip events become audible and radiate significant seismic energy ranges from 1 - 10 mm/s (Mclaskey & Yamashita, 2017; Scuderi et al., 2016; Song & McLaskey, 2024; Wu & McLaskey, 2019) and we selected 10 mm/s to be consistent with previous experiments of similar scale (Song & McLaskey, 2024). We calculated the fault coupling ratio by averaging the individual ratios obtained from the slip sensors attached to their corresponding VW patches: E4 and E5 for the OP test and E2 to E7 for the MP test. The fault coupling ratio close to 1 indicates that most of the faults remain locked for most of the seismic cycle and slip only during seismic

events. In contrast, a ratio close to 0 indicates that most slip is aseismic, occurring as creep without slipping fast and generating seismic events. We averaged the fault coupling ratio over multiple slip cycles and found fault coupling ratios of 0.69 for the OP test and 0.21 for the MP test. The MP test shows both a lower total slip and a reduced fault coupling ratio relative to the OP test, suggesting that aseismic creep is prevalent in the MP test. Overall, the fault in the MP test is weaker and has low coupling ratio, low $\Delta\tau_{mech}$, and small slip within a slip cycle.

We analyzed representative slip events from both the OP and MP tests to investigate detailed slip behaviors, focusing on the regions highlighted by the black dotted boxes in Figures 4.2c and 4.2d. Figure 4.3 shows the temporal evolution of slip distribution along the fault, capturing all stick-slip events within a slip cycle. The insets in Figures 4.3a and 4.3b show the ground motions recorded with sensor P3. Figures 4.3c and 4.3d show the same slip data as a function of fault distance, with lines plotted at 0.1 ms time interval, and the color of the line changes from dark to light purple over a 10 ms time interval. This purple diagram allows for a rough estimation of slip speed: wider gaps between the lines indicate fast slip, while closely spaced lines that show the light and dark purple color banding indicate slow slip.

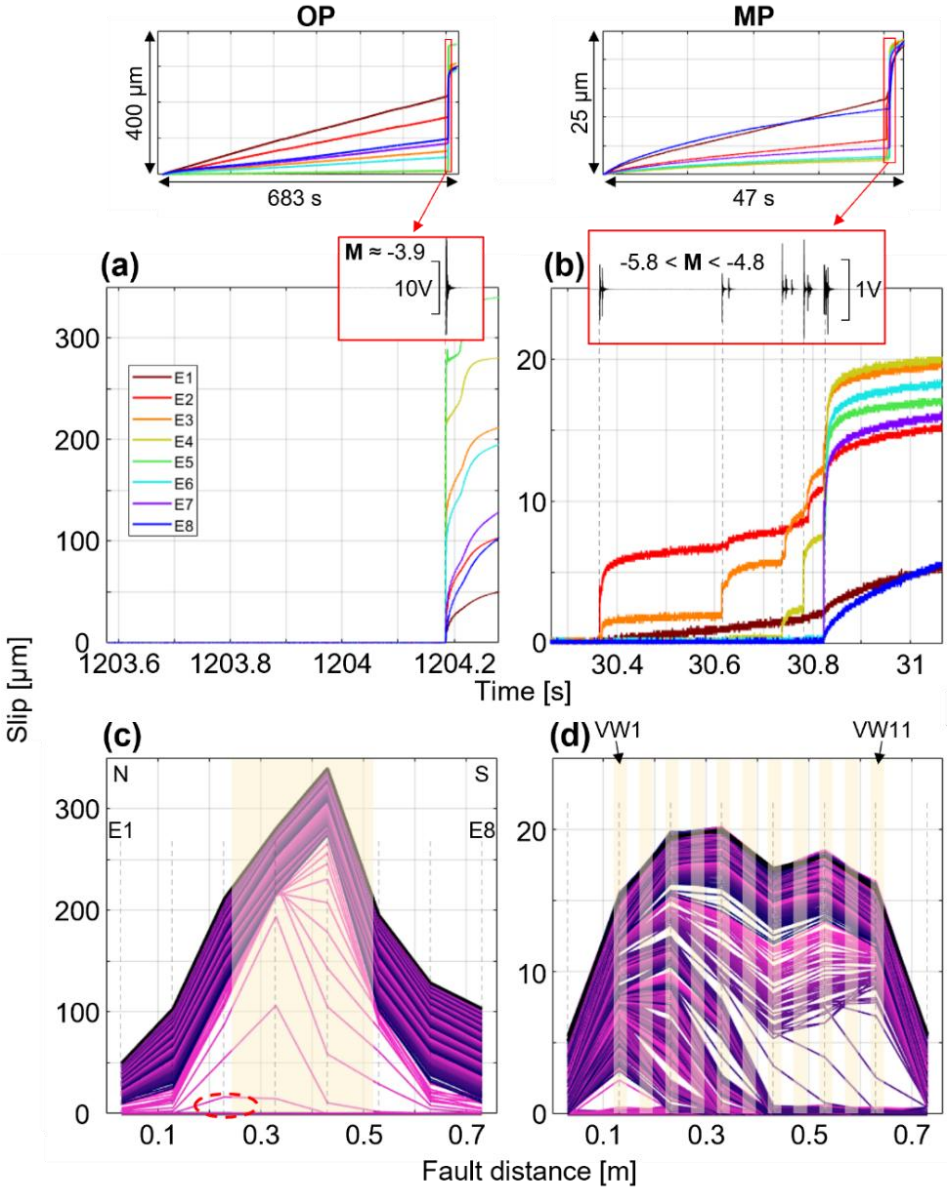

Figure 4.3. Representative stick-slip events at 0.45 µm/s loading rate (Black dotted boxes in Figures 2c and 2d). Temporal slip for (a) the OP and (b) MP tests, along with the corresponding slip with fault distance for (c) the OP and (d) MP tests. The top inset shows the ground response from P3. Note that the yellow shaded area indicates the location of the VW patches.

The OP test generally produces only one slip event per slip cycle, with the maximum amplitude of ground motion reaching ~10 V (Figure 4.3a). The slip event starts to nucleate at the boundary between the VW patch and VS region (E3, red dotted circle)

and propagates to the leading end (Figure 4.3c). The MP test produces multiple ruptures within a slip cycle, generating small amplitude ground motions (~1 V) (Figure 4.3b). The calculated magnitude (**M)** ranges from -5.8 to -4.8, which is considerably smaller than the **M** (-3.9) observed in the OP tests (see Section 4.3.5 for the calculation of magnitude). The sequence of ruptures in the MP test started near the forcing end (VW1) and propagated toward the leading end (VW11), similar to general direction of rupture in the OP test (Figure 4.3d). Individual seismic events in the sequence rupture either a single VW patch or multiple VW patches simultaneously. It is difficult to distinguish between these cases since the spacing of Eddy sensors is larger than the spacing between the VW patches. The largest event in the sequence ruptures at least six VW patches simultaneously, including the rerupture of some VW patches that had already slipped individually a few ms earlier.

4.4.2. Magnitude of mainshock with loading rates

In this Section, we examined the mechanical properties of the OP and MP tests across multiple slip cycles, with a particular focus on recurrence time and magnitude. The MP tests exhibited multiple slip events per slip cycle, so we defined the mainshock as the event with the largest magnitude in each cycle; foreshocks as the events occurring within 1 s before the mainshock and aftershocks as the events occurring within 1 s after it. We classified all detected events as either foreshocks or aftershocks because they were clustered around the mainshock, and no events occurred outside of this time window. In contrast, the OP tests typically showed a single stick-slip event, which was considered as the mainshock. We occasionally observed a single foreshock during the

OP test, but only under 4.5 μm/s loading rate and for cases with small peak τ_{mech} / σ_{mech}; however, they did not significantly affect the magnitude (see Figure 4.S2).

Figure 4.4 illustrates the relationship between mainshock magnitude and recurrence time for each slip cycle in the OP and MP tests. For the OP tests, the reduction in loading rate caused longer T_r, resulting in higher **M** of the mainshock. This effect is attributed to the fault healing mechanism (see Section 4.5.2), which strengthens the fault over time under steady loading, requiring more shear stress to initiate the rupture (Marone & Saffer, 2015; Marone, 1998; McLaskey et al., 2012). In contrast, in the MP tests, the reduction in loading rate caused a notable decrease in **M**. This contradicted the expectation based on fault healing and discussed in Section 4.5.3. The mechanical properties of slip events generated at different loading rates are summarized in Table 4.1.

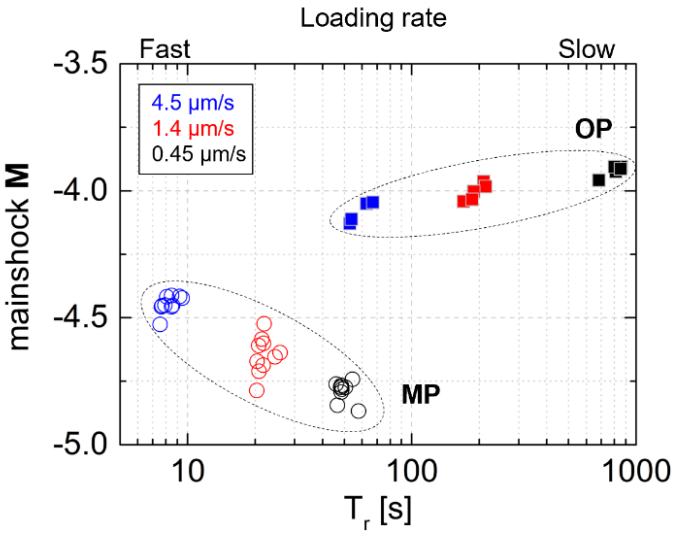

Figure 4.4. Relationship between mainshock magnitude (M) and recurrence time (T_r) across different loading rates. Solid squares present the OP tests, while hollow circles present the MP tests.

Table 4.1. Mechanical properties of the OP and MP tests with different loading rates. Note that these values are averages of all slip events.

Fault condition	Loading rate [μm/s]	σ_{mech} [MPa]	τ_{mech_peak} [MPa]	T_r [s]	Total slip [μm]	Max slip rate [mm/s]	Mainshock **M**
OP	4.5	15.6	3.7	59	230	445	-4.08
	1.4	15.7	3.8	193	265	678	-4.01
	0.45	15.5	4.0	802	360	1092	-3.92
MP	4.5	15.7	3.1	8	33	89	-4.44
	1.4	15.5	2.9	22	31	78	-4.59
	0.45	14.3	2.6	49	23	45	-4.80

4.4.3. Timing and magnitude of foreshocks and aftershocks depend on loading rate

In this Section, we explored the trends of the foreshocks, mainshock, and aftershocks in the MP tests with respect to the loading rate. Figure 4.5 shows the time interval and magnitude of the foreshocks and aftershocks under different loading rates in the MP tests. The foreshock interval is defined as the interval between the first foreshock and the mainshock, while the interval of the aftershocks is defined as the interval between the mainshock and the final aftershock within a slip cycle (Figure 4.5a). The interval of the foreshocks increases to ~500 ms as the loading rate decreases. However, the trend with the interval of the aftershocks is less clear, as it ranges from ~1 ms to ~20 ms, regardless of the loading rates. The average interval of the foreshocks and aftershocks is summarized in Table 4.2. The **M** of the foreshocks decreases with a reduction in loading rate, consistent with previous laboratory findings (Bolton et al., 2021) and the mainshocks exhibit a similar trend (Figure 4.5b). In addition to variations in **M**, significant changes in the number of foreshocks were observed with different loading rates; more foreshocks occur at slower loading rates (Table 4.2).

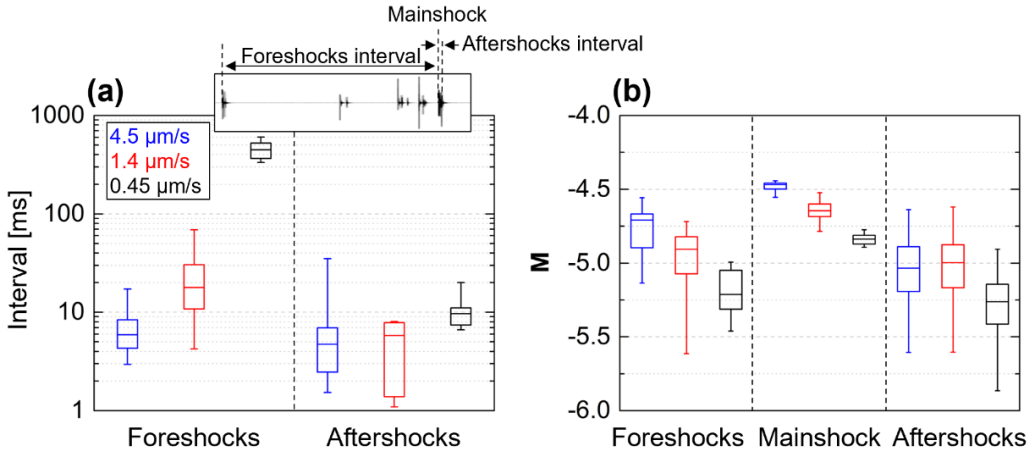

Figure 4.5. (a) Time interval of the foreshocks and aftershocks in a slip cycle and (b) magnitude of the ruptures with different loading rates. The interval of the foreshocks was defined as the time between the initial rupture of the foreshocks and the mainshock, while the interval of the aftershocks was defined as the time between the mainshock and the final rupture of the aftershocks within a slip cycle. Note that the example inset is from Figure 4.3b.

Table 4.2. Characteristics of the foreshocks and aftershocks in the MP tests. Note that these values are averages of all slip events.

Loading rate [μm/s]	Foreshocks			Aftershocks		
	Number	**M**	Interval [ms]	Number	**M**	Interval [ms]
4.5	2.3	-4.77	7	4.8	-5.04	8
1.4	6.2	-4.96	22	4.5	-5.03	5
0.45	11.1	-5.19	457	10.1	-5.30	10

4.4.4. Locations of foreshocks show a slow main front propagation and faster back propagation

We closely explored the slip behavior at 0.45 μm/s loading rate in the MP tests, revealing a distinct directionality of the rupture (detailed mechanisms in Section 4.5.4). Figure 4.6 shows the magnitude and location of the foreshocks, mainshock, and aftershocks, for the slip event shown in Figure 4.3b at ~30 s. We used this as a representative example of the spatiotemporal patterns of foreshocks and aftershocks.

The time of the mainshock serves as the reference time. The background shading indicates the slip rate measured with the eddy current slip sensors. The slip rate was calculated by averaging over specific time windows, such as 10 ms for Figure 4.6a and 0.2 ms for Figure 4.6b, to maintain consistent slip rate resolution across the plots. The hypocenter of the earthquakes and triggered time was obtained from the Piezoelectric sensors (details in Figure 4.S3). This method identifies which VW patch the labquake most likely emanated from, but not the detailed position within the patch. Therefore, we present the seismicity at the center of each VW patch rather than specifying precise locations within the patch. The first foreshock occurs at the forcing end (VW1) and a sequence of events, indicating the main front propagation, migrate across the sample. However, as the sequence of events migrate forward, some events also migrate backward (i.e., back propagation), diminishing in magnitude as they migrate away from the main front. The mainshock initiates at VW6 and ruptures dynamically through multiple VW patches with a fast slip rate (black color) compared to other events. Aftershocks mainly occur in this dynamically ruptured area (VW6 to VW11) over ~8 ms. As the loading rate increases (e.g., 1.4 μm/s and 4.5 μm/s), the main front propagation becomes more dominant, reducing the likelihood of back propagation (Figure 4.S4). At 1.4 μm/s loading rate, back propagation is still observed, but it is less pronounced compared to that at 0.45 μm/s loading rate. At 0.45 μm/s loading rate, while all foreshocks do not exactly replicate those shown in Figure 4.6a over ten slip cycles, they exhibit similar patterns of 2 or 3 back propagations within each slip cycle. We will discuss the characteristics of back propagation, including its magnitude and propagation velocity in Section 4.5.4.

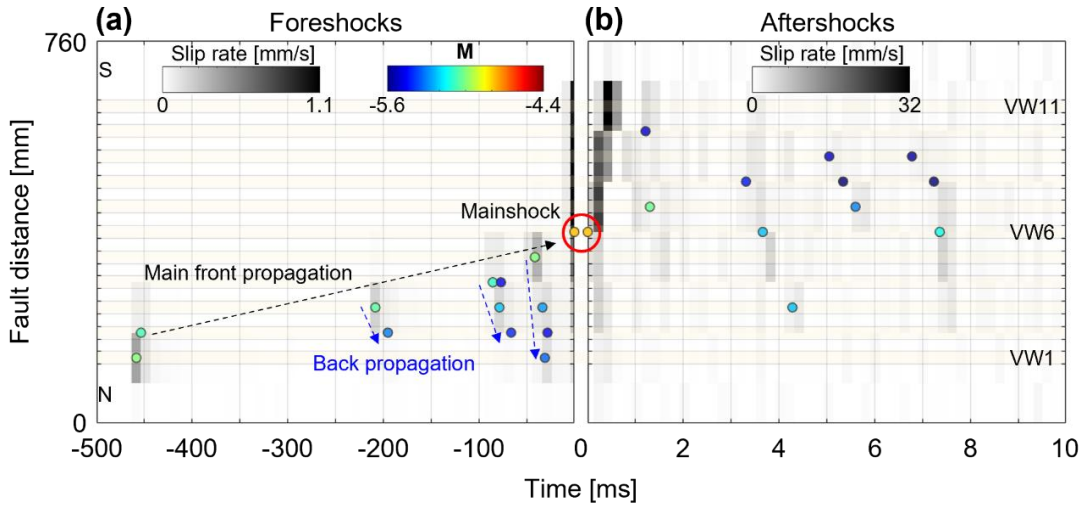

Figure 4.6. Location and magnitude of events in the MP test at 0.45 μm/s loading rate, showing (a) foreshocks and (b) aftershocks. The background color is from the slip rate, averaging over different time windows (10 ms for Figure 4.6a and 0.2 ms for Figure 4.6b). The location of the event is from the first arrival time of the Piezoelectric sensors (see details in Figure 4.S3). Note that the mainshock (red circle) establishes the reference point for the timeline. The yellow shaded area indicates the location of the VW patch.

4.5. Discussion

In this study, we introduced VS patches between the VW patches (e.g., MP test) to create heterogeneous fault friction and compared the slip behavior to a single VW patch (e.g., OP test), maintaining the same total VW area. This heterogeneous distribution of fault friction is consistent with previous numerical simulations (Dublanchet, 2018; Ito & Kaneko, 2023) that aimed to understand dynamic slip behaviors that were not observed with a single VW patch. In the following sections, we discuss how partitioning a VW patch with VS patches affected the general behavior such as total slip, magnitude, and recurrence time (Section 4.5.1), verification of the fault healing rate from OP tests (Section 4.5.2), barrier effectiveness of the VS patch at different loading rates in the MP tests (Section 4.5.3),

characteristics of the main front and back propagations (Section 4.5.4), and implications for the aftershocks that we observed (Section 4.5.5).

4.5.1. Effect of partitioning a VW patch by VS patches

The mechanical properties such as recurrence time, total slip, max slip rate, and magnitude of the OP tests were 5 to 25 times higher than those of the MP tests under the same loading rate (Table 4.1). This significant difference was attributed to the partitioning of a VW patch by VS barriers, which impeded dynamic rupture. The VS barriers led to the formation of foreshocks and aftershocks in the MP tests, while only foreshocks were occasionally observed in the OP tests (Figure 4.S2). The fault coupling ratio of the OP tests was three times higher than that of the MP tests (Section 4.4.1), suggesting that a single VW patch became more locked during interseismic period, while VW sections interspersed with VS barriers creeped more interseismically, reduced overall slip, slip rate, and magnitude of seismic events, and made it less prone to dynamic slip. There are somewhat different end-boundary conditions between the MP tests (117.5 mm-long VS sections) and the OP tests (242.5 mm-long VS sections) (Figure 4.1b). However, we believe their effect on slip behavior to be minor, compared to the partitioning by VS barriers.

Previous numerical studies have shown that interseismic creep is more prevalent on small VW patches than on larger ones (Cattania & Segall, 2019; Chen & Lapusta, 2009), and it can be understood as follows. As stress accumulates at the edges of each VW patch, the resulting creep front propagates into the VW patch and grows to the nucleation dimension (L_n) before instability. At the end of the seismic cycle, the total

length of creeping regions within VW patches is equal to ~$2N \cdot L_n$, with N as the number of VW patches. If we assume that creep takes place at a speed similar to the loading rate, the instantaneous coupling ratio across all VW regions is as follows:

$$\text{Coupling ratio} = (L_{tot} - 2N \cdot L_n) / L_{tot} = 1 - (2L_n / L_{VW}) \quad (4.2)$$

where $L_{tot} = N \cdot L_{VW}$ is the total VW length and L_{VW} is the size of each VW patch. Given that L_n = 8.75 mm for PMMA (Song & McLaskey, 2024), the coupling ratios are calculated to be 0.94 for the OP test and 0.3 for the MP test, which broadly matches the experimental trends (Section 4.4.1). This shows that the coupling ratio decreases with the total number of VW patches, consistent with our observations. Although approximate, this simple argument highlights the importance of the parameter L_{VW} / L_n, which was previously identified as a good metric to estimate the behavior of a single VW patch surrounded by VS patches (Barbot, 2019; Cattania, 2019; Song & McLaskey, 2024). Different expressions for L_n have been proposed, based on a spring-slider stability analysis (Ruina, 1983) or linear elastic fracture mechanics (Rubin & Ampuero, 2005). Although the latter better suits the continuum problem considered here, we use the ratio L_{VW}/h^* (spring-slider stability analysis) for consistency with previous work (Song & McLaskey, 2024), where h^* is defined as:

$$h^* = G \cdot D_c / [\sigma_n \cdot (b - a)] \quad (4.3)$$

where G is shear stiffness (2 GPa for PMMA), D_c is the characteristic slip distance (in state evolution), a and b are frictional parameters, and σ_n is the normal stress. In linear elastic fracture mechanics, the L_n is given by L_∞, defined as:

$$L_\infty = [b \cdot G \cdot D_c] / [\pi \sigma_n \cdot (b - a)^2] \quad (4.4)$$

The frictional properties of glassy polymers fall within the following ranges: (b - a) =

0.0044 - 0.005, D_c = 0.2 - 0.35 μm, and b = 0.0144 - 0.016 (Kaneko et al., 2016; Lu, 2009). We used the following PMMA friction parameters: (b - a) = 0.005, D_c = 0.35 μm, and b = 0.016, for consistency with a similar experimental setup in Song & McLaskey (2024). This yields h^* = 8.75 mm at 16 MPa and h^*/L_∞ = 0.98 (Equations 4.3 and 4.4), meaning that the methodological approach does not vary significantly between spring-slider stability analysis and linear elastic fracture mechanics. Since L_{VW} = 275 mm for the OP tests, L_{VW}/h^* is 31 in the OP tests. From the previous experimental study (Song & McLaskey, 2024), when L_{VW}/h^* = 31, the corresponding T_r and **M** were ~50 s and ~ -4.0 (with M_0 = 1200 Nm), respectively. Those values corresponded well with our results of the OP tests at 4.5 μm/s loading rate (Table 4.1). Note that the loading rate in Song & McLaskey (2024) is 3 μm/s during the interseismic period, but under our definition of full-cycle average loading rate (total slip over multiple cycles divided by the corresponding time interval), the loading rate is ~4.1 μm/s. Both represent the same loading. For the MP tests, we calculated L_{VW}/h^* = 3 for the individual 25 mm VW patch, close to the transition from slow slip to periodic seismic slip (Song & McLaskey, 2024). Based on the way T_r and M_0 were found to vary as a function of L_{VW}/h^* for a single VW patch, shown in Figure 7 of Song & McLaskey (2024), the collective behavior of the 11 patches observed in the MP tests (T_r = ~8 s and **M** = -4.4 ($M_0 \approx$ 300 Nm) for 4.5 μm/s loading rate (Table 4.1)) corresponds to the behavior of a single patch with L_{VW}/h^* = ~5. Thus, the observed slip behavior in the MP test is closer to that of a single 25 mm VW patch (L_{VW}/h^* = 3), rather than that of a 275 mm VW patch (L_{VW}/h^* = 31). This suggests that the VS barriers primarily result in independent rupture of the VW patches rather than a whole-

fault rupture. Even when ruptures involve multiple VW patches, the presence of the VS barrier significantly constrains their magnitude.

4.5.2. Verification of the fault healing rate from OP tests

Fault healing involves the increase in the contact area of asperities over time, which strengthens the fault (Dieterich & Kilgore, 1994; Marone, 1998a). The static frictional strength of the VW fault (μ_s) tends to grow with the duration of stationary contact (t_{hold}) as described by the following equation:

$$\mu_s = \alpha_s + \beta_s \cdot \log(t_{hold}) \tag{4.5}$$

where α_s is the frictional fault strength when $t_{hold} = 1$ and β_s is the healing rate of the VW fault (Carpenter et al., 2016; Im et al., 2017; Marone & Saffer, 2015; Marone, 1998b; Marone et al., 1995; McLaskey et al., 2012; Tesei et al., 2012; Yasuhara et al., 2005). Frictional healing can be controlled through a pause in loading (Marone, 1998a; McLaskey, 2019; Mclaskey & Yamashita, 2017; Tesei et al., 2012) or by changing the loading rate (McLaskey et al., 2012). The result of the OP tests is consistent with this concept of healing since an increase in T_r resulted in a higher ratio of $\tau_{mech\_peak} / \sigma_{mech}$ (Table 4.1). To quantify the healing parameters, we first calculate the friction of PMMA (μ_{PMMA}), and to do this we defined the peak sample-average friction coefficient ($\tau_{mech\_peak} / \sigma_{mech}$) as follows:

$$\tau_{mech\_peak} / \sigma_{mech} = \mu_{LFI} + \mu_{PMMA} \cdot (A_{PMMA} / A) + \mu_{Teflon} \cdot (A_{Teflon} / A) \tag{4.6}$$

where A is total fault area, A_{Teflon} is the Teflon patch area, A_{PMMA} is the bare PMMA patch area, μ_{LFI} is the friction coefficient of LFI (≈ 0.04 from Figure 4.A1c), and μ_{Teflon} is the friction coefficient of Teflon (≈ 0.016 from Figure 4.A1c). Based on Equation

4.6, the calculated μ_{PMMA} is 0.51, 0.53, and 0.58 for 4.5 μm/s, 1.4μm/s, and 0.45 μm/s, respectively. Assuming that $t_{hold} = T_r$ (see T_r in Table 4.1), the trend line based on three points resulted in healing parameters of $\alpha_s = 0.42$ and $\beta_s = 0.05$ (Equation 4.5). These values were comparable to the PMMA parameters of $\alpha_s = 0.39$ and $\beta_s = 0.05$ from McLaskey et al. (2012) for a rough PMMA fault surface.

4.5.3. Barrier effectiveness of the VS patch with loading rates

While the strength variation in the OP tests is consistent with our understanding of fault healing, we observed a decrease in mainshock **M** with T_r in the MP tests (Figure 4.4). If interpreted in the context of fault healing, this observation would imply an apparent inverse fault healing. Instead, we hypothesize that this observation is due to a change in the effectiveness of the VS barriers as a function of healing time, which is predominantly controlled by loading rate in our experiments. A strong VS barrier caused VW patches to be more likely to rupture independently (0.45 μm/s loading rate in the MP test, Figure 4.3d), whereas the weak VS barrier caused multiple VW patches to rupture simultaneously, leading to a larger **M** (4.5 μm/s loading rate in the MP test, Figure 4.S5). This interpretation aligns with numerical simulation results indicating that accelerated creep rates in the VS patch due to an increased loading rate, reduced the effectiveness of the VS barrier (Ito & Kaneko, 2023).

The effectiveness of the VS barrier, which is equivalent to changes in friction of the VS patch, is controlled by the friction parameter (a - b), initial slip velocity (V_0), and final slip velocity (V) (see Figure 4.A1b):

$$\Delta\mu = (a - b)\cdot\ln(V/V_0). \quad (4.7)$$

Assuming the (a - b) value remains constant under the same normal stress, the sample-average friction coefficient can be controlled by V/V_0. Therefore, a higher V/V_0 ratio enables the VS patch to act as a more effective barrier against dynamic slip compared to a lower V/V_0 ratio. Note that friction parameters can evolve with cumulative shear strain due to changing gouge layers (e.g., Marone et al., 1992; Scuderi et al., 2017), but that is not the case in these experiments (e.g., Figure 4.A1).

To examine the effectiveness of the VS barrier, we analyzed the velocity variations occurring at the VS patches during stick-slip events in the OP tests (Figure 4.7). Due to space constraints, we were unable to directly measure the slip velocity of the VS patches in the MP test; however, we assumed that the same mechanism occurred in both scenarios. The ratio of slip rate (i.e., peak slip rate during the rupture, $\dot{D}_{peak}$, divided by the slip rate prior to the rupture, $\dot{D}_{prior}$) is higher at 0.45 μm/s loading rate compared to 4.5 μm/s loading rate in the VS patch regions (e.g., E1, E2, E7, and E8) (Figure 4.7a). This indicates that a slow loading rate induces a greater change in shear resistance ($\Delta\mu$ in Equation 4.7), leading to a stronger VS barrier (Figure 4.7b). This aligns with our findings in the MP tests, where 0.45 μm/s loading rate induced more independent ruptures than 4.5 μm/s loading rate. We note, however, that the numerical simulations presented in Section 4.5.4.4 suggest a somewhat more complex interpretation. It may not be the VS barriers alone that cause a "stronger barrier" but the combination of both VW and VS patches with slower slip rate (i.e. more healed) that likely work together to more effectively partition the earthquake rupture.

Variations in the effectiveness of the VS barrier at different loading rates led to lower mainshock magnitude at longer T_r in the MP tests, similar to the observations in

natural fault zones. For example, in Parkfield, California, it was more commonly observed that earthquake magnitude was inversely correlated with recurrence time rather than directly correlated (Chen et al., 2010). Similarly, Uchida et al. (2015) demonstrated that the seismic moment of repeating earthquakes increased significantly following the 2011 Tohoku-Oki earthquake, with some sequences showing seismic moment up to 2.8 times greater than those recorded before the 2011 Tohoku-Oki earthquake. This increase in seismic moment was closely linked to the faster loading rate caused by rapid postseismic slip. The surrounding conditionally stable regions became seismically active as they experienced faster loading rates, leading to a larger rupture area and greater seismic moment. This result aligns with our findings that the VS barrier became less effective at faster loading rate, leading to rupturing more VW patches and higher seismic moment. Based on this observation, these natural faults are likely not solely composed of homogeneous VW segments but instead exhibit multiple VS and VW regions.

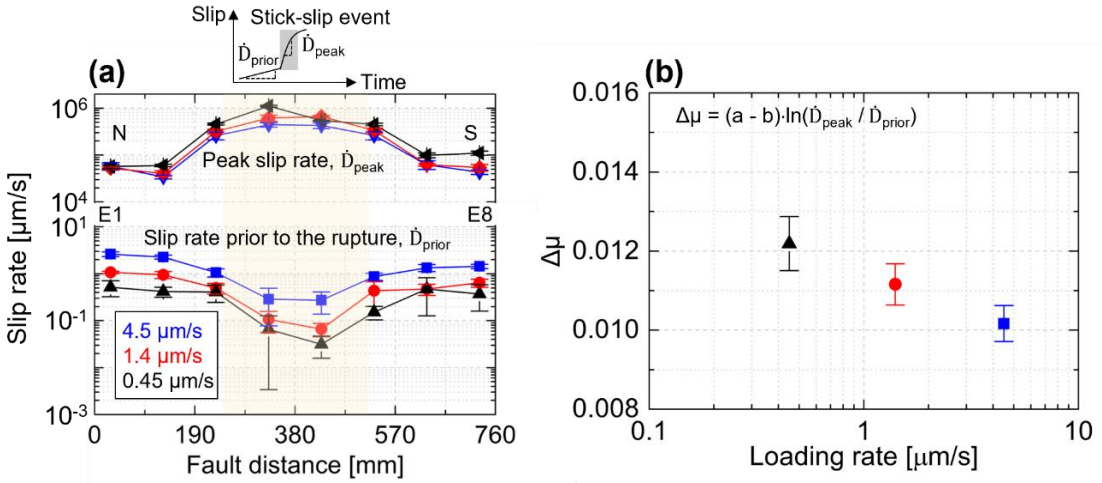

Figure 4.7. (a) Slip rate during the rupture ($\dot{D}_{peak}$) and prior to the rupture ($\dot{D}_{prior}$) with respect to different loading rates in the OP tests. Note that the yellow shaded area indicates the location of the VW patch. (b) Corresponding changes of friction in VS patch areas (e.g., E1, E2, E7, and E8) with different loading rates. (a - b) value is 0.001 under 16 MPa normal stress (Figure 4.A1c).

4.5.4. Main front and back propagation

The foreshocks in the MP tests typically migrated from the forcing end (N) to the leading end (S) (black dotted arrow in Figure 4.6a). However, in some cases, foreshocks propagated in the opposite direction, indicating back propagation (blue dotted arrows in Figure 4.6a). This bidirectional rupture behavior, similar to Rapid Tremor Reversals (RTRs), was also shown in subduction zones, including the southern Kyushu subduction zone in Japan (Yamashita et al., 2015) and the Cascadia subduction zone in North America (Houston et al., 2011; Thomas et al., 2013).

4.5.4.1. Experimental observation of back propagation

We calculated the velocities of the main front and back propagation based on timing and spatial location of the foreshocks in the MP test at 0.45 μm/s loading rate (Figure 4.8). The main front propagation velocity was determined by the linear fitting of the

foreshock hypocenters as shown in Figure 4.6. For example, we calculated the average velocity as the front propagated from VW2 to VW6, noting that its velocity between the two consecutive points appeared to increase from ~0.2 m/s to ~1.1 m/s as it propagated. Similarly, the back propagation velocity was determined by the linear fitting of foreshock hypocenters that extended from the main front back toward the forcing end, in the opposite direction to the main front propagation. For example, the calculated back propagation velocity was ~4 m/s (from two events at -200 ms) and ~13 m/s (from three events at -40 ms) (Figure 4.6a). Over the ten slip cycles, the main front propagated at an average velocity of ~0.67 m/s, while back propagation propagated at an average velocity of ~6.8 m/s (Figure 4.8a), ~10 times faster than the main front (Ding et al., 2024). Following the main front propagation, the mainshock nucleated in VW6 or VW7 (Figure 4.8b). The magnitudes of the events that characterized the main front ranged from **M** -5.2 to -5. These main front events triggered smaller events that migrated in the reverse direction, with magnitudes decreasing as they propagated (Figure 4.8c).

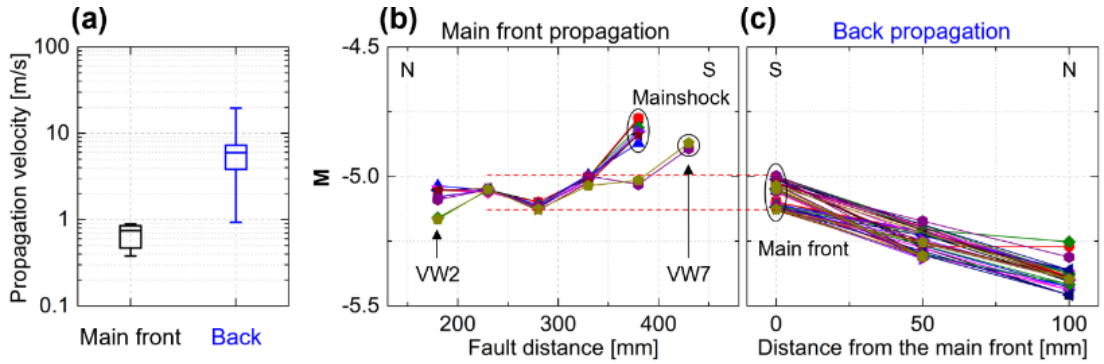

Figure 4.8. (a) The velocities of the main front and back propagations at 0.45 μm/s loading rate in the MP test. The magnitude of (b) the events that characterized the main front propagation and (c) events associated with back propagation from the main front.

4.5.4.2. Numerical simulation

To better understand the mechanics of the laboratory RTRs and our MP experimental system, we developed a matching numerical model using FDRA a quasi-dynamic 2D boundary element framework (Segall & Bradley, 2012; Sun & Cattania, 2025), with a model setup similar to Ito & Kaneko (2023). The fault consisted of alternating VS and VW segments with lengths matching those used in the MP experiments. The normal stress was set to 16 MPa and the fault was loaded with a uniformly increasing shear stressing rate of 4.5 kPa/s applied along the length of the fault to help match the experimental results. The leading end of the fault was modeled as a free boundary condition by using analytical half-space solutions for stress interactions, thus neglecting the effect of other fault boundaries. Loading from the forcing end was modeled with a constant sliding rate of 0.45 μm/s. Friction parameters are provided in Table 4.3. The parameters for PMMA are based on values used previously for similar glassy polymers (described in Section 4.5.1). While most of the parameters were chosen to match experimental conditions or assumed frictional properties of PMMA, some parameters, particularly the shear stressing rate and the friction properties of Teflon, were adjusted to improve agreement with the experimental results. For example, we used (a - b) value of 0.0004 for Teflon in the simulation, instead of 0.001 as observed in this study (Figure 4.A1c) and assumed D_c value of 0.35 μm, which we could not reliably estimate from the experiment (Figure 4.A1b).

Table 4.3. Friction parameters used in numerical simulations.

Parameters	VW (PMMA; Lu, 2009)	VS (Teflon)
a	0.011	0.0024
b	0.016	0.002
(a - b)	-0.005	0.0004
D_c [μm]	0.35	0.35

Figure 4.9 presents our preferred model, which quantitatively reproduces many of the features of the MP experiments. The slip rate is shown as a function of fault distance for both simulation time steps (Figure 4.9a), which, due to adaptive time stepping, emphasizes the more rapidly slipping times associated with foreshocks and mainshocks, and linear time (Figures 4.9b to 4.9d). As the main rupture front propagates, back propagation is also clearly observed (Figure 4.9a).

The experimental features are quite rich, and we have attempted to constrain the input friction parameters by quantitatively matching the following features (see Figure 4.6a for the experimental results): (1) Discrete seismic events with slip rate greater than 10 mm/s characterize the main front and back-propagating (RTR) fronts, (2) first foreshock occurs ~0.5 s before the mainshock, (3) the propagation velocity of the main front accelerates as it progresses across the sample from the VW1 to VW6, (4) the main front velocity is ~0.5 m/s at ~0.5 s prior to the mainshock, (5) the RTR front velocities increase with proximity to the mainshock, (6) the RTR front propagation velocity (200 ms prior to the mainshock) is 10 times faster than the main front, and (7) discrete events in the RTRs become weaker as they propagate back from the main front. In the simulations, this is quantified with decreasing maximum slip rate, whereas in the experiments, this is quantified with decreasing seismic moment. Though our model matches (1-7) above, it does not match all the features of the MP

and OP tests, particularly the recurrence time, since the simplified model does not account for the finite size and 3-D nature of the experimental configuration. This discrepancy may affect our estimates, so we acknowledge that the friction parameters listed in Table 4.3 are not fully constrained by our model.

We were also able to produce simulations that reproduced the general RTR-like behavior even when some of the features, such as propagation velocity of the main and back-propagating fronts, differed by orders of magnitude in the experiment. When comparing our results with the km-scale simulations of Ito & Kaneko (2023), which also included alternating VW and VS patches, their larger scale and greater number of patches produced more detailed patterns of foreshocks, enabling analysis of b-values. Nevertheless, both studies commonly observed foreshocks with some degree of back propagation. This suggests that RTR-like behavior is rather universal and can be relatively easily achieved with heterogeneous interfaces that host slow slip fronts, consistent with recent results on RTRs on rough faults (Sun & Cattania, 2025). The driving mechanism behind the RTR is further examined in Section 4.5.4.4 through numerical simulation results.

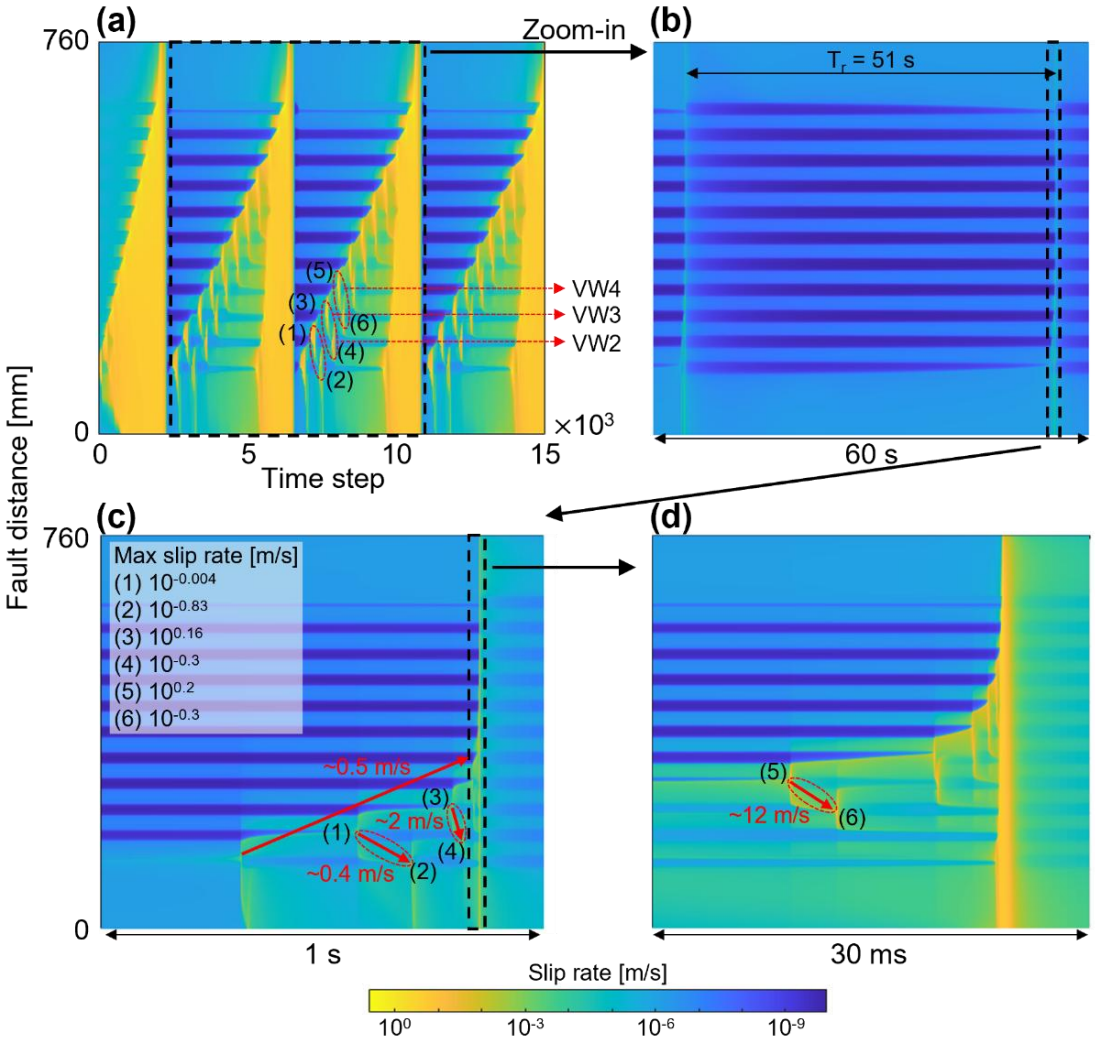

Figure 4.9. (a) Evolution of slip event cycles over the time step of the MP test at 0.45 μm/s loading rate. Zoomed-in time scales: (b) 60 s, (c) 1 s, and (d) 30 ms. Note that the average main front velocity is ~0.5 m/s, while the average RTR migration velocity is ~5 m/s. The numbers from (1) to (6) indicate a sequence of slip events in chronological order.

4.5.4.3. Comparing back propagation in subduction zones

The RTR-like behavior observed in both experimental and numerical results shows parallels with RTRs in subduction zones. For instance, RTR events in subduction zones have been shown to propagate at velocities between 2 m/s and 4.6 m/s, which is also ~10 times faster than typical main front propagation velocities (Hawthorne et al.,

2016; Houston et al., 2011; Rubin & Armbruster, 2013; Yamashita et al., 2015). Further, previous studies have noted that the events get weaker during RTRs. For example, the estimated stress drop from RTR events was only half of that observed during the main front propagation (Hawthorne et al., 2016) and the seismic energy radiated from RTR events is an order of magnitude smaller than that from the main front events (Ando et al., 2012). These behaviors suggested that the mechanics underlying RTRs in subduction zones might share similar features with our fault conditions.

4.5.4.4. Variations in fault healing affect back propagation

In this Section, we use the numerical simulation results to show that the faster back propagation and slower forward propagation occur because the fault is more healed and more locked ahead of the main front than behind it. Additionally, the differences in peak strength on the VW patches ahead of and behind the main front are roughly consistent with our estimates based on healing rate.

Figure 4.10 shows the evolution of slip rate in the numerical simulations during the rupture of VW3, rerupture of VW2, and rupture of VW4. These correspond to events (3), (4), and (5) in Figure 4.9a, respectively. In Figure 4.10a, the slip rate increases to seismic slip rates within VW3 at t_2. After that time, slip rate decreases to a lower level on VW3 while it increases in both directions: forward, in the direction of the main rupture front propagation, toward VW4, which has a slower slip rate and is therefore more locked, and backward, over the previously ruptured section toward VW2, which has a higher slip rate and is therefore less locked. Figure 4.10b shows VW2 increases

to seismic slip rates at t_6, while VW4 takes much longer to accelerate, and reaches seismic slip rates at t_8. In Figure 4.10c, seismic slip in VW4 causes an increase in slip rate at VW3 (t_{10}) in preparation for its rerupture.

Variation in fault healing time explains the differences in peak shear stress in the simulation, shown in Figure 4.10d. If we consider the healing time of a VW patch as the time since the previous rupture on that patch, the healing time for VW3 and VW4 is ~51 s, measured from the previous mainshock. In contrast, VW2 had just ruptured in the main front and had thus only healed for ~0.24 s. Given these time intervals (~51 s for VW4 and ~0.24 s for VW2), the resulting difference in the friction coefficient is 0.116 between the VW2 and VW4 (Equation 4.5 and $\beta_s = 0.05$). With 16 MPa normal stress, this corresponds to a difference in shear strength of ~1.8 MPa. Assuming that the peak shear stress at rupture onset is similar to the peak shear strength of each VW patch, the observed peak shear stresses of ~10.4 MPa for VW2 and ~11.8 MPa for VW4, yield a difference of ~1.4 MPa (Figure 4.10d), which roughly aligns with ~1.8 MPa from the calculation.

The simulation results show that the back propagation occurs more quickly than the forward propagation primarily due to differences in the VW patches ahead of and behind the rupture rather than the VS patches. In contrast, slip rates on the VS patches ahead of and behind VW3 are similar, indicating that the barrier effect is similar. This provides a more nuanced interpretation that might also be extended to the mechanism for the lower mainshock magnitude at longer T_r in the MP tests described in Figure 4.4: at longer T_r, it is not just the VS barriers that become more effective at breaking the multiple VW patches up into separate ruptures, but also the combination of both

VW and VS patches with slower slip rate (i.e. more healed) that work together to partition the earthquake rupture.

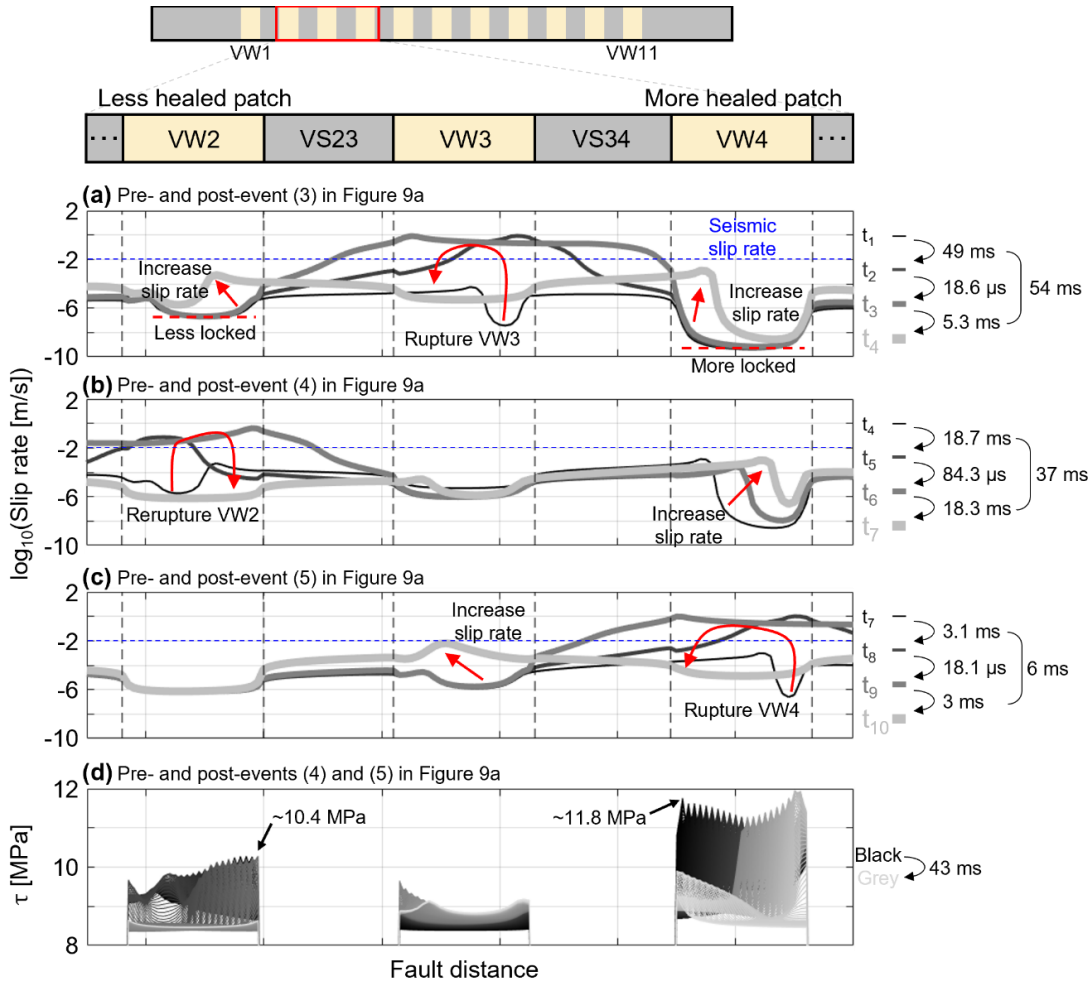

Figure 4.10. Simulated slip rate and shear stress evolution during the rupture of VW3, the rerupture of VW2, and the rupture of VW4, corresponding to events (3), (4), and (5) in Figure 4.9a, respectively. (a) The slip rate evolves within VW3 and subsequently decreases to the residual level, while VW2 and VW4 begin to accelerate. (b) The slip rate evolves and drops to the residual level in VW2, while it continues to evolve in VW4. (c) The slip rate eventually drops to the residual level in VW4, leading to an increase in slip rate at VW3 in preparation for its rerupture. (d) The shear stress evolution when VW2 and VW4 rupture, corresponding to the stages shown in (b) and (c).

4.5.5. Implications of the aftershocks

Aftershocks are rarely observed in laboratory experiments, likely due to the uniformity of the fault surface, whereas natural fault systems are far more complex than experimental setups. However, aftershocks have been observed in some rock experiments (Davidsen et al., 2021; Goebel et al., 2023). Some evidence suggests that aftershocks are driven by the redistribution of residual stress following a mainshock. Goebel et al. (2023) found that fault roughness played a significant role in the generation of the aftershocks, as rough faults retained higher residual stress due to smaller stress drops during the events. This uneven stress distribution led to localized stress concentrations that trigger aftershocks. Davidsen et al. (2021) demonstrated that post-fracture stress relaxation and large-scale irregularities, such as imperfections in the fault surface, helped trigger aftershocks by concentrating stress in specific areas. Together, these findings highlight that aftershocks were driven by the residual stress and energy left on the fault after the mainshock, with fault roughness and heterogeneities significantly influencing the distribution of these residual stresses. We hypothesize that in most previous experiments, the effects of fault roughness and heterogeneities, along with variations in stress relaxation, were not sufficiently significant to trigger aftershocks, which might explain the rare observation of the aftershocks in those studies.

To investigate the cause of aftershocks in the MP tests, we analyzed how the number of hypocenters of the aftershocks and the amount of afterslip vary with fault distance (Figure 4.11). The afterslip was measured over 0.1 s, starting immediately after the mainshock ended (see Figure 4.S6), during which all aftershocks had already occurred

within 0.1 s (Figure 4.5a). We divided the data into three categories based on the mainshock nucleation patch: all mainshocks nucleated on either VW3, VW6, or VW7, and the remaining VW patches located South of the nucleation region ruptured together during the mainshock (colored bidirectional arrow in Figure 4.11). For example, if the mainshock nucleated at VW3, the rupture extended from VW3 to VW11. Figure 4.11a shows the hypocenters of the aftershocks in relation to the mainshock nucleation patch. While aftershocks in the VW3 mainshock predominantly occurred at the boundary of the rupture area, most aftershocks in the VW6 and VW7 mainshocks clearly nucleated within the rupture zone, suggesting that aftershock activity is closely linked to the mainshock rupture area. Figure 4.11b shows the afterslip occurring within 0.1 s following the mainshock illustrating the slip deficit from the mainshock and the preceding interseismic slip. The maximum afterslip occurred either within the mainshock rupture area (e.g., VW3 and VW6) or at its boundary (e.g., VW7), which was similar to the results in Figure 4.11a. These findings indicate that aftershocks are associated with the mainshock rupture area and rapid afterslip, and that fewer aftershocks nucleated outside of the mainshock rupture area where the afterslip was slower.

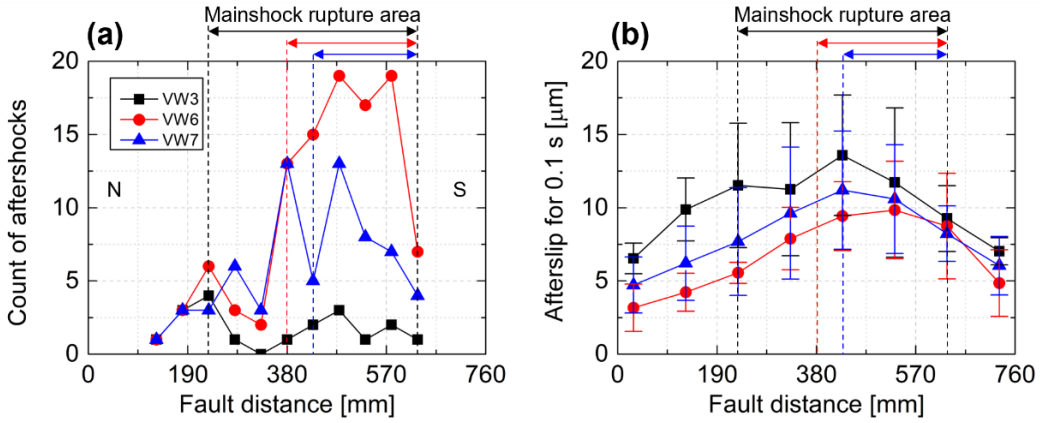

Figure 4.11. (a) Number of nucleation location of the aftershocks with different loading rates with respect to the nucleation patch of the mainshock (e.g., VW3, VW6 and VW7) in the MP tests. (b) Afterslip for 0.1 s after the mainshock. The colored bidirectional arrow indicates the rupture area caused by the mainshock. Note that method used to calculate afterslip for 0.1 s is shown in Figure 4.S6.

In numerical simulations featuring similar fault conditions (e.g., alternating VW and VS patches along the fault), aftershocks were also observed due to a slip deficit at the boundaries of the area ruptured by the mainshock (Yabe & Ide, 2018). This slip deficit resulted from strain accumulation that was not fully released during the mainshock, as the VS patch barriers were sufficiently robust to stop the rupture. However, as the (a - b) value of the VS patch decreased (i.e., becoming velocity neutral or a weak barrier), the slip deficit diminished, resulting in a mainshock without aftershocks (Yabe & Ide, 2018). Similarly, in the OP tests, no barriers were present within the VW patch, resulting in the rare observation of aftershocks. The nucleation location of the aftershocks for VW6 and VW7 was dominant within the mainshock rupture area (Figure 4.11a), which was slightly different from numerical simulation findings, where the slip deficit was exclusively observed at the periphery of the mainshock area. Nevertheless, our results support the findings in natural faults that the aftershock zone

is a good proxy for the mainshock rupture area (Neo et al., 2021).

4.6. Conclusions

We conducted biaxial experiments using a 760 mm PMMA sample to investigate the effect of VS patches interspersed within a VW patch. We directly compared a single, unbroken VW patch (OP tests) to a case where the VW patch was partitioned by VS patches (MP tests) with the same total VW area. While both the OP and MP tests exhibited stick-slip events, the MP tests were characterized by the occurrence of foreshocks, mainshock, and aftershocks within a slip cycle. In contrast, the OP tests typically produced only one large seismic event, the mainshock, in a slip cycle. The recurrence time, total slip, maximum slip rate, and magnitude in the OP tests were roughly an order of magnitude larger than those in the MP tests under the same loading rate. Even though the VW fault area was the same in both tests, the VS barriers between the VW patches inhibited fast rupture propagation and reduced the slip and stress drop in the MP tests.

We also varied the loading rate to examine its effects. In the OP tests, the mainshock magnitude increased as the loading rate decreased because the long recurrence time allowed the fault to heal more and this produced somewhat higher strength drops and therefore somewhat larger earthquakes. In the MP tests, however, the magnitude of the mainshock decreased as the loading rate decreased. Reducing the loading rate increased the amount of healing time and allowed both the VW patches and VS barriers to become more locked (slower slip rate) this combination more effectively prevented the VW patches from rupturing together in a large seismic event. Thus, a

faster loading rate (and shorter healing time) promoted the simultaneous rupture of multiple VW patches with larger overall magnitudes, while slow loading rates encouraged independent ruptures with smaller magnitudes.

In the MP tests with a strong VS barrier (i.e., 0.45 μm/s loading rate), we observed sequences of small seismic events that tracked a slowly propagating main front and faster migration of seismicity propagating from the main front back over the areas that had already slipped, with the migration velocity of back propagation being ~10 times faster than that of the main front propagation. This behavior is similar to a phenomenon known as Rapid Tremor Reversals (RTRs) observed in subduction zones. We found that the more rapid back propagation compared to slower forward propagation can be attributed to the differential healing time ahead of the slow front compared to behind the slow front. Confirmed using numerical simulation of the RTR-like behavior, the less healed VW patches and VS barriers behind the slower main front ruptured more readily than the more thoroughly healed (and locked) patches ahead of the main front. Thus, it appears that a similar mechanism to that associated with lower mainshock magnitude at longer recurrence time in the MP tests also contributes to RTRs: fault sections with long healing times are more effectively locked (slower local slip rates) and this can slow the propagation velocity of slow fronts and can inhibit dynamic ruptures from simultaneously rupturing multiple VW patches separated by barriers. In contrast, short healing times do not allow fault sections to lock up as effectively (faster local slip rates, though still very low) and this enables faster propagation of slow fronts and allow dynamic rupture to propagate through VS barriers to produce larger earthquakes.

Overall, this study demonstrates that frictional heterogeneity of the fault plays a crucial role in determining the mechanical behavior and seismic activity of the fault and also highlights how the behavior of heterogeneous faults can be non-intuitive and highly nonlinear. Understanding these dynamics provides insights into the complex mechanisms of fault healing and has significant implications for predicting seismic behavior, thereby improving strategies for seismic hazard mitigation.

4.7. Appendix

Figure 4.A1 shows the experimental setup and results for the Teflon's friction parameter using a double-direct shear configuration. We made identical PMMA stationary blocks with dimensions of 760 mm by 102 mm by 38 mm in x, y, and z directions, respectively (Figure 4.A1a). The PMMA moving block has dimensions of 800 mm by 152 mm by 38 mm in x, y, and z directions, respectively. Teflon was applied across the entire faults, allowing us to measure the friction parameters of both faults. Two Eddy current sensors (e.g., E1 and E2) were installed to verify if the faults slipped simultaneously. We sheared the moving block by ~2 mm under a normal stress of 16 MPa and applied normal stresses of 4, 8, 2, and 16 MPa, shearing ~2 mm at each stress level before starting to record. Figure 4.A1b shows the sample-average friction coefficient derived from the ratio of shear to normal stresses. The loading rate was varied from 0.45 to 4.5 μm/s to observe the effects on the two faults. We divided the results of friction coefficient (Figure 4.A1b) by a factor of two to obtain the coefficient of friction of one of the two Teflon interfaces (Figure 4.A1c). The friction coefficient and (a - b) decreased with increased normal stress, similar to the results of Song &

McLaskey (2024). However, the results from Song & McLaskey (2024) included the friction of both LFI composed of reinforced Teflon sliding against precision ground steel and the Teflon-coated PMMA interfaces studied here. Therefore, by comparing these values, the calculated sample-average friction coefficient of LFI is ~0.04.

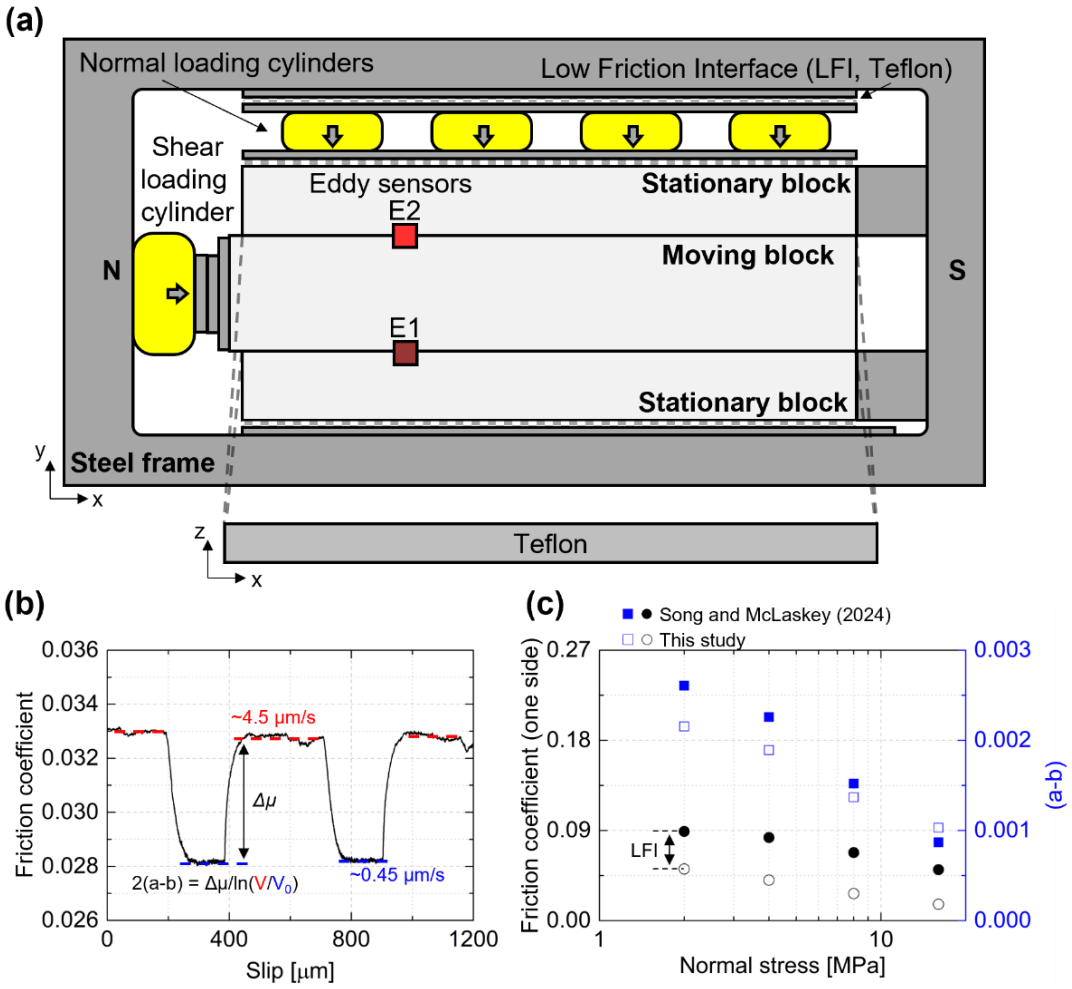

Figure 4.A1. (a) Double-direct shear experimental setup for determining Teflon's friction parameters. (b) Sample-average friction coefficient from shear and normal stresses with varying loading rates (0.45 μm/s and 4.5 μm/s) at 16 MPa normal stress. Note that this exhibited the combined friction coefficient of both Teflon-coated PMMA faults. (c) The sample-average friction coefficient of one Teflon-coated PMMA frictional interface (4.5 μm/s loading rate) was compared to the combined friction of one Teflon-coated PMMA interface with LFI (Song & McLaskey, 2024), with corresponding estimates of (a - b) values also provided.

4.8. Supplementary Figures

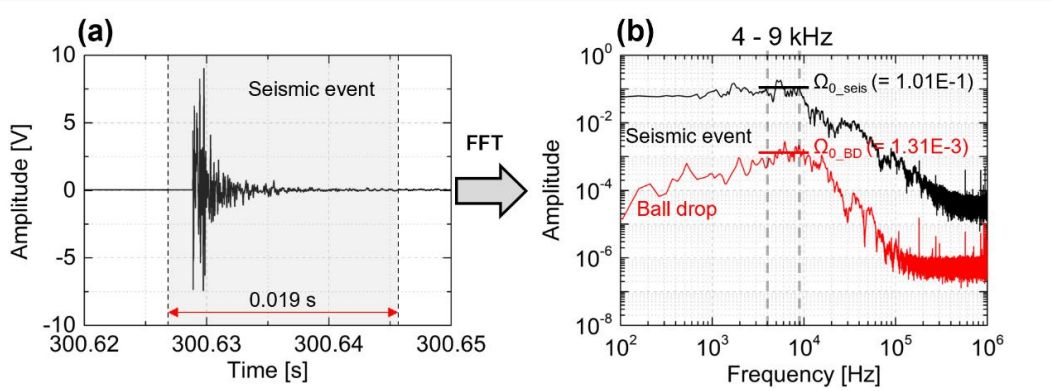

Figure 4.S1. (a) The signal of a stick-slip event by P3 at 4.5 μm/s loading rate in the OP test. The time window was 19 ms for Fourier Transform. (b) Signal amplitude in the frequency domain, averaged from sensors P1, P3, P5, and P7. Calibration of ground motion for seismic events was performed using the ball drop method, detailed in prior studies (Cebry & McLaskey, 2024; McLaskey et al., 2015; Song & McLaskey, 2024; Wu & McLaskey, 2019). Thick solid lines indicated the averages amplitude in the frequency range between 4 and 9 kHz, which was used to calibrate the seismic moment of the events.

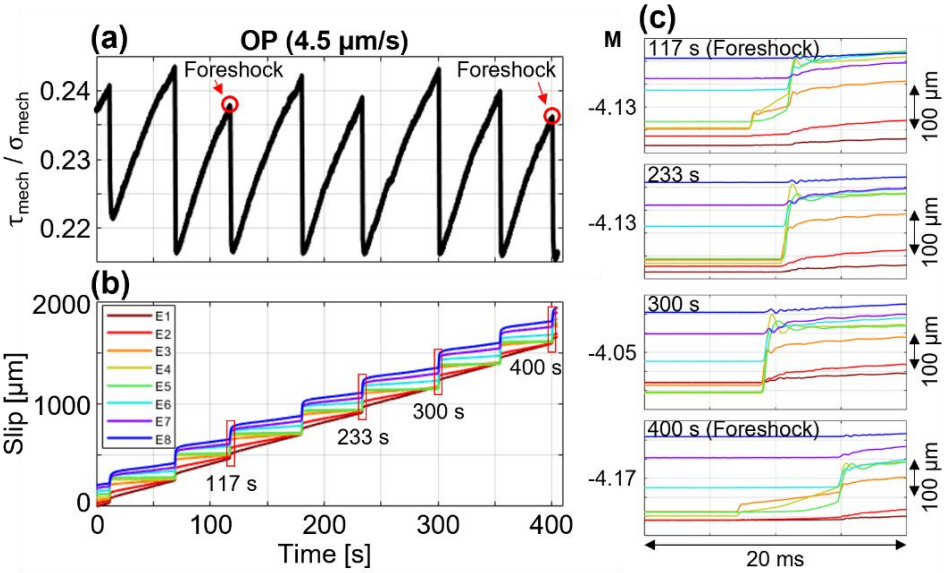

Figure 4.S2. (a) Sample-average friction coefficient (τ_{mech} / σ_{mech}) of the OP tests at 4.5 μm/s loading rate and (b) corresponding slip. (c) Detailed slip over 20 ms near four example stick slip events (times are labeled). We found that mainshocks with a foreshock occurred at lower values of peak τ_{mech} / σ_{mech} compared to those without a foreshock, yet the magnitude of the mainshocks is about the same with or without the presence of foreshocks.

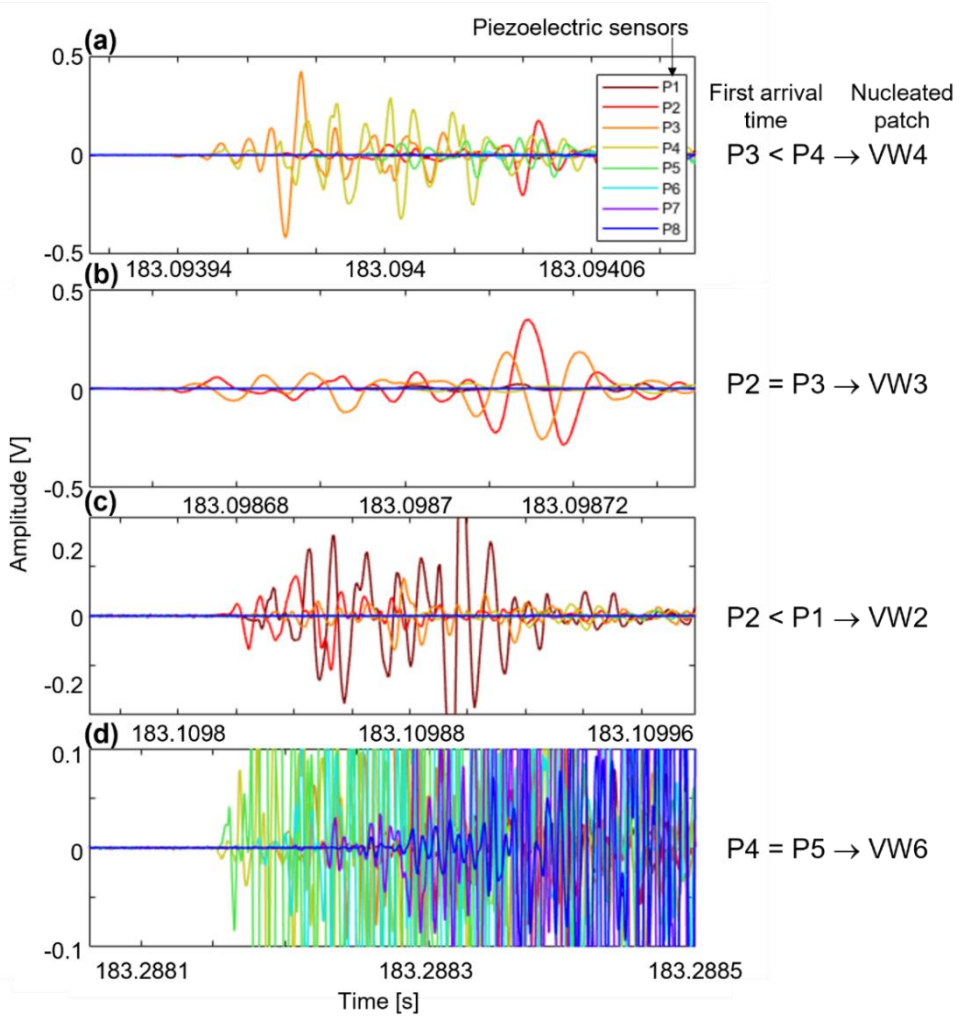

Figure 4.S3. The estimation of the source location based on the first arrival time of the Piezoelectric sensors (e.g., P1 to P8) in the MP test. Note that the location was roughly estimated using the relative arrival times of the two closest piezoelectric sensors (see Figure 4.1b for the detailed location of the sensors).

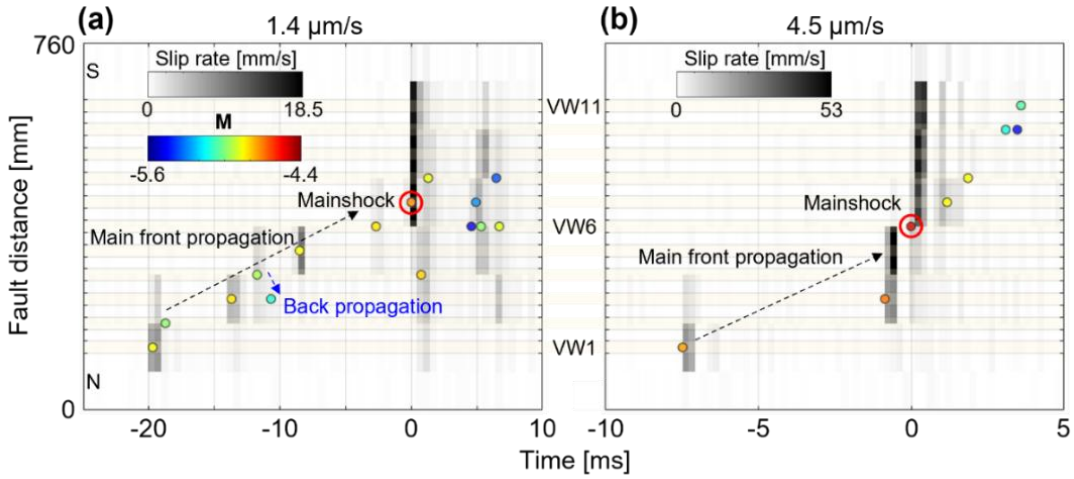

Figure 4.S4. Locations and magnitudes of events in the MP test at loading rates of (a) 1.4 μm/s and (b) 4.5 μm/s loading rates. The background color is from the slip rate, averaging over different time windows (0.5 ms for Figure 4.S4a and 0.2 ms for Figure 4.S4b). The 4.5 μm/s loading rate rarely shows back propagation, whereas the 1.4 μm/s rate reveals back propagations that are less pronounced than the prominent back propagation observed at 0.45 μm/s loading rate in Figure 4.6a.

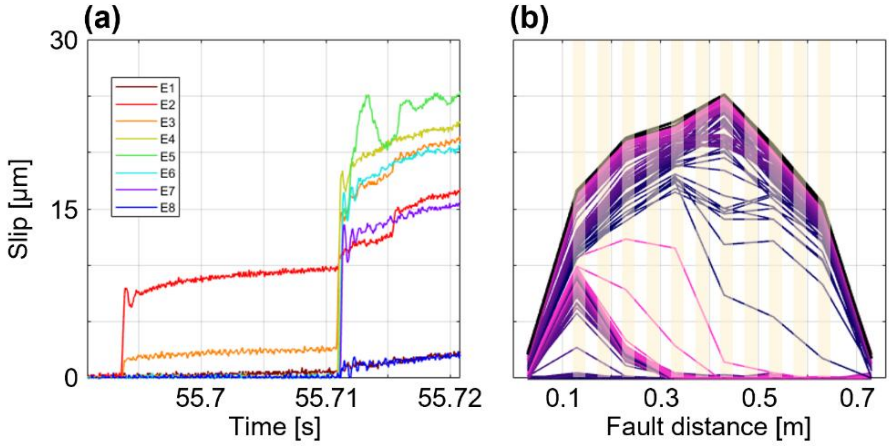

Figure 4.S5. Representative slip event with (a) time and (b) fault distance in MP test at 4.5 μm/s loading rate. Note that fast loading rate (4.5 μm/s) induces the simultaneous rupture of multiple VW patches as compared to the slower loading rate (0.45 μm/s) illustrated in Figures 4.3b and 4.3d.

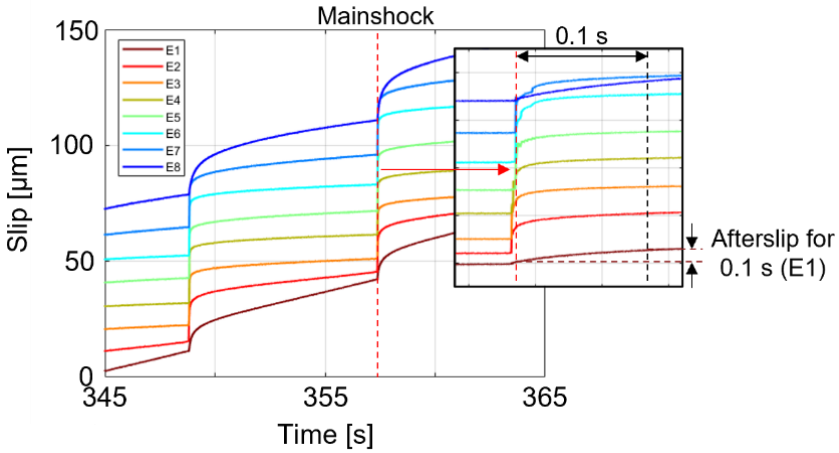

Figure 4.S6. Representative slip from the MP tests using Eddy sensors at 4.5 μm/s loading rate. Afterslip for 0.1 s was obtained from the slip occurring during the 0.1 s immediately following the mainshock.

REFERENCES

Ando, R., Takeda, N., & Yamashita, T. (2012). Propagation dynamics of seismic and aseismic slip governed by fault heterogeneity and Newtonian rheology. *Journal of Geophysical Research: Solid Earth*, *117*(11), 1–14. https://doi.org/10.1029/2012JB009532

Anthony, J. L., & Marone, C. (2005). Influence of particle characteristics on granular friction. *Journal of Geophysical Research: Solid Earth*, *110*(8), 1–14. https://doi.org/10.1029/2004JB003399

Barbot, S. (2019). Slow-slip, slow earthquakes, period-two cycles, full and partial ruptures, and deterministic chaos in a single asperity fault. *Tectonophysics*, *768*(July), 228171. https://doi.org/10.1016/j.tecto.2019.228171

Bedford, J. D., Faulkner, D. R., & Lapusta, N. (2022). Fault rock heterogeneity can produce fault weakness and reduce fault stability. *Nature Communications*, *13*(1), 326. https://doi.org/10.1038/s41467-022-27998-2

Bolton, D. C., Shreedharan, S., Rivière, J., & Marone, C. (2021). Frequency-Magnitude Statistics of Laboratory Foreshocks Vary With Shear Velocity, Fault Slip Rate, and Shear Stress. *Journal of Geophysical Research: Solid Earth*, *126*(11). https://doi.org/10.1029/2021JB022175

Bolton, D. C., Marone, C., Saffer, D., & Trugman, D. T. (2023). Foreshock properties illuminate nucleation processes of slow and fast laboratory earthquakes. *Nature Communications*, *14*(1). https://doi.org/10.1038/s41467-023-39399-0

Buijze, L., Guo, Y., Niemeijer, A. R., Ma, S., & Spiers, C. J. (2021). Effects of heterogeneous gouge segments on the slip behavior of experimental faults at dm scale. *Earth and Planetary Science Letters*, *554*(December 2020). https://doi.org/10.1016/j.epsl.2020.116652

Carpenter, B. M., Ikari, M. J., & Marone, C. (2016). Laboratory observations of time-dependent frictional strengthening and stress relaxation in natural and synthetic fault gouges. *Journal of Geophysical Research: Solid Earth*, *121*(2), 1183–1201. https://doi.org/10.1002/2015JB012136

Cattania, C. (2019). Complex Earthquake Sequences On Simple Faults. *Geophysical Research Letters*, *46*(17–18), 10384–10393. https://doi.org/10.1029/2019GL083628

Cattania, C., & Segall, P. (2019). Crack Models of Repeating Earthquakes Predict Observed Moment-Recurrence Scaling. *Journal of Geophysical Research: Solid Earth*, *124*(1), 476–503. https://doi.org/10.1029/2018JB016056

Cattania, C., & Segall, P. (2021). Precursory Slow Slip and Foreshocks on Rough Faults. *Journal of Geophysical Research: Solid Earth*, *126*(4), 1–20. https://doi.org/10.1029/2020JB020430

Cebry, S. B. L., & McLaskey, G. C. (2021). Seismic swarms produced by rapid fluid injection into a low permeability laboratory fault. *Earth and Planetary Science Letters*, *557*, 116726. https://doi.org/10.1016/j.epsl.2020.116726

Cebry, S. B. L., & McLaskey, G. C. (2024). Heterogeneous high frequency seismic radiation from complex ruptures. *Seismica*, *3*(2). https://doi.org/10.26443/seismica.v3i2.1351

Cebry, S. B. L., Sorhaindo, K., & McLaskey, G. C. (2023). Laboratory Earthquake Rupture Interactions With a High Normal Stress Bump. *Journal of Geophysical Research: Solid Earth*, *128*(11), 1–24. https://doi.org/10.1029/2023JB027297

Chen, K., Bürgmann, R., Nadeau, R. M., Chen, T., & Lapusta, N. (2010). Postseismic variations in seismic moment and recurrence interval of repeating earthquakes. *Earth and Planetary Science Letters*, *299*(1–2), 118–125. https://doi.org/10.1016/j.epsl.2010.08.027

Chen, T., & Lapusta, N. (2009). Scaling of small repeating earthquakes explained by interaction of seismic and aseismic slip in a rate and state fault model. *Journal of Geophysical Research: Solid Earth*, *114*(1), 1–12. https://doi.org/10.1029/2008JB005749

Collettini, C., Niemeijer, A., Viti, C., Smith, S. A. F., & Marone, C. (2011). Fault structure, frictional properties and mixed-mode fault slip behavior. *Earth and Planetary Science Letters*, *311*(3–4), 316–327. https://doi.org/10.1016/j.epsl.2011.09.020

Corbi, F., Mastella, G., Tinti, E., Rosenau, M., Sandri, L., Pardo, S., & Funiciello, F. (2024). Asperity Size and Neighboring Segments Can Change the Frictional Response and Fault Slip Behavior: Insights From Laboratory Experiments and Numerical Simulations. *Journal of Geophysical Research: Solid Earth*, *129*(1), 1–16. https://doi.org/10.1029/2023JB026594

Davidsen, J., Goebel, T., Kwiatek, G., Stanchits, S., Baró, J., & Dresen, G. (2021). What Controls the Presence and Characteristics of Aftershocks in Rock Fracture in the Lab? *Journal of Geophysical Research: Solid Earth*, *126*(10), 1–25. https://doi.org/10.1029/2021JB022539

Dieterich, J. H. (1992). Earthquake nucleation on faults with rate-and state-dependent strength. *Tectonophysics*, *211*(1–4), 115–134. https://doi.org/10.1016/0040-1951(92)90055-B

Dieterich, J. H., & Kilgore, B. D. (1994). Direct observation of frictional contacts:

New insights for state-dependent properties. *Pure and Applied Geophysics PAGEOPH*, *143*(1–3), 283–302. https://doi.org/10.1007/BF00874332

Ding, X., Xu, S., Fukuyama, E., & Yamashita, F. (2024). Back-Propagating Rupture: Nature, Excitation, and Implications. *Journal of Geophysical Research: Solid Earth*, *129*(10). https://doi.org/10.1029/2024JB029629

Dresen, G., Kwiatek, G., Goebel, T., & Ben-Zion, Y. (2020). Seismic and Aseismic Preparatory Processes Before Large Stick–Slip Failure. *Pure and Applied Geophysics*, *177*(12), 5741–5760. https://doi.org/10.1007/s00024-020-02605-x

Dublanchet, P. (2018). The dynamics of earthquake precursors controlled by effective friction. *Geophysical Journal International*, *212*(2), 853–871. https://doi.org/10.1093/gji/ggx438

Dublanchet, P., Bernard, P., & Favreau, P. (2013). Interactions and triggering in a 3-D rate-and-state asperity model. *Journal of Geophysical Research: Solid Earth*, *118*(5), 2225–2245. https://doi.org/10.1002/jgrb.50187

Fryer, B., Giorgetti, C., Passelègue, F., Momeni, S., Lecampion, B., & Violay, M. (2022). The Influence of Roughness on Experimental Fault Mechanical Behavior and Associated Microseismicity. *Journal of Geophysical Research: Solid Earth*, *127*(8). https://doi.org/10.1029/2022JB025113

Goebel, T. H. W., Kwiatek, G., Becker, T. W., Brodsky, E. E., & Dresen, G. (2017). What allows seismic events to grow big?: Insights from b-value and fault roughness analysis in laboratory stick-slip experiments. *Geology*, *45*(9), 815–818. https://doi.org/10.1130/G39147.1

Goebel, T. H. W., Brodsky, E. E., & Dresen, G. (2023). Fault Roughness Promotes Earthquake-Like Aftershock Clustering in the Lab. *Geophysical Research Letters*, *50*(8), 1–11. https://doi.org/10.1029/2022GL101241

Guérin-Marthe, S., Nielsen, S., Bird, R., Giani, S., & Di Toro, G. (2019). Earthquake Nucleation Size: Evidence of Loading Rate Dependence in Laboratory Faults. *Journal of Geophysical Research: Solid Earth*, *124*(1), 689–708. https://doi.org/10.1029/2018JB016803

Hanks, T. C., & Kanamori, H. (1979). A moment magnitude scale. *Journal of Geophysical Research B: Solid Earth*, *84*(B5), 2348–2350. https://doi.org/10.1029/JB084iB05p02348

Hawthorne, J. C., Bostock, M. G., Royer, A. A., & Thomas, A. M. (2016). Variations in slow slip moment rate associated with rapid tremor reversals in Cascadia. *Geochemistry, Geophysics, Geosystems*, *17*(12), 4899–4919. https://doi.org/10.1002/2016GC006489

Houston, H., Delbridge, B. G., Wech, A. G., & Creager, K. C. (2011). Rapid tremor reversals in Cascadia generated by a weakened plate interface. *Nature Geoscience*, *4*(6), 404–409. https://doi.org/10.1038/ngeo1157

Ikari, M. J., Marone, C., & Saffer, D. M. (2011). On the relation between fault strength and frictional stability. *Geology*, *39*(1), 83–86. https://doi.org/10.1130/G31416.1

Im, K., Elsworth, D., Marone, C., & Leeman, J. (2017). The Impact of Frictional Healing on Stick-Slip Recurrence Interval and Stress Drop: Implications for Earthquake Scaling. *Journal of Geophysical Research: Solid Earth*, *122*(12), 10,102-10,117. https://doi.org/10.1002/2017JB014476

Ito, R., & Kaneko, Y. (2023). Physical Mechanism for a Temporal Decrease of the Gutenberg-Richter b-Value Prior to a Large Earthquake. *Journal of Geophysical Research: Solid Earth*, *128*(12), 1–21. https://doi.org/10.1029/2023JB027413

Kaneko, Y., & Lapusta, N. (2010). Supershear transition due to a free surface in 3-D simulations of spontaneous dynamic rupture on vertical strike-slip faults. *Tectonophysics*, *493*(3–4), 272–284. https://doi.org/10.1016/j.tecto.2010.06.015

Kaneko, Y., Lapusta, N., & Ampuero, J. P. (2008). Spectral element modeling of spontaneous earthquake rupture on rate and state faults: Effect of velocity-strengthening friction at shallow depths. *Journal of Geophysical Research: Solid Earth*, *113*(9), 1–17. https://doi.org/10.1029/2007JB005553

Kaneko, Y., Avouac, J. P., & Lapusta, N. (2010). Towards inferring earthquake patterns from geodetic observations of interseismic coupling. *Nature Geoscience*, *3*(5), 363–369. https://doi.org/10.1038/ngeo843

Kaneko, Y., Nielsen, S., & Carpenter, B. M. (2016). The onset of laboratory earthquakes explained by nucleating rupture on a rate-and-state fault. *Journal of Geophysical Research: Solid Earth*, *121*(8), 6071–6091. https://doi.org/10.1002/2016JB013143

Karner, S. L., & Marone, C. (2000). *Geocomplexity and the Physics of Earthquakes*. *Geophysical Monograph Series* (Vol. 120). https://doi.org/10.1029/GM120

Kato, N. (2004). Interaction of slip on asperities: Numerical simulation of seismic cycles on a two-dimensional planar fault with nonuniform frictional property. *Journal of Geophysical Research: Solid Earth*, *109*(B12), 1–17. https://doi.org/10.1029/2004JB003001

Kato, N., & Yoshida, S. (2011). A shallow strong patch model for the 2011 great Tohoku-oki earthquake: A numerical simulation. *Geophysical Research Letters*, *38*(15), 1–5. https://doi.org/10.1029/2011GL048565

Konca, A. O., Avouac, J. P., Sladen, A., Meltzner, A. J., Sieh, K., Fang, P., et al. (2008). Partial rupture of a locked patch of the Sumatra megathrust during the 2007 earthquake sequence. *Nature*, *456*(7222), 631–635. https://doi.org/10.1038/nature07572

Leeman, J. R., Saffer, D. M., Scuderi, M. M., & Marone, C. (2016). Laboratory observations of slow earthquakes and the spectrum of tectonic fault slip modes. *Nature Communications*, *7*(1), 11104. https://doi.org/10.1038/ncomms11104

Leeman, J. R., Marone, C., & Saffer, D. M. (2018). Frictional Mechanics of Slow Earthquakes. *Journal of Geophysical Research: Solid Earth*, *123*(9), 7931–7949. https://doi.org/10.1029/2018JB015768

Lu, X. (2009). Combined experimental and numerical study of spontaneous dynamic rupture on frictional interfaces. *California Institute of Technology*.

Lui, S. K. Y., & Lapusta, N. (2016). Repeating microearthquake sequences interact predominantly through postseismic slip. *Nature Communications*, *7*, 1–7. https://doi.org/10.1038/ncomms13020

Lui, S. K. Y., & Lapusta, N. (2018). Modeling High Stress Drops, Scaling, Interaction, and Irregularity of Repeating Earthquake Sequences Near Parkfield. *Journal of Geophysical Research: Solid Earth*, *123*(12), 10,854-10,879. https://doi.org/10.1029/2018JB016472

Marone, C. (1998a). Laboratory-derived friction laws and their application to seismic faulting. *Annual Review of Earth and Planetary Sciences*, *26*(1), 643–696. https://doi.org/10.1146/annurev.earth.26.1.643

Marone, C. (1998b). The effect of loading rate on static friction and the rate of fault healing during the earthquake cycle. *Nature*, *391*(6662), 69–72. https://doi.org/10.1038/34157

Marone, C., & Saffer, D. M. (2015). The Mechanics of Frictional Healing and Slip Instability During the Seismic Cycle. In *Treatise on Geophysics* (Vol. 4, pp. 111–138). Elsevier. https://doi.org/10.1016/B978-0-444-53802-4.00092-0

Marone, C., Raleigh, C. B., & Scholz, C. H. (1990). Frictional behavior and constitutive modeling of simulated fault gouge. *Journal of Geophysical Research*, *95*(B5), 7007–7025. https://doi.org/10.1029/JB095iB05p07007

Marone, C., Scholtz, C. H., & Bilham, R. (1991). On the mechanics of earthquake afterslip. *Journal of Geophysical Research*, *96*(B5), 8441–8452. https://doi.org/10.1029/91JB00275

Marone, C., Hobbs, B. E., & Ord, A. (1992). Coulomb constitutive laws for friction: Contrasts in frictional behavior for distributed and localized shear. *Pure and*

Applied Geophysics, *139*(2), 195–214. https://doi.org/10.1007/BF00876327

Marone, C., Vidale, J. E., & Ellsworth, W. L. (1995). Fault healing inferred from time dependent variations in source properties of repeating earthquakes. *Geophysical Research Letters*, *22*(22), 3095–3098. https://doi.org/10.1029/95GL03076

Mclaskey, G. C., & Yamashita, F. (2017). Slow and fast ruptures on a laboratory fault controlled by loading characteristics. *Journal of Geophysical Research: Solid Earth*, *122*(5), 3719–3738. https://doi.org/10.1002/2016JB013681

McLaskey, G. C. (2019). Earthquake Initiation From Laboratory Observations and Implications for Foreshocks. *Journal of Geophysical Research: Solid Earth*, *124*(12), 12882–12904. https://doi.org/10.1029/2019JB018363

McLaskey, G. C., & Lockner, D. A. (2014). Preslip and cascade processes initiating laboratory stick slip. *Journal of Geophysical Research: Solid Earth*, *119*(8), 6323–6336. https://doi.org/10.1002/2014JB011220

McLaskey, G. C., Thomas, A. M., Glaser, S. D., & Nadeau, R. M. (2012). Fault healing promotes high-frequency earthquakes in laboratory experiments and on natural faults. *Nature*, *491*(7422), 101–104. https://doi.org/10.1038/nature11512

McLaskey, G. C., Lockner, D. A., Kilgore, B. D., & Beeler, N. M. (2015). A Robust Calibration Technique for Acoustic Emission Systems Based on Momentum Transfer from a Ball Drop. *Bulletin of the Seismological Society of America*, *105*(1), 257–271. https://doi.org/10.1785/0120140170

Mei, C., Barbot, S., Jia, Y., & Wu, W. (2022). Experimental evidence for multiple controls on fault stability and rupture dynamics. *Earth and Planetary Science Letters*, *577*, 117252. https://doi.org/10.1016/j.epsl.2021.117252

Nakata, R., Ando, R., Hori, T., & Ide, S. (2011). Generation mechanism of slow earthquakes: Numerical analysis based on a dynamic model with brittle-ductile mixed fault heterogeneity. *Journal of Geophysical Research*, *116*(B8), B08308. https://doi.org/10.1029/2010JB008188

Neo, J. C., Huang, Y., Yao, D., & Wei, S. (2021). Is the aftershock zone area a good proxy for the mainshock rupture area? *Bulletin of the Seismological Society of America*, *111*(1), 424–438. https://doi.org/10.1785/0120190200

Passelègue, F. X., Latour, S., Schubnel, A., Nielsen, S., Bhat, H. S., & Madariaga, R. (2017). Influence of Fault Strength on Precursory Processes During Laboratory Earthquakes. In *Geophysical Monograph Series* (pp. 229–242). https://doi.org/10.1002/9781119156895.ch12

Rice, J. R., & Ruina, A. L. (1983). Stability of Steady Frictional Slipping. *Journal of Applied Mechanics*, *50*(2), 343–349. https://doi.org/10.1115/1.3167042

Rubin, A. M., & Ampuero, J.-P. (2005). Earthquake nucleation on (aging) rate and state faults. *Journal of Geophysical Research: Solid Earth*, *110*(B11), 1–24. https://doi.org/10.1029/2005JB003686

Rubin, A. M., & Armbruster, J. G. (2013). Imaging slow slip fronts in Cascadia with high precision cross-station tremor locations. *Geochemistry, Geophysics, Geosystems*, *14*(12), 5371–5392. https://doi.org/10.1002/2013GC005031

Ruina, A. (1983). Slip instability and state variable friction laws. *Journal of Geophysical Research: Solid Earth*, *88*(B12), 10359–10370. https://doi.org/10.1029/JB088iB12p10359

Scholz, C. H. (1968). Experimental study of the fracturing process in brittle rock. *Journal of Geophysical Research*, *73*(4), 1447–1454. https://doi.org/10.1029/jb073i004p01447

Scuderi, M. M., Marone, C., Tinti, E., Di Stefano, G., & Collettini, C. (2016). Precursory changes in seismic velocity for the spectrum of earthquake failure modes. *Nature Geoscience*, *9*(9), 695–700. https://doi.org/10.1038/ngeo2775

Scuderi, M. M., Collettini, C., Viti, C., Tinti, E., & Marone, C. (2017). Evolution of shear fabric in granular fault gouge from stable sliding to stick slip and implications for fault slip mode. *Geology*, *45*(8), 731–734. https://doi.org/10.1130/G39033.1

Segall, P., & Bradley, A. M. (2012). Slow-slip evolves into megathrust earthquakes in 2D numerical simulations. *Geophysical Research Letters*, *39*(18), 2–6. https://doi.org/10.1029/2012GL052811

Song, J. Y., & McLaskey, G. C. (2024). Laboratory Earthquake Ruptures Contained by Velocity Strengthening Fault Patches. *Journal of Geophysical Research: Solid Earth*, *129*(4), 1–16. https://doi.org/10.1029/2023JB028509

Song, J. Y., Cattania, C., & McLaskey, G. C. (2025). Fault healing and asperity partitioning on a frictionally heterogeneous laboratory fault [Dataset]. Cornell eCommons. https://doi.org/10.7298/8tjz-2e50

Sun, Y., & Cattania, C. (2025). Propagation of Slow Slip Events on Rough Faults: Clustering, Back Propagation, and Re-Rupturing. *Journal of Geophysical Research: Solid Earth*, *130*(2). https://doi.org/10.1029/2024JB029384

Tesei, T., Collettini, C., Carpenter, B. M., Viti, C., & Marone, C. (2012). Frictional strength and healing behavior of phyllosilicate-rich faults. *Journal of Geophysical Research: Solid Earth*, *117*(9), 1–13. https://doi.org/10.1029/2012JB009204

Tesei, T., Collettini, C., Barchi, M. R., Carpenter, B. M., & Di Stefano, G. (2014).

Heterogeneous strength and fault zone complexity of carbonate-bearing thrusts with possible implications for seismicity. *Earth and Planetary Science Letters*, *408*, 307–318. https://doi.org/10.1016/j.epsl.2014.10.021

Thomas, T. W., Vidale, J. E., Houston, H., Creager, K. C., Sweet, J. R., & Ghosh, A. (2013). Evidence for tidal triggering of high-amplitude rapid tremor reversals and tremor streaks in northern Cascadia. *Geophysical Research Letters*, *40*(16), 4254–4259. https://doi.org/10.1002/grl.50832

Uchida, N., Shimamura, K., Matsuzawa, T., & Okada, T. (2015). Postseismic response of repeating earthquakes around the 2011 Tohoku-oki earthquake: Moment increases due to the fast loading rate. *Journal of Geophysical Research: Solid Earth*, *120*(1), 259–274. https://doi.org/10.1002/2013JB010933

Wei, M., & Shi, P. (2021). Synchronization of Earthquake Cycles of Adjacent Segments on Oceanic Transform Faults Revealed by Numerical Simulation in the Framework of Rate-and-State Friction. *Journal of Geophysical Research: Solid Earth*, *126*(1), 1–15. https://doi.org/10.1029/2020JB020231

Wu, B. S., & McLaskey, G. C. (2018). Broadband Calibration of Acoustic Emission and Ultrasonic Sensors from Generalized Ray Theory and Finite Element Models. *Journal of Nondestructive Evaluation*, *37*(1), 1–16. https://doi.org/10.1007/s10921-018-0462-8

Wu, B. S., & McLaskey, G. C. (2019). Contained Laboratory Earthquakes Ranging From Slow to Fast. *Journal of Geophysical Research: Solid Earth*, *124*(10), 10270–10291. https://doi.org/10.1029/2019JB017865

Yabe, S., & Ide, S. (2018). Why Do Aftershocks Occur Within the Rupture Area of a Large Earthquake? *Geophysical Research Letters*, *45*(10), 4780–4787. https://doi.org/10.1029/2018GL077843

Yamanaka, Y., & Kikuchi, M. (2004). Asperity map along the subduction zone in northeastern Japan inferred from regional seismic data. *Journal of Geophysical Research: Solid Earth*, *109*(B7). https://doi.org/10.1029/2003JB002683

Yamashita, F., Fukuyama, E., Xu, S., Kawakata, H., Mizoguchi, K., & Takizawa, S. (2021). Two end-member earthquake preparations illuminated by foreshock activity on a meter-scale laboratory fault. *Nature Communications*, *12*(1), 1–11. https://doi.org/10.1038/s41467-021-24625-4

Yamashita, Y., Yakiwara, H., Asano, Y., Shimizu, H., Uchida, K., Hirano, S., et al. (2015). Migrating tremor off southern Kyushu as evidence for slow slip of a shallow subduction interface. *Science*, *348*(6235), 676–679. https://doi.org/10.1126/science.aaa4242

Yasuhara, H., Marone, C., & Elsworth, D. (2005). Fault zone restrengthening and

frictional healing: The role of pressure solution. *Journal of Geophysical Research: Solid Earth*, *110*(6), 1–11. https://doi.org/10.1029/2004JB003327

Zhou, X., He, Y., & Shou, Y. (2021). Experimental investigation of the effects of loading rate, contact roughness, and normal stress on the stick-slip behavior of faults. *Tectonophysics*, *816*(July 2020), 229027. https://doi.org/10.1016/j.tecto.2021.229027

CHAPTER 5

Seismicity Migration from Fluid Injection: Laboratory Experiments and Numerical Models Illuminate Volume-Driven versus Pressure-Diffusion-Driven Migration

This chapter is drawn from the Preprinted paper: *Song, J.Y., Liu, L., Arson, C., and McLaskey, G.C., 2025. Seismicity Migration from Fluid Injection: Laboratory Experiments and Numerical Models Illuminate Volume-Driven versus Pressure-Diffusion-Driven Migration. Submitted to Earth and Planetary Science Letters. https://doi.org/10.31223/X5QM9J*

5.1. Abstract

Fluid injection into the subsurface can induce seismicity by reactivating shear rupture, which typically produces larger earthquake magnitudes than tensile rupture. In laboratory shear rupture experiments, pressurization of the entire fault is often limited because large unconfined samples allow fluid to leak at free surfaces. In this study, we investigated shear fault reactivation by directly injecting fluid into a PMMA fault (760 mm long, 76 mm high) formed as the interface between two separate PMMA blocks. To prevent leakage in the 76 mm dimension, we made a low permeability barrier by coating the outer edges of the fault with Teflon tape. Fluid pressure then extended along the 760 mm dimension, resulting in the migration of seismicity away from the injection well. Changes in injection rate and fluid viscosity revealed two mechanisms: (1) slow injection rate or low-viscosity fluid caused seismicity migration governed by

pressure diffusion, and (2) fast injection rate or high-viscosity fluid caused seismicity migration proportional to injected volume. Simulations with a 2D poroelastic model showed that seismicity migrated with the fluid pressure front in the volume-driven regime, whereas fluid pressure advanced well ahead of seismicity in the pressure-diffusion-driven regime. These results highlight that Teflon tape effectively sealed faults and controlled fluid flow, and that injection rate and fluid viscosity have a strong impact on fault slip and induced seismicity.

5.2. Introduction

Fluid injection into the subsurface serves a variety of geo-engineering purposes, including the disposal of large volumes of wastewater (Bao & Eaton, 2016; Keranen et al., 2014) and Carbon Capture and Storage (CCS) (Stork et al., 2015). However, such practices have been shown to elevate the risk of seismicity by reactivating faults. For example, the **M** 5.7 Prague and **M** 5.8 Pawnee earthquakes in Oklahoma, USA, were triggered by high-volume wastewater disposal (Barbour et al., 2017; Keranen et al., 2014). Beyond waste disposal, fluid injection is also employed to fracture rock (i.e., hydraulic fracturing) in applications such as Enhanced Geothermal Systems (EGS) (Majer et al., 2007) and enhanced hydrocarbon recovery (Atkinson et al., 2016; Ellsworth, 2013). Yet these operations have also been linked to induced seismicity. Notable examples include the **M** 5.5 event at Pohang (South Korea), the **M** 3.9 event at Fox creek, Alberta (Canada), the **M** 4 event at the Eagle Ford Formation, South Texas (USA), and the **M** 2.9 event at Garvin County, Oklahoma (USA) (Bao & Eaton, 2016; Fasola et al., 2019; Grigoli et al., 2018; Holland, 2013; Schultz et al., 2020).

Given these risks, understanding the mechanisms of induced seismicity is crucial for mitigating potential risks to infrastructure and communities.

Fluid injection may produce tensile hydraulic fracture (Jaeger et al., 2009; Scholz, 2002) if the associated fluid pressure exceeds the tensile strength of the rock. This tensile (Mode 1) fracture typically produces only low magnitude microseismic events, often below magnitude 0 (Eaton, 2018; Eaton et al., 2018; Maxwell, 2014). Under sufficient deviatoric stress, fluid injection may significantly reduce effective normal stress. According to the Coulomb failure criterion, this stress reduction can trigger shear slip (Mode 2 and Mode 3 fractures), even without reaching tensile conditions (Jaeger et al., 2009; Scholz, 2002). Shear fractures tend to release more strain energy than tensile fracture, often resulting in larger earthquakes (Kanamori & Brodsky, 2004; Lockner, 1995).

Earthquakes associated with fluid injections are mainly attributed to pore pressure diffusion. High pressures near the injection well cause elevated pore pressure on nearby faults and fractures, which reduces the effective normal stress and reduces the resistance to shear. Pore pressure diffusion models suggest a migration of seismicity fronts for which the distance from the injection well is proportional to $\sqrt{\alpha t}$, with α and t representing hydraulic diffusivity and time, respectively (Shapiro et al., 1997, 2002). Based on this relationship, hydraulic diffusivity has been inferred from seismic fronts, as observed in Basel (Switzerland), Soultz-sous-Forets (France), Cotton Valley (USA), Fenton hill (USA) (Mukuhira et al., 2017; Parotidis et al., 2004). Other studies noted that poroelastic stresses can also affect induced seismicity, and may be important in formations with little hydraulic connectivity (e.g. Chang and Segall,

2016; Zhai et al., 2019). Another mechanism that drives induced seismicity involves stress redistribution resulting from aseismic slip. The increased pore pressure first triggers aseismic slip, which expands outward from an injection well. As the slipping region extends beyond the area of the pressurized region, stress is transferred to adjacent locked segments, potentially triggering seismicity. This phenomenon has been observed in in-situ faults, experiments, and simulations (Bhattacharya & Viesca, 2019; Cappa et al., 2019; Guglielmi et al., 2015; Yang et al., 2023).

In laboratory studies, both tensile fractures and shear fractures have been systematically investigated to understand the mechanisms of fracture propagation and fault slip behavior under various conditions. Tensile fracture experiments have quantified fracture growth with fluid injection (Cochard et al., 2024; Ha et al., 2018; Liu et al., 2018; Yuan et al., 2024; Zhao et al., 2022), examined fracture patterns and breakdown pressure in heterogeneous layers of rocks (Teufel & Clark, 1984), and highlighted the effects of pressurization rate, viscosity of injected fluid, and cyclic injection on the breakdown pressure (Ha et al., 2018; Ishida et al., 2004; Lockner & Byerlee, 1977; Patel et al., 2017; Zoback et al., 1977). In contrast, shear fracture experiments have primarily focused on how fluids affect fault stability. For example, injection rate strongly affects slip behavior. Higher rates promote unstable slip and dynamic ruptures, while slower injection favors aseismic creep and stable sliding, thereby reducing the risk of induced seismicity (Gori et al., 2021; Ji et al., 2022; Wang et al., 2020). Fault roughness also affects slip behavior by enhancing permeability through shear dilation as asperities open faults (Ye & Ghassemi, 2018), while heterogeneous stress distributions concentrate seismic activity around asperities,

leading to localized slip zones (Wang et al., 2024).

Previous shear fracture laboratory experiments have primarily been conducted on small fault samples (typically less than 100 mm in length), which may not fully capture the complexities of larger fault systems. To overcome this limitation, longer samples (e.g., ~1 m or ~3 m in length) were used for fluid injection experiments, where fluid was directly injected into the fault (Cebry et al., 2022; Cebry & McLaskey, 2021). However, the large samples have a slab-like geometry and are typically unconfined, so fluid can diffuse to a free surface of the sample relatively close to the injection well (e.g., 38 mm diffusion distance for a 760 mm-long fault; Cebry and McLaskey, 2021). This limits the extent of pressurization along the fault and causes seismicity to occur predominantly near the injection well.

In this study, we investigated shear fracture by fluid injection, but we applied Teflon to the laboratory fault surface to reduce hydraulic diffusivity, confine the fluid, and extend the diffusion distance from 38 mm to 380 mm. The Teflon surface treatment is identical to that reported in Song and McLaskey (2024), used to modify the fault friction properties. We compared experiments with Confined Fluid (CF), where Teflon was attached along the top and bottom of the fault to produce a diffusion distance of 380 mm, to experiments with Open Fluid (OF), which has a 38 mm diffusion distance, similar to the setup in Cebry and McLaskey (2021). Both types of experiments produced several tiny seismic events. However, the CF experiments allowed fluid pressure to weaken a larger portion of the laboratory fault, and we often observed seismicity migration away from the injection well. The effects of injection rate and fluid viscosity were investigated, revealing two distinct seismic migration

mechanisms: (1) pressure-diffusion-driven migration, occurring at slow injection rate or low-viscosity fluid and (2) volume-driven migration, occurring at fast injection rate or high-viscosity fluid. To better understand the mechanisms behind the migration of seismicity, a 2D numerical model was developed incorporating Darcy flow and poroelasticity. With the volume-driven regime, the fluid pressure built up faster than it diffused away, forcing the fault open and abruptly increasing the porosity and permeability of fault zone. The resulting reduction of effective normal stress allowed the fault to slip and release stored shear strain energy as a sequence of seismic events, which migrated faster than those solely driven by pore pressure diffusion.

5.3. Experimental materials and methods

5.3.1. Experimental setup

The experiment was conducted in a biaxial machine (Cebry & McLaskey, 2021; Mclaskey & Yamashita, 2017; Song & McLaskey, 2024), with the setup illustrated in the top-view diagram (Figure 5.1a). Two Polymethyl methacrylate (PMMA) blocks were used: the moving block measured 760 mm × 203 mm × 76.2 mm, while the stationary block measured 790 mm × 152 mm × 76.2 mm in the x, y, and z directions, respectively. The stationary block included 4 mm diameter injection holes drilled in it that allowed fluid to directly reach the fault plane (Figure 5.1b). Normal force was applied using four hydraulic cylinders, while shear force was exerted on the moving block to induce slip along the fault plane. To minimize friction from surfaces other than the fault, Teflon sheets were inserted at the steel-to-steel (Low Friction Interface, LFI) and PMMA-to-steel interfaces. The friction coefficient of these non-fault

surfaces is ~0.04 (Song et al., 2025). The end of the fault near the shear hydraulic cylinder (i.e., forcing end), is defined as the North (N) end, while the opposite end (i.e., leading end) is defined as the South (S) end.

To measure the fault slip and seismic waves, we used Eddy current sensors (square symbols) and Piezoelectric sensors (triangle symbols), respectively (Figure 5.1a), attached to the sample with hot glue (Stanley, DualMelt). The Eddy current sensors, labeled E1 to E8, were positioned along the top of the block at 100 mm intervals in x-direction. Each Eddy current sensor consisted of a probe attached to the stationary block and a steel target fixed to the moving block. Displacement of the probe relative to the target was interpreted as fault slip, recorded at 20 kHz sampling rate with a resolution of ~0.15 μm. The Piezoelectric sensors (Panametrics, V103), labeled P1 to P8, were positioned at 100 mm intervals in x-direction and placed 40 mm away from the fault plane in y-direction. The Piezoelectric sensors were recorded continuously at 20 kHz and also at 2 MHz for 50 ms time windows when the signal exceeded the noise level.

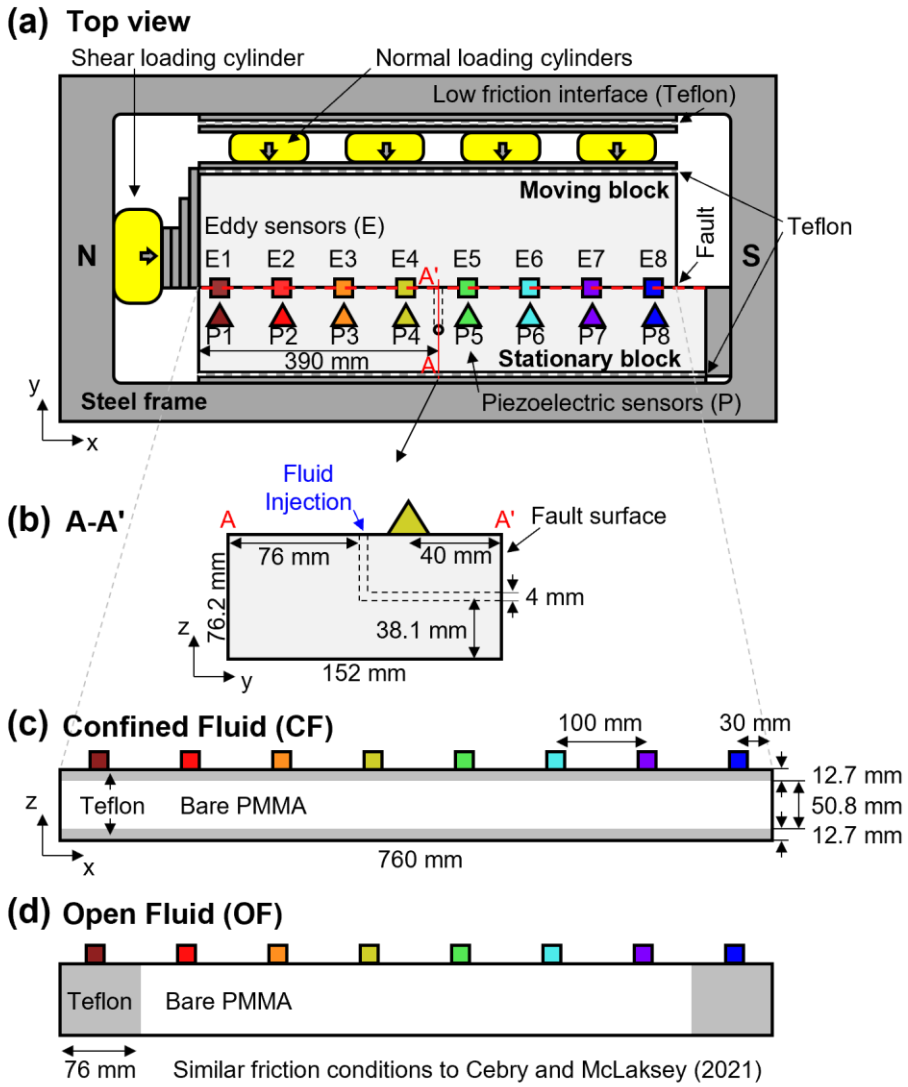

Figure 5.1. (a) Top view of biaxial experimental setup. Note that 'E' and 'P' are Eddy and Piezoelectric sensors, respectively. (b) A-A' plane of stationary block for the fluid injection details. Fault conditions for (c) Confined Fluid (CF) and (d) Open Fluid (OF), which is similar to the friction conditions shown in Cebry and McLaskey (2021).

5.3.2. Fault conditions

The surfaces of the PMMA blocks were fly-cut flat and then roughened using 80-grit abrasive. In the CF setup, we applied Teflon tape (Hyper Tough, 12.7 mm wide) to both sides of the fault in the (x, y) plane to prevent fluid leakage (Figure 5.1c). To

attach the Teflon tape to the fault, the Teflon tape was extended along the designated fault surface and fixed at both ends with adhesive tape. Before assembling the blocks, we placed plastic wrap (GLAD, Clingwrap) between the Teflon areas to prevent adhesion between them (Song & McLaskey, 2024). In the bare PMMA region, we pre-wetted the fault with the injected fluid to ensure saturated conditions before testing. In the experimental setup by Cebry and McLaskey (2021), Talc was applied to the fault edge to induce Velocity-Strengthening (VS) behavior. To replicate similar fault conditions (an Open Fluid setup, OF), we attached Teflon, also known for its velocity-strengthening (VS) behavior (Song & McLaskey, 2024), to both ends of the faults (Figure 5.1d). Comparing the CF and OF setups enabled the investigation of how the Teflon arrangement affected fluid pathways and seismicity patterns.

5.3.3. Experimental procedure

We applied a constant normal force to the x-z sample boundary which resulted in 8 MPa sample-average normal stress on the fault for all cases. We then increased shear force on the y-z sample boundary on the moving block to produce a constant ~3 μm/s loading rate. Before conducting each experiment, we sheared the moving block by ~2 mm to avoid a run-in phase, characterized by frictional evolution with continued slip (Song & McLaskey, 2024). Once completed, we sheared the sample to generate one or two complete rupture seismic slip events (see Figure 5.2a). We then paused shearing for 10 s when the sample-average shear stress on the fault reached a midpoint between the peak (τ_{peak}) and residual (τ_{res}) shear stresses (Figure 5.2), after which we injected fluid according to the specified injection rates and fluid types listed in Table 5.1.

Water (viscosity: 1 mPa·s) and a more viscous fluid (viscosity: 50 mPa·s), composed of 28 % water and 72 % glycerin (PTI Process Chemicals, Glycerin 99 %) by weight, were injected directly onto the fault surface.

Table 5.1. Experimental conditions.

Experiment	Name	Fault condition	Injection rate [ml/min]	Injected fluid
1	OF8W	Open Fluid	8	Water
2	CF16W	Confined Fluid	16	Water
3	CF8W	Confined Fluid	8	Water
4	CF4W	Confined Fluid	4	Water
5	CF2W	Confined Fluid	2	Water
6	CF1W	Confined Fluid	1	Water
7	CF1V	Confined Fluid	1	Viscous fluid
8	CF0.5V	Confined Fluid	0.5	Viscous fluid

5.3.4. Hypocenter locations and magnitude of seismicity

During fluid injection onto the fault, swarms of seismic slip events were detected by Piezoelectric sensors, shown in Figure 5.3. Using the recorded waveforms, we determined the hypocenter locations and estimated the moments of individual seismic slip events.

To locate the hypocenter of the seismic slip events, we used the first P-wave arrival times. Specifically, we selected the four earliest arrival times from eight sensors (P1 to P8; see Figure 5.S1a). An array of possible hypocenter locations was constructed along the x-direction with a spacing of 0.02 mm, covering a total length of 760 mm and resulting in 38,000 points. For each point, we computed a cost function as described below:

$$\text{Cost}(x) = \sum_{i=1}^{4} \left| (t_i - t_0) - \sqrt{(x - x_i)^2 + (y - y_i)^2 + (z - z_i)^2}/V_p \right|, \quad (5.1)$$

where t_i is the i^{th} Piezoelectric sensor's first arrival time and (x_i, y_i, z_i) are the i^{th} sensor's spatial coordinates, t_0 is the estimated origin time of the seismic source, and V_P is the P-wave velocity (2650 m/s for PMMA). We confine this localization to the x dimension only by assuming that the events originated near the center of the fault such that ($y - y_i$) is fixed to 40 mm, and ($z - z_i$) is fixed to 38.1 mm. The hypocenter location (x) that minimized Equation 5.1 was identified as the hypocenter (see Figure 5.S1c).

To obtain the seismic moment of the seismic slip events, we utilized the Fourier domain using the Fast Fourier Transform (FFT) algorithm. Since the recorded signals included instrument response, they were calibrated using a reference source which is a ball impact, which has been validated in previous studies (Cebry & McLaskey, 2024; McLaskey et al., 2015; Song et al., 2025; Song & McLaskey, 2024). We dropped a steel ball (~2.38 mm diameter) from a height of 0.91 m, measured the seismic signals, and calculated the equivalent seismic moment of this ball drop (M_{0_BD}) (see McLaskey et al., 2015; Song et al., 2025 for details). We then performed an FFT on the signals from all sensors and averaged the resulting spectra (Figure 5.S1b). To estimate the moment of the seismic slip event (M_{0_SE}), we compared the amplitude of the FFT of the seismic event to that of the ball drop event in the 4 - 9 kHz frequency range. This frequency band was chosen because it is below the corner frequency of the ball drop (~25.6 kHz; see Wu and McLaskey, 2018 for details) and still had high Signal-to-Noise Ratio (SNR) in both the ball drop and seismic event. Finally, we converted the seismic moment to magnitude (**M**) using the empirical relation (Hanks & Kanamori, 1979)

$$\mathbf{M} = 2/3 \cdot \log(M_{0\_SE}) - 6.067. \quad (5.2)$$

5.4. Experimental Results

5.4.1. The effect of Open Fluid and Confined Fluid

The effect of the Teflon tape used to confine the fluid is examined in Figure 5.2, which compares the OF8W and CF8W tests. The CF test exhibited larger shear stress reduction and slip compared to the OF test. For example, the sample-averaged shear stress in CF8W dropped by ~2 MPa, which is five times greater than the ~0.4 MPa drop observed in OF8W. The corresponding slip for CF8W reached ~1200 μm, which is four times larger than ~300 μm slip observed in OF8W. In the pore pressure evolution, the OF pressure remained stable at ~10 MPa (Figure 5.2a), likely due to fluid leakage at the top and bottom of the sample, which prevented further pressure buildup (Cebry & McLaskey, 2021). In contrast, the CF test showed a pressure drop to 8 MPa (Figure 5.2b), likely due to a high permeability layer by the Teflon (Section 5.6.3).

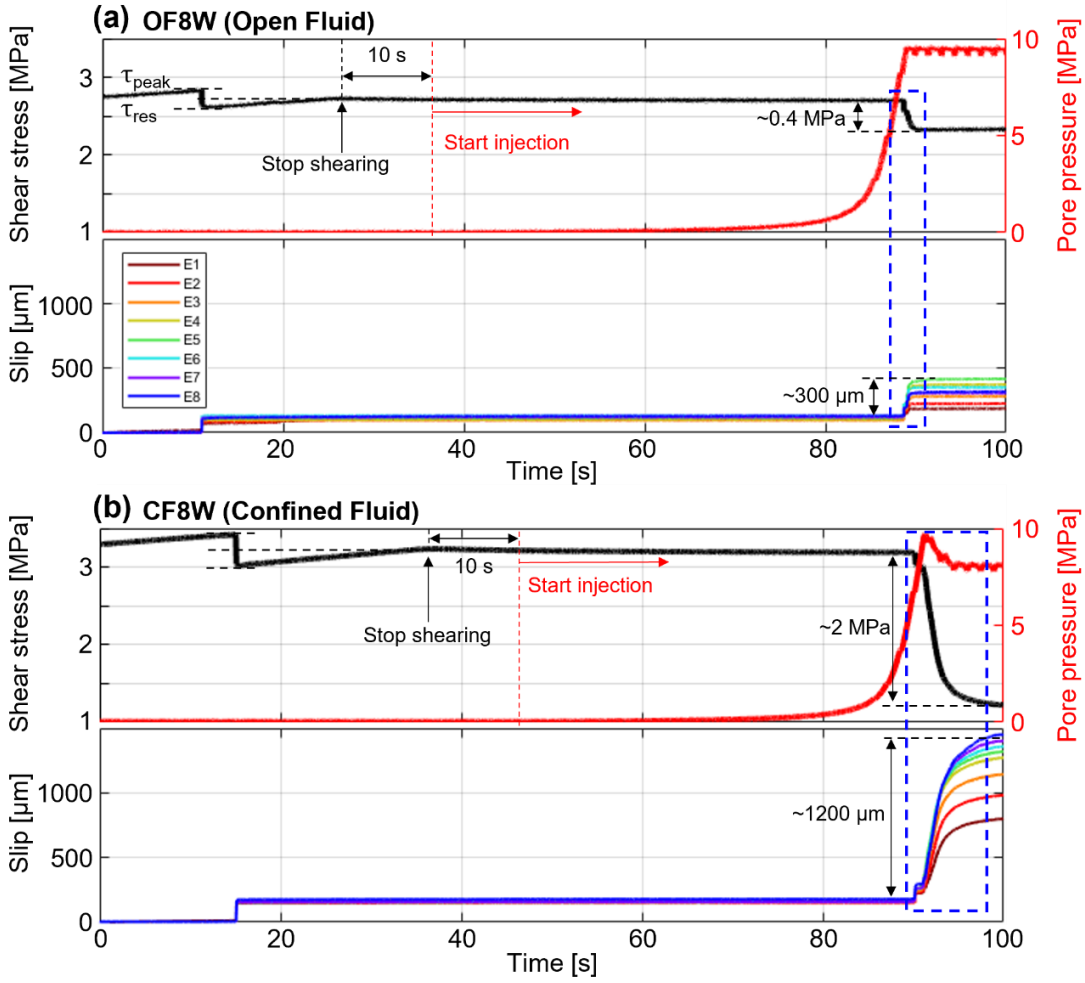

Figure 5.2. Overview of sample-average shear stress, pore pressure at the injection well, and slip behavior of (a) OF8W and (b) CF8W. Shearing ceased when the sample-average shear stress reached a midpoint between the peak shear stress (τ_{peak}) and the residual shear stress (τ_{res}). Fluid injection into the fault began 8 ml/min injection rate, 10 s after stopping shearing in both tests. E1 - E8 are eight eddy current slip sensors with locations shown in Figure 5.1. The region highlighted by the blue dotted area is analyzed in Figure 5.3.

To analyze the seismic slip events induced by fluid injection, Figure 5.3 shows a zoom in of the blue-dotted region in Figure 5.2. Many seismic slip events were so small that no slip was detected with the Eddy current sensors. However, for the larger seismic slip events, we mapped the extent of dynamic slip, defined as where the average the slip rate exceeded 3 mm/s measured using Eddy current sensors within ±0.01 s time

window, surrounding the event. Figures 5.3c and 5.3d show the extent of dynamic slip as black vertical lines. The locations of the hypocenters (circles) and their corresponding magnitudes (indicated by the color within each circle) were determined from piezoelectric sensors (see methods in Section 5.3.4). A representative set of signals from one seismic slip event is shown in Figure 5.3e, with the earliest first arrivals detected near P4 and P5, close to the injection site. Figure 5.3f shows a sequence of two seismic slip events with distinct hypocenters that occurred within a few milliseconds of each other.

In most experiments, a few small-magnitude events occurred near the injection well before the mainshock, defined as the event with the largest magnitude that ruptured the entire fault (Figure 5.3c). The mainshock reduced the sample-average shear stress to τ_{res}. The main focus of this study is the migration of seismicity that occurred after the mainshock. In experiment OF8W, those events remained concentrated near the injection well, indicating that fluid pressurization and weakening were highly localized. In contrast, CF8W exhibited both a larger number of events and a more distributed rupture pattern (Figure 5.3d). The hypocenters propagated bilaterally along the fault. As the hypocenters migrated, dynamic slip occurred both at the hypocenter locations and ahead of them, extending to the ends of the sample but not extending back behind the migrating front of hypocenters.

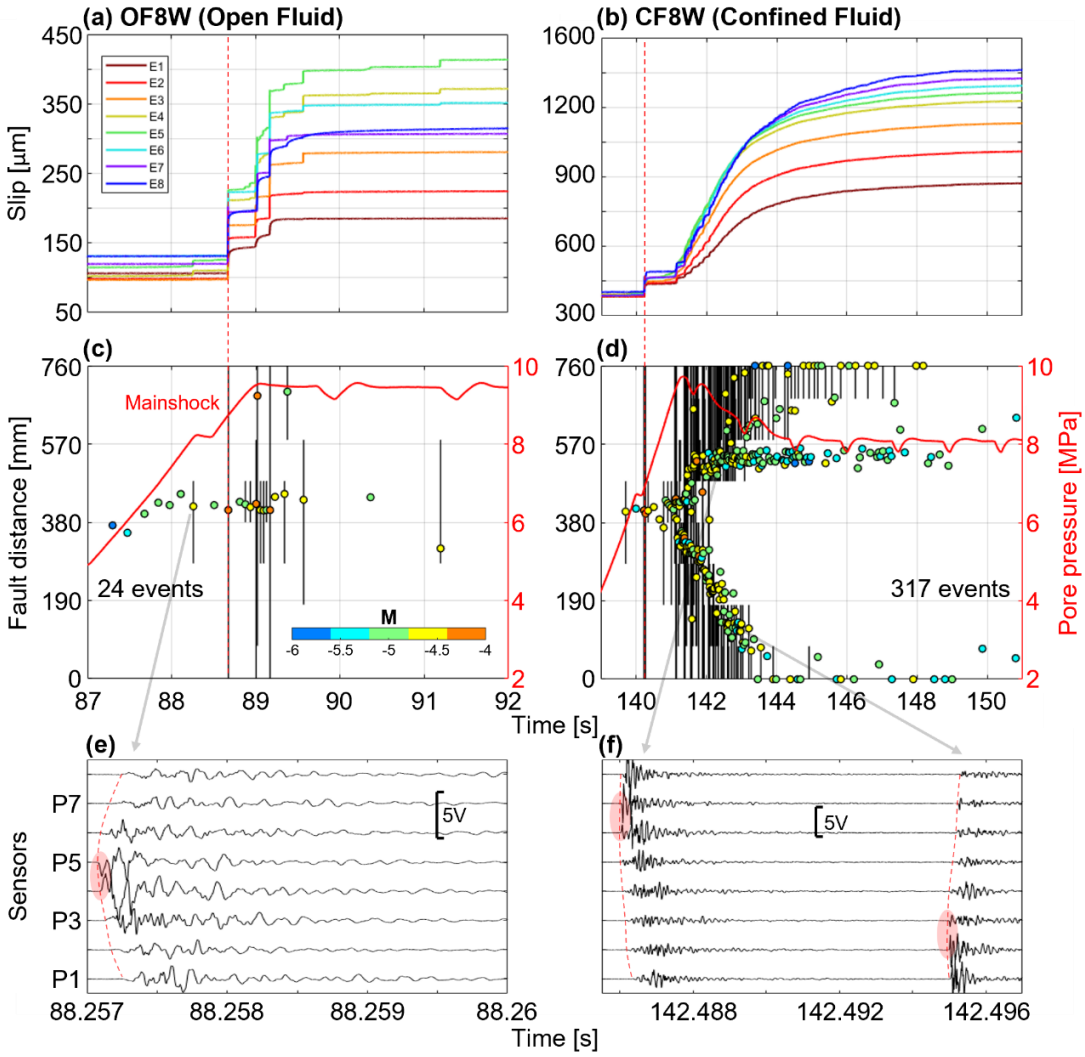

Figure 5.3. Zoomed-in view of the blue dotted region in Figure 5.2, highlighting fluid-induced (a) slip, (c) magnitude and hypocenter of seismicity, and (e) representative signals for OF8W, with (b), (d), and (f) showing the corresponding results for CF8W. Note that the mainshock is defined as the largest magnitude event within these slip sequences. Vertical black lines denote the extent of dynamic slip in c and d.

5.4.2. Effect of injection rate and viscosity

Figure 5.4 shows the effects of fluid injection rate and viscosity on pore pressure and seismicity for confined fault (CF) experiments. Data for other injection conditions is provided in Figure 5.S2. At the fast injection rate (CF16W), the mainshock occurred immediately as the first event with no detectable precursory slip (Figure 5.4b), followed by seismicity that initially clustered near the injection well and then migrated outward (Figure 5.4a). In contrast, the slow injection rate (CF1W) showed multiple small magnitude foreshocks near the well before the mainshock (Figure 5.4c) with ~20 μm of precursory slip along most of the fault (Figure 5.4d). After the mainshock, most events remained clustered near the injection well. Some events occurred farther from the injection site, but no distinct migration was observed.

The injection of more viscous fluid (CF1V) caused a clear outward migration of hypocenters and larger event magnitudes (Figure 5.4e). Despite the slow injection rate, the viscous fluid produced seismic behavior similar to that observed in fast water injection (CF16W). The mainshock resulted in ~300 μm of slip (Figure 5.4f), six times more than in the water injection cases.

Table 5.S1 summarizes the effects of loading rate and fluid viscosity. Higher injection rates of water generally produced more seismic events, larger friction drops, and higher peak pressures, but fewer foreshocks. Slow injection of viscous fluid caused larger friction changes and fewer foreshocks, similar to fast water injection (CF16W), though with fewer total events.

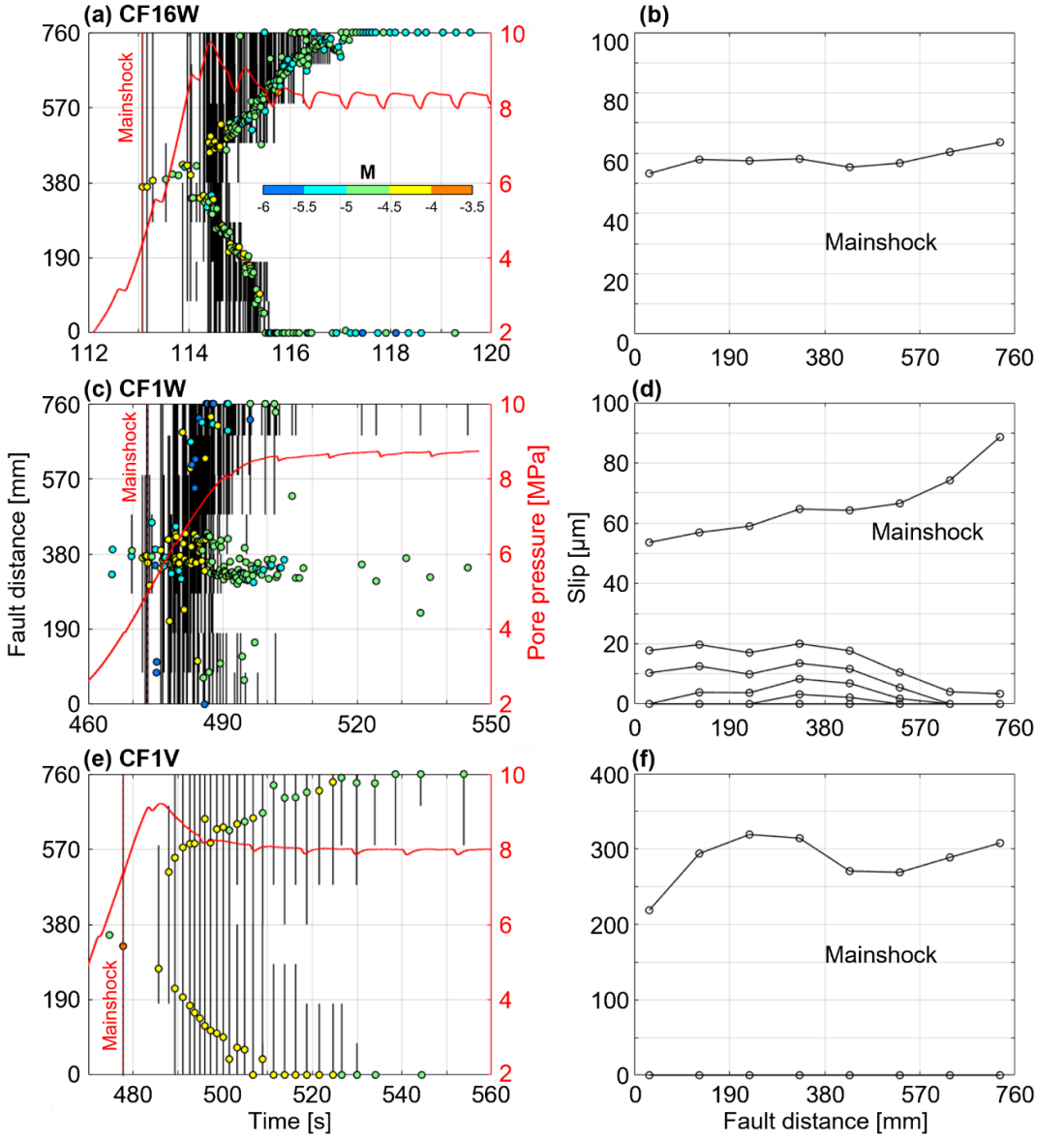

Figure 5.4. Pore pressure at the injection well, along with the magnitude and hypocenter distribution of seismicity for (a) CF16W, (c) CF1W, and (e) CF1V. Cumulative slip prior to the mainshock for (b) CF16W, (d) CF1W, and (f) CF1V.

5.5. Numerical simulation

5.5.1. Model

To better understand the physical mechanisms underlying the seismicity migration, injection-driven fault dynamics were simulated using a poroelastic model implemented in the open-source Finite Element software, Multiphysics Object-Oriented Simulation Environment (MOOSE) (Permann et al., 2020). The simulation was conducted in 2D to represent the experimental fluid injection in the x-y plane where z = 38.1 mm, corresponding to the depth of the injection well (Figure 5.5a). The bulk PMMA blocks were modeled as porous media with very low porosity (10^{-4}) and permeability (10^{-6} D), while the fault was represented by a highly permeable domain of thickness 0.5 mm, in agreement with the experimental set-up. Due to the geometric symmetry of the domain, the simulation was performed on a quarter of the 2D cross-section (Figure 5.5b). The open outflow boundary condition (bottom right of the simulation domain) was implemented via PorousFlowOutflowBC in MOOSE to represent the free flow through the fault outlet. With that modeling approach, fluid at the outflow boundary was removed according to the local flux derived from Darcy's law and the pressure gradient, which varied during the simulation.

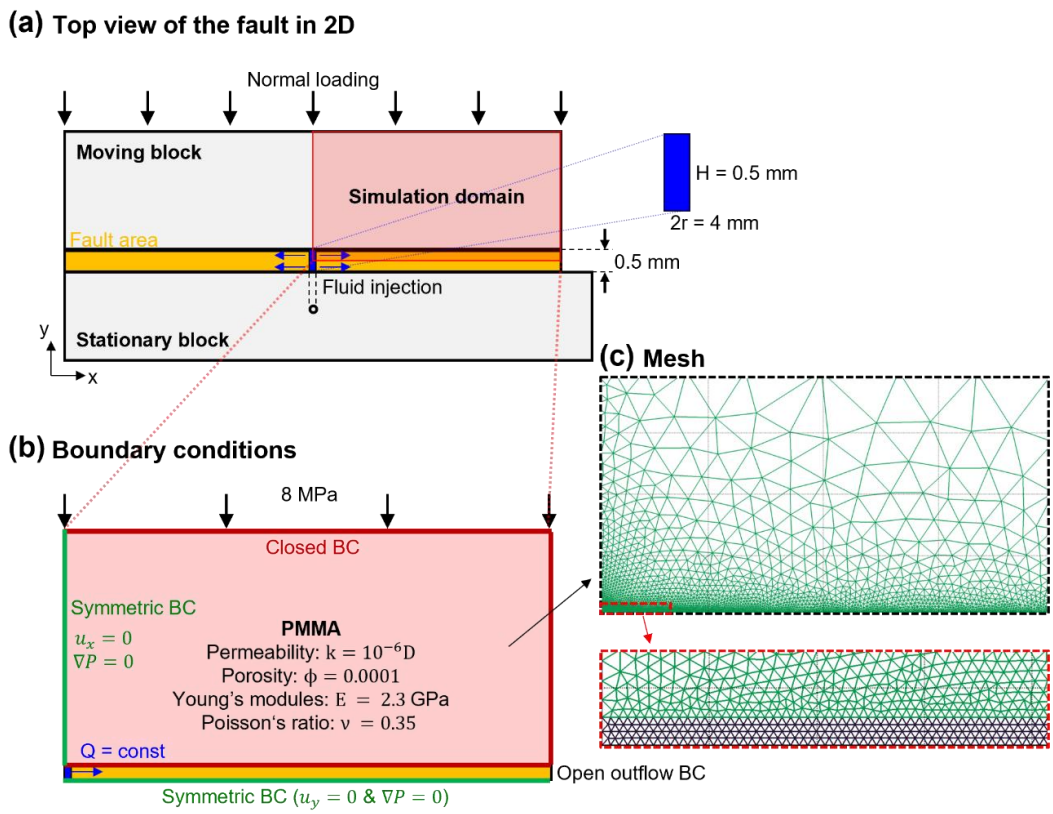

Figure 5.5. (a) 2D simulation domain representing a quarter of the x-y plane at the injection position. (b) Simulation set-up with the boundary conditions (BC) and material properties employed in the numerical model. (c) Mesh adopted in the simulations, with a finer mesh in the fault region.

The PorousFlowFullySaturated action from the PorousFlow module was employed to couple fluid flow and mechanical deformation, according to the following governing equations:

$$\frac{\partial}{\partial t}(\phi\rho) + \phi\rho\nabla\cdot v_s - \nabla\cdot\left(\frac{\rho k}{\mu}\nabla P_f\right) = 0, \tag{5.3}$$

$$-\nabla\cdot\left(\sigma^{eff} - \alpha_B P_f I\right) = 0, \tag{5.4}$$

where ϕ is the porosity (dimensionless), k is the permeability (m^2 or D), ρ is the fluid density (kg/m^3), μ is the fluid dynamic viscosity (Pa·s), v_s is the velocity of the porous solid skeleton (m/s), α_B is the Biot coefficient (dimensionless, 0.8 in this study), P_f is

the fluid pressure (Pa), σ^{eff} denotes effective stress tensor (Pa), and I is identity tensor. Both the bulk PMMA and fault regions were considered as linear elastic porous solids (Figure 5.5a). To represent fault opening without fault lateral deformation, we assigned a Poisson's ratio of 0 to the fault region. The fluid flow in both the fault and the bulk PMMA regions were assumed to follow Darcy's law. Fault aperture was modeled through porosity, which varied with fluid pressure P_f according to the following poroelastic constitutive relationship:

$$\phi = \phi^{ref} + a_P(P_f - P_f^{ref}), \tag{5.5}$$

where the superscript ref refers to a reference state, $a_p = 2\times10^{-7}$ Pa^{-1} to match the time scale of the fault opening dynamics observed experimentally (of the order of seconds). Additionally, we arbitrarily set $\phi^{ref} = 0.005$ to represent an initial fault porosity higher than the porosity of the PMMA blocks and $P_f^{ref} = 0.1$ MPa to set the reference fluid pressure equal to the atmospheric pressure. Fracture aperture can also be viewed as a linear function of fluid pressure, see for example (Ozdemirtas et al., 2009):

$$w = w^{ref} + \frac{1}{K_n}(P_f - P_f^{ref}), \tag{5.6}$$

where w is the fracture aperture, and K_n is the normal stiffness of the fracture. In agreement with the model described in Equation 5.6, in this work, fracture aperture was considered equivalent to porosity.

We assumed that fluid flow within the fault region was governed by the cubic law, such that the flow rate q could be expressed as:

$$q\ [m^2/s] = \frac{w^3}{12\mu}\nabla P_f, \tag{5.7}$$

$$Q\ [m^3/s] = \frac{w^3 L_z}{12\mu}\nabla P = \frac{w^2}{12}\frac{A}{\mu}\nabla P_f, \tag{5.8}$$

in which the area of the cross section of the flow channel is noted $A = w \cdot L_z$, where L_z is the length perpendicular to the 2D domain modeled in the simulations (i.e., z-direction in Figure 5.1). Fault permeability can be seen as a quadratic function of porosity, given that $k_f = w^2/12$. Since we modeled fault opening as a porosity change, fault permeability was expressed as a function of porosity, as:

$$k_f = k_f^{open} \phi^2, \tag{5.9}$$

where k_f^{open} represents the permeability of fault zone when it is fully opened (i.e., $\phi = 1$). In this work, $k_f^{open} = 100$ D was chosen to represent a fault with an opening w of the order of 0.1 mm, and to capture the time scale of the propagation of the fault aperture front observed experimentally. Lastly, the fluid viscosity μ was set as a value of 1 mPa·s for the water and 50 mPa·s for the viscous fluid in agreement with the experiments. The fluid density was modeled as a function of fluid pressure, as follows:

$$\rho = \rho_0 \exp\left(\frac{P_f}{K_b}\right), \tag{5.10}$$

where ρ_0 represents reference fluid density and K_b denotes the fluid bulk modulus.

The initial fluid pressure was set to 0.1 MPa in the entire simulation domain. The fluid was injected into the fault region as shown in Fig. 5a at various injection rates. The injection area is the lateral surface area of the injection cylinder (shown in Figure 5.5a), calculated as $2\pi \cdot r \cdot H = 2\pi \cdot (2\times10^{-3}\ \text{m}) \cdot (0.5\times10^{-3}\ \text{m}) = 2\pi\times10^{-6}\ \text{m}^2$, where r and H are the radius and height of the injection cylinder, respectively. An injection flow rate of 8 ml/min corresponds to injection volume rate per area of $1/(15\ \pi)\ \text{m}^3/\text{m}^2/\text{s}$, which corresponds to 21 $\text{kg/m}^2/\text{s}$ for water. We varied the injection rates from 0.5 $\text{kg/m}^2/\text{s}$ to 20 $\text{kg/m}^2/\text{s}$, corresponding to volumetric injection rates ranging from 0.2 ml/min to

7.6 ml/min. The unit of injection rate is converted to a mass rate per area to match the input requirements of the PorousFlowSink boundary condition in MOOSE.

The mesh in the fault region was finer than in the bulk PMMA blocks, because of the difference of scale between the fault and bulk PMMA block zones (Figure 5.5c). A first-order Lagrange interpolation was adopted for both displacement and pore pressure fields.

5.5.2. Distribution of porosity with different injection rates

To investigate how injection rate of water affects the spatial distribution of porosity in the simulation, we plotted the porosity distribution along the fault distance at similar injected volumes (Figure 5.6). Porosity is a function of pore pressure (Equation 5.5). As pore pressure increases, porosity also increases, enhancing fluid flow within the fault. At the fastest injection rate (7.6 ml/min), porosity is higher and more localized near the injection well (Figure 5.6a). In contrast, at a slower injection rate (0.5 ml/min), the porosity has lower values and is more distributed away from the injection well, even for a similar injected volume (Figure 5.6b). The red dotted line at a porosity of 0.15 represents the critical porosity (ϕ_c) associated with the onset of seismicity, which is discussed in Section 5.6.1.2.

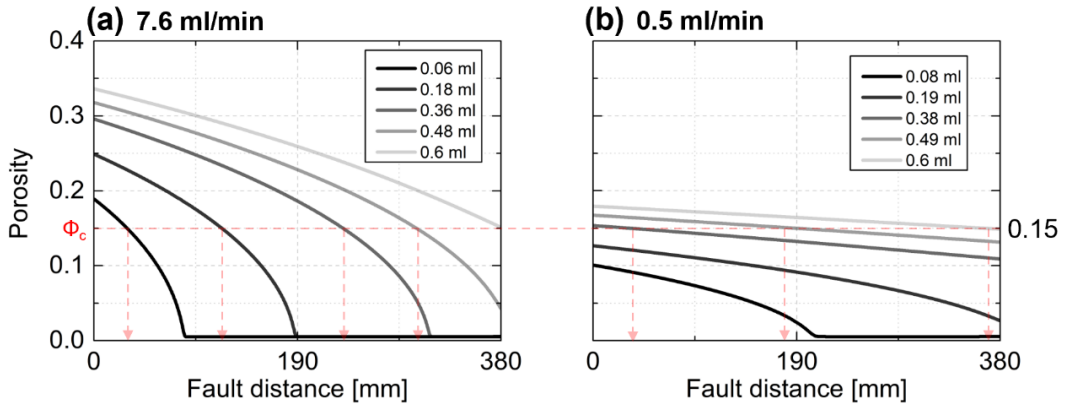

Figure 5.6. Porosity distributions along the fault distance at various injected volumes of water from 0.06 ml to 0.6 ml for (a) 7.6 ml/min injection rate and (b) 0.5 ml/min injection rate. Note that ϕ_c is the critical porosity for the onset of seismicity, detailed in Section 5.6.1.2.

5.6. Discussion

Our experiments demonstrated that fault slip and seismicity patterns during fluid injection were influenced by the presence of confinement, injection rate, and fluid viscosity. The impermeable Teflon-covered fault sections used in the confined fluid (CF) experiments enhanced fault weakening by pressurizing a larger fault area compared to the open fluid (OF) experiments. Higher injection rates (e.g., CF16W) triggered an immediate mainshock without foreshocks, whereas lower rates (e.g., CF1W) led to a mainshock preceded by detectable slow slip and multiple associated foreshocks near the injection well. Viscous fluid injection (e.g., CF1V) produced fewer but larger magnitude seismic events, while less viscous injection (e.g., CF1W) produced a larger number of smaller events. Results of 2D poroelastic simulations showed that at a fast injection rate, porosity increased sharply near the injection well and gradually extended along the fault, while at a slow injection rate, the porosity increase was smaller but more uniformly distributed along the fault.

5.6.1. Seismicity migration mechanisms

To examine the mechanisms driving seismicity migration, we first created a pressure-diffusion model that neglects poroelasticity (Section 5.6.1.1). While this adequately described the seismicity locations for the low injection rate, it could not explain the faster migration observed at higher injection rates and with the more viscous fluid, which we term volume-driven seismicity migration. In contrast, the experimental results could be reproduced with the poroelastic model described in Section 5.5 because the numerical model included fluid volume in its formulation (Section 5.6.1.2).

5.6.1.1. Pressure-diffusion model

We modeled pressure diffusion using the 2D diffusion equation:

$$\frac{\partial P_f}{\partial t} = \alpha\left(\frac{\partial^2 P_f}{\partial x^2} + \frac{\partial^2 P_f}{\partial y^2}\right), \tag{5.11}$$

where t is time, α (= $k_f/(\beta_c \cdot \mu)$) is the hydraulic diffusivity, and β_c is the storage coefficient. Using symmetry, we modeled 2D diffusion using only a quarter of the domain (Figure 5.S3a) and applied Neumann boundary conditions at the Teflon-PMMA interface and Dirichlet boundary conditions (P = 0) at the free surface at the fault end. To determine α, we used a shut-in test where fluid injection was halted at a set pressure (8 MPa, after ~40 s) and the subsequent pressure decrease over time was observed. Our analysis showed that α ranged from 8E-9 to 8E-8 m^2/s (Figure 5.S3b) and no single α value could perfectly match our results, consistent with Cebry and McLaskey (2021), likely due to neglected poroelastic effects (Rutqvist & Stephansson, 2003).

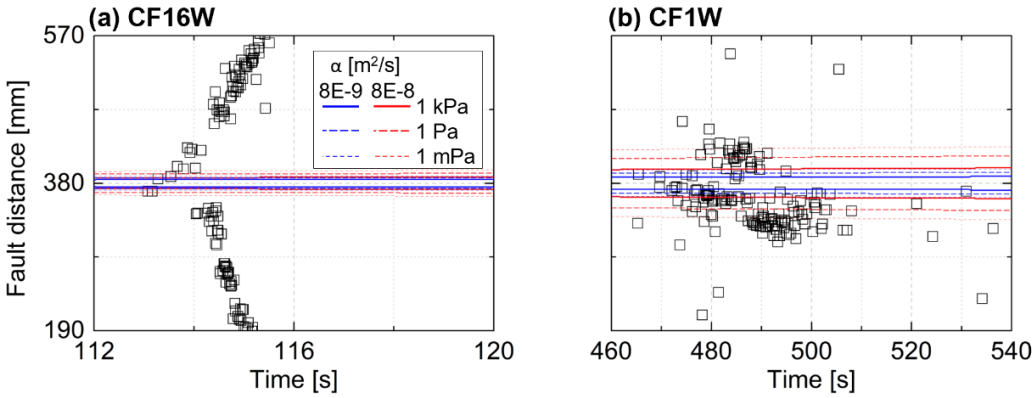

Figure 5.7. Comparison of modeled pressure contours (e.g., 1 mPa, 1 Pa, and 1 kPa) for (a) CF16W and (b) CF1W. Note that pressure diffusion on fault surface is shown in Figures 5.S3c and 5.S3d.

5.6.1.2. Seismicity migration with injected volume

To better understand the mechanism behind the migration of seismicity at fast injection rates that could not be explained by pressure diffusion, Figure 5.8a shows the migration of seismicity hypocenters against injected fluid volume rather than time. The injected volume was calculated by multiplying the time and the injection rate, and the x-axis was shifted to align migration trends for comparison. When normalized this way, the propagation of seismicity in CF1V and CF16W experiments exhibit similar behavior, suggesting that injected volume played a key role. However, in CF1W, pressure appeared to be the dominant control (Figure 5.7b) instead of injected volume.

To reproduce seismicity migration from the numerical simulations described in Section 5.5, we assumed that seismic slip events occur when the Coulomb failure criterion is reached:

$$\tau \geq \tau_{static} = \mu_{PMMA} * (\sigma_N - P_f), \quad (5.12)$$

where τ is the applied shear stress (set to 3.1 MPa for these experiments, see Figure 5.2b), σ_N is the applied normal stress (8 MPa), and μ_{PMMA} is the static friction

coefficient of PMMA, which is a tunable parameter to match with experimental results. Setting an assumed value for μ_{PMMA} produces a critical pore pressure, which corresponds to a critical value of porosity. The location of this critical porosity, ϕ_c, changes with injection volume (red dotted arrows in Figure 5.6a) and its migration was used to simulate a migration of seismicity. Through trial and error, we found that $\phi_c = 0.15$ matched the experimental results. That is, when normalized by injected volume, all seismicity migration patterns collapsed to a similar form except for experiments where low-viscosity fluid was injected at a low rate (e.g., 0.5 ml/min or 0.9 ml/min injection rates) (Figure 5.8b).

This $\phi_c = 0.15$ corresponds to a critical pressure $P_f = 0.8$ MPa (Equation 5.5). Combining this with the experimentally observed values of σ_N and τ, Equation 5.12 yields a value of $\mu_{PMMA} = 0.43$. This falls within the previously reported range of PMMA friction coefficients, from 0.38 to 0.6 (McLaskey et al., 2012; Paglialunga et al., 2023; Wu et al., 2023).

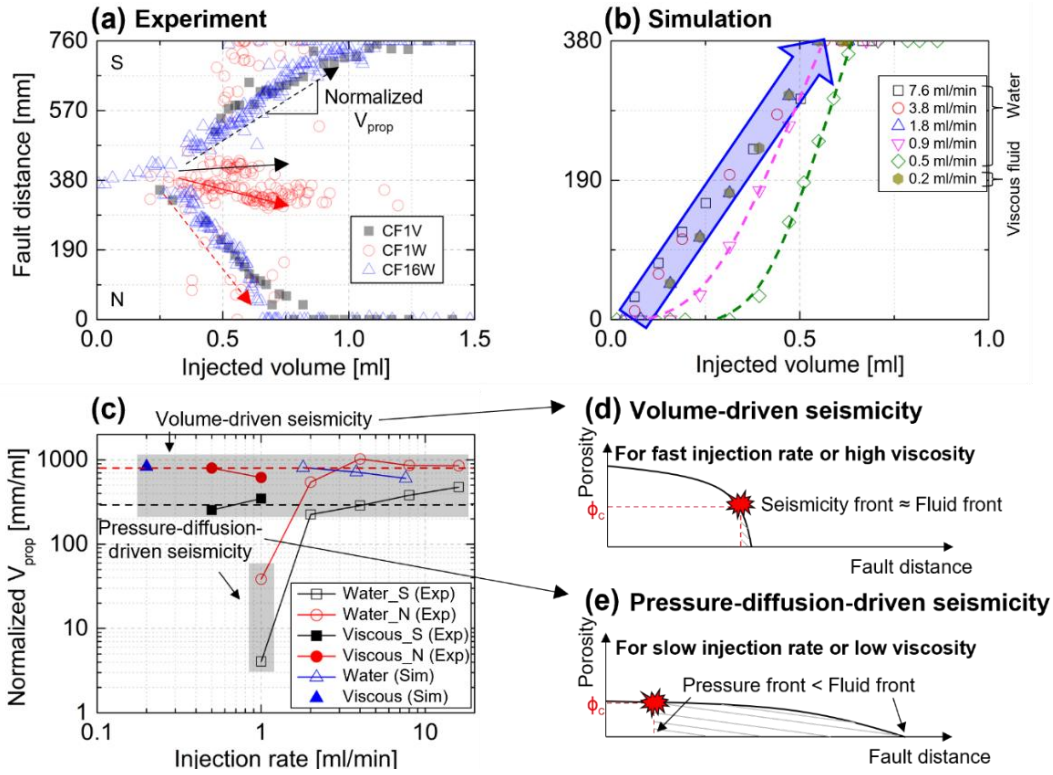

Figure 5.8. (a) Migration of hypocenters as a function of injected volume in the experiment. Note that the graph has been shifted in x-direction to align the trends for comparison. Normalized V_{prop} is defined as the fault distance divided by the injected volume. (b) Seismicity migration as a function of injected volume in the simulation. Note that each data point for fault distance corresponded to the location where the porosity distribution intersected the critical porosity. (c) Propagation velocity normalized by the injected volume of all CF fault conditions for experiment and simulation. Schematic porosity distributions for (d) volume-driven seismicity and (e) pressure-diffusion-driven seismicity (similar to Figure 5.6). Note that the hashed area represents the delay in injected fluid volume between the seismicity front and fluid front.

5.6.1.3. Pressure-Diffusion-Driven versus Volume-Driven Seismicity Migration

To systematically study seismicity migration, Figure 5.8c shows the normalized propagation velocity (V_{prop}) versus injection rate under CF fault conditions, where the velocity was calculated as the slope of fault distance versus injected volume using linear fitting (Figure 5.8a). Two symbols are shown at each injection rate because seismicity migrates bilaterally and one symbol is for the N-propagating front and the

other is from the S-propagating front. In nearly all the experiments, the normalized propagation velocities ranged between ~300 mm/ml and ~800 mm/ml (black and red symbols). The velocity derived from the numerical simulation was ~700 mm/ml (blue symbol), well aligned with the experimental results.

In the volume-driven seismicity migration, illustrated in Figure 5.8d, fluid pressure remains concentrated near the injection point due to limited diffusion, which is characteristic of scenarios involving fast injection rate or high-viscosity fluid. The fluid pressure pushes open the fault which increases the permeability of the fault zone and enhances fluid flow. The pressure-diffusion model that lacks this poroelastic effect fails to reproduce the migration of seismicity observed experimentally (Section 5.6.1.1). Meanwhile, the seismicity front in the volume-driven pattern approximately matches the fluid front because of the high value and large gradient of porosity and fluid pressure. In contrast, experiment CF1W and simulations with slow injection rates and low-viscosity fluid can be described by pressure-diffusion-driven seismicity. In that regime, there is a large spatial separation between the seismicity front and the fluid front, depicted by the gray hashed region in Figure 5.8e.

To further verify that the migrating seismicity closely matched the expanding fluid front, we ran an additional CF1V experiment where the fault was initially dry. The fault was pre-wetted in all previously reported experiments to ensure saturated conditions before testing; however, through the use of a dry fault, we could visually track the fluid front through the transparent PMMA (Figure 5.A1). Using this method, it was confirmed that the hypocenters of the seismicity generally aligned with the locations of the fluid fronts.

5.6.1.4. Comparison to previous work

The pressure-diffusion model cannot fully explain the volume-driven seismicity in this study. Instead, a poroelastic model that allows permeability to increase with increasing fluid pressure was needed to reproduce the seismicity migration. Yang et al. (2023) used a 2D anti-plane numerical model to confirm a direct link between the injection rate and the speed of stress transfer. They investigated the stress transfer front speed (0.01 MPa pressure contour) at high injection rates (from 3×10^5 ml/min to 6×10^6 ml/min), considering a fault opening of w = 1 m in the y-direction and a fault depth of d = 1 km in the z-direction (Figure 5.1c), Within this range of injection rates, the normalized stress transfer front speed remained ~10^{-3} mm/ml. This is consistent with previous numerical simulation results showing that the slip front migration speed is proportional to the injection rate (Dublanchet, 2019; Garagash, 2021). However, at a low injection rate (1.2×10^5 ml/min), the normalized stress transfer front speed, governed by pressure diffusion, dropped to ~10^{-4} mm/ml. Despite the similarity in migration mechanism to our experiments, the boundary injection rate between volume-driven and pressure-diffusion-driven regimes in Yang et al. (2023) is ~10^5 times higher (~2×10^5 ml/min) than in our experiments (~1.5 ml/min; Figure 5.8c). This difference arises from the reservoir capacity per unit fault length: w·d is 1000 m^2 in Yang et al. (2023), whereas in our experiment, w·d is only 2.5×10^{-5} m^2 (w = 0.05 m and d = 0.0005 m; Figures 5.1c and 5.5a). Furthermore, Yang et al. (2023) found that fluid injection-induced pore pressure triggered aseismic slip, which transferred stress to distant locked faults, causing rupture without permeability changes with pore pressure. However, the poroelastic model in this study accounts for permeability

changes with pore pressure, which also affects the boundary injection rate. Finally, differences in initial model settings, such as the shear modulus of the block (0.85 GPa in this study and 32.4 GPa in Yang et al., 2023), can affect the boundary injection rate. Nevertheless, volume-driven migration of stress or seismicity is commonly observed in both stress transfer and poroelastic models.

5.6.2. The effect of fluid viscosity on seismicity

While fluid viscosity affects the transition between volume-driven and pressure-diffusion-driven seismicity regimes, it also appeared to affect the seismicity that was generated. Viscous fluid produced fewer seismic events, but larger magnitude events compared to water. A related observation is that with water injection, dynamic slip typically propagated from seismic hypocenters outward away from the injection well with notably no dynamic slip in regions close to the well that were already highly pressurized (Figures 5.4a and 5.4c). In contrast, under viscous fluid injection, dynamic slip also propagated back into the region near the injection well (Figure 5.4e) despite the fact that it was highly pressurized there. This observation might be explained by Cornelio and Violay (2020) who found that as fluid viscosity increased, the (a-b) parameter from the rate-and-state friction law decreased, transitioning from positive (i.e., velocity-strengthening) to negative values (i.e., velocity-weakening). This is because high-viscosity fluid leads to boundary lubrication condition, where thin fluid films coexist with solid-solid contact. This regime is highly sensitive to slip rate changes, enhancing velocity-weakening behavior as the system becomes more prone to frictional instability. Also, they found that water promoted dilation of the fault

during fault slip, while viscous fluid promoted compaction, which increased pore pressure locally and reduced effective normal stress. This compaction destabilized the fault and contributed to be velocity-weakening behavior. Therefore, under viscous fluid injection, even fluid-pressurized regions adjacent to the well could experience dynamic slip, and this could be the cause of the larger magnitude events.

5.6.3. High permeable pathways by Teflon tape

This study showed that the Teflon technique effectively prevented fluid leakage and expanded the potential applications of fluid-injection experiments in large samples that are not confined within a pressure vessel. However, the Teflon tape used in this study has a thickness of ~tens of microns, which created a highly permeable pathway along the edge of the bare PMMA fault surface adjacent to the Teflon-covered area. This increase in permeability near the edge of the Teflon can be visualized in Figure 5.A1 where the fluid front travels fastest near the Teflon and slower in the interior of the bare PMMA region. The higher permeability pathway near the edge of the Teflon region is the likely reason for the drop in fluid pressure from 10 MPa to 8 MPa shown in Figure 5.2b but not present in Figure 5.2a. This heterogeneous permeability distribution was not incorporated into numerical simulations.

5.7. Conclusions

In this work, we investigated shear fault reactivation by directly injecting fluid into a PMMA fault (760 mm long, 76 mm high) formed from the interface between two separate blocks. To prevent leakage due to a free surface at a short distance from the

injection location, we coated the section of the fault close to the free surface with Teflon tape. The enhanced weakening of the fault compared to cases without the Teflon showed that the Teflon barriers were effective at confining the fluid and enabling pressurization over a larger fault area. This Teflon confinement technique allows for more versatility in large-scale laboratory fluid injection experiments.

By varying the fluid injection rate and viscosity, two distinct migration mechanisms were observed. At slow injection rate or with low-viscosity fluid (water), seismicity slowly migrated from the injection point, termed pressure-diffusion-driven seismicity since the seismicity front followed a pressure-diffusion model. In contrast, at fast injection rate or with high-viscosity fluid, the seismicity front migrated much more rapidly, with migration rate proportional to the injected fluid volume. This migration behavior is referred to as volume-driven seismicity in this work.

A 2D poroelastic numerical model was developed, incorporating pressure-dependent permeability within the fault zone. This model reproduced the experimentally observed seismicity migration patterns by assuming that seismic events initiate when and where fluid pressure, linked to porosity (Equation 5.5), reaches a critical threshold. When the experimentally applied stress levels were added to the critical fluid pressure threshold, it suggested a friction coefficient $\mu_{PMMA} = 0.43$, aligning with previously published estimates.

Overall, this study demonstrates that the migration of seismic events can be governed by either pressure diffusion or the injected volume, with the controlling mechanism determined by the injection rate, fluid viscosity, and poroelastic parameters. The volume-driven seismicity migration regime identified in this study is likely important

for cases of fast injection into low permeability formations, which are conditions similar to hydraulic fracture operations for subsurface hydrocarbon operations or stimulation phases associated with enhanced geothermal systems in tight formations.

5.8. Appendix

We conducted fluid injection under dry fault conditions, following the same procedure as in CF1V. A camera positioned beneath the fault captured high-resolution images (2640 × 1080 pixels) at 310 s, 355 s, and 370 s to compare fluid migration with seismic hypocenters. In the PMMA region, the fluid spreads out in a circular pattern (Figure 5.A1a). Upon reaching the boundary between the Teflon-covered and bare PMMA areas, the fluid advances more rapidly along the boundary than within the PMMA fault regions (Figures 5.A1b and 5.A1c). The fluid reaches the top faster than the bottom, leading to asymmetric migration. The fluid migration region, roughly outlined in red circle, is compared with seismic hypocenters (Figures 5.A1d and 5.A1e). This result indicates that the fluid front directly influences fault seismicity in volume-driven regimes (see Section 5.6.1.2). While many hypocenters align with fluid locations, some originate from the far end of the fault, beyond the fluid. This suggests that seismic triggering is not solely due to direct fluid injection but also influenced by other mechanisms. This may be due to stress concentration at the fault ends caused by the cessation of a previous rupture.

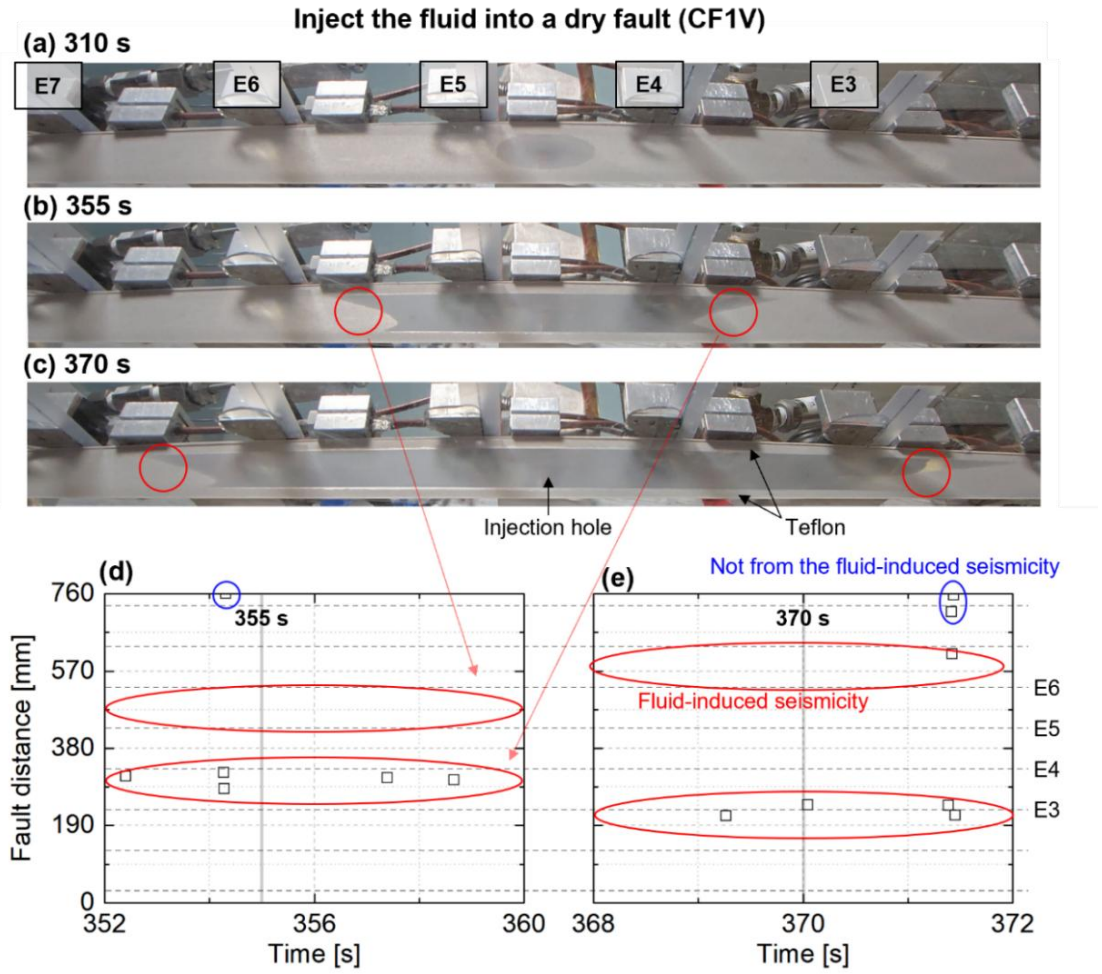

Figure 5.A1. Fluid migration of CF1V under dry fault conditions at (a) 310 s, (b) 355 s, and (c) 370 s, with corresponding seismicity at (d) 355 s and (e) 370 s.

5.9. Supplementary Figures

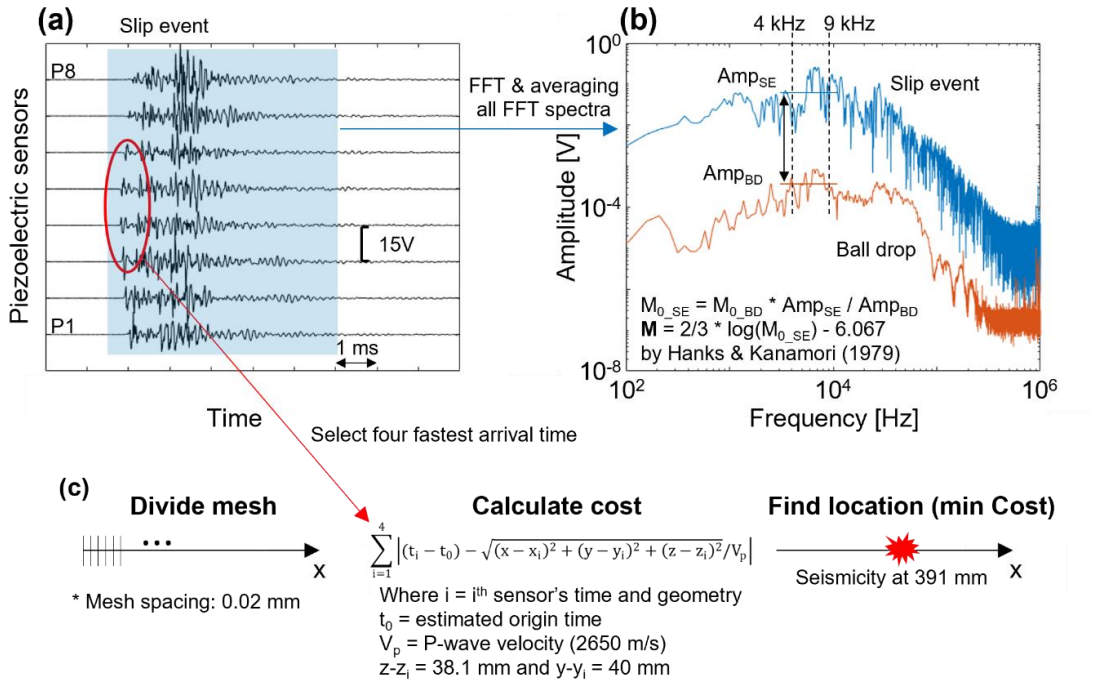

Figure 5.S1. (a) Representative signals from the slip event in time domain and (b) averaged frequency-domain spectra (via FFT) for both the ball drop and slip event. (c) Process for determining the seismic event location in one-dimensional analysis: divide the mesh for calculation, compute the cost function at each mesh point, and identify the minimum cost, which corresponds to the seismic event location. Note that the four fastest arrival signals were used for the cost calculation.

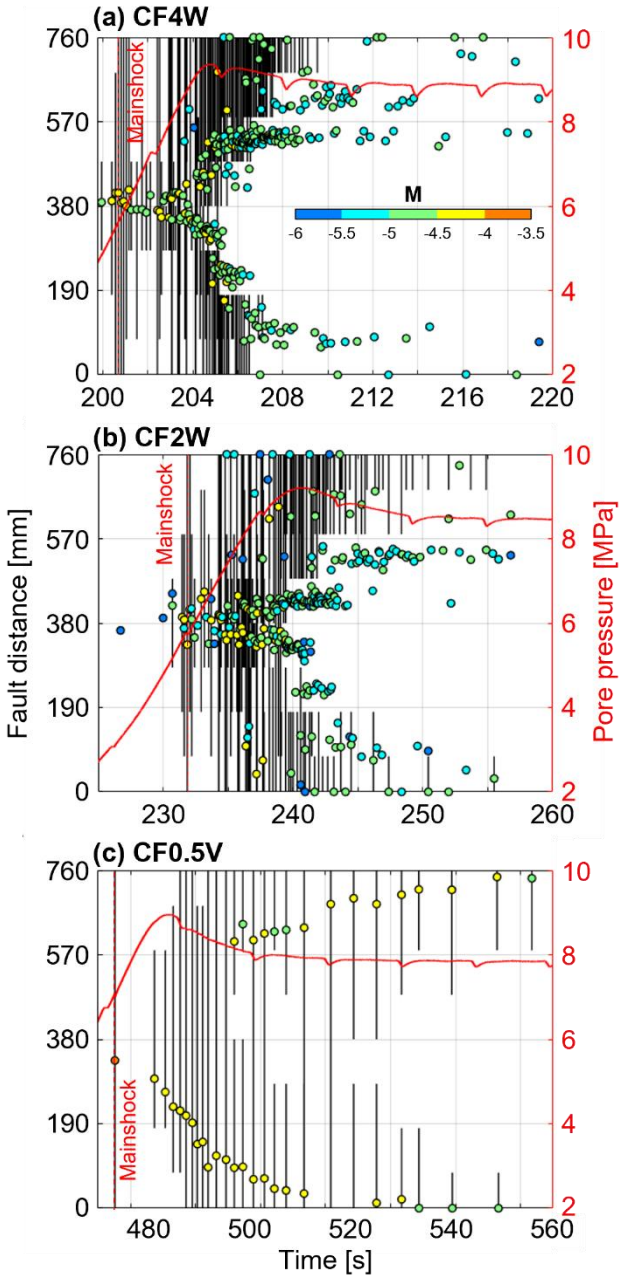

Figure 5.S2. Pore pressure at the injection well, along with the magnitude and hypocenter distribution of seismicity for (a) CF4W, (b) CF2W, and (c) CF0.5V.

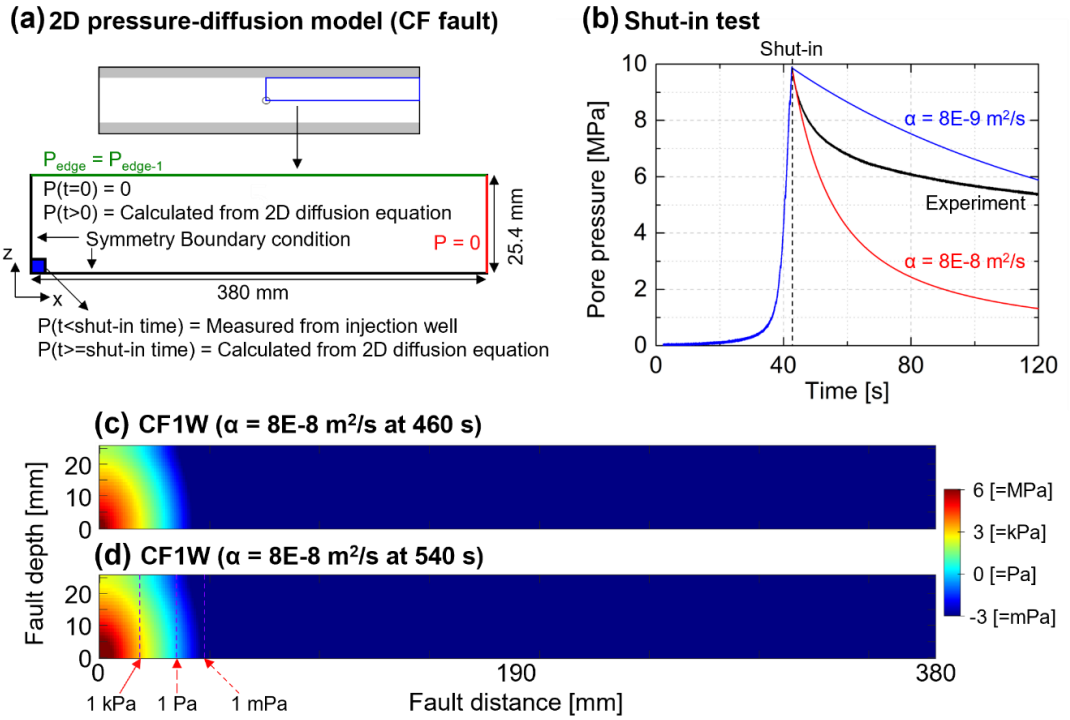

Figure 5.S3. (a) Schematic 2D pressure diffusion model with boundary conditions. (b) Shut-in test to obtain the range of the hydraulic diffusion coefficient in CF fault condition. Note that water injection continued until ~40 s before being stopped. Pressure distribution with distance for CF1W using water for α = 8e-8 m^2/s at (c) 460 s and (d) 540 s. Note that the color scale represents pressure on a logarithmic scale.

5.10. Supplementary Table

Table 5.S1. Mechanical properties with different loading rates and viscosities. Note that friction coefficient is the ratio of sample-average shear and normal stresses.

Exp	Total events [Count]	Foreshocks [Count]	Peak fluid pressure [MPa]	Change of friction coefficient
CF16W	274	0	9.7	0.25
CF8W	317	2	9.7	0.24
CF4W	314	3	9.4	0.23
CF2W	288	7	9.2	0.22
CF1W	190	7	8.6	0.19
CF1V	53	1	9.2	0.21
CF0.5V	39	0	9.0	0.15

REFERENCES

Atkinson, G. M., Eaton, D. W., Ghofrani, H., Walker, D., Cheadle, B., Schultz, R., et al. (2016). Hydraulic Fracturing and Seismicity in the Western Canada Sedimentary Basin. *Seismological Research Letters*, *87*(3), 631–647. https://doi.org/10.1785/0220150263

Bao, X., & Eaton, D. W. (2016). Fault activation by hydraulic fracturing in western Canada. *Science*, *354*(6318), 1406–1409. https://doi.org/10.1126/science.aag2583

Barbour, A. J., Norbeck, J. H., & Rubinstein, J. L. (2017). The effects of varying injection rates in osage county, Oklahoma, on the 2016 Mw 5.8 Pawnee Earthquake. *Seismological Research Letters*, *88*(4), 1040–1053. https://doi.org/10.1785/0220170003

Bhattacharya, P., & Viesca, R. C. (2019). Fluid-induced aseismic fault slip outpaces pore-fluid migration. *Science*, *364*(6439), 464–468. https://doi.org/10.1126/science.aaw7354

Cappa, F., Scuderi, M. M., Collettini, C., Guglielmi, Y., & Avouac, J. P. (2019). Stabilization of fault slip by fluid injection in the laboratory and in situ. *Science Advances*, *5*(3), 1–8. https://doi.org/10.1126/sciadv.aau4065

Cebry, S. B. L., & McLaskey, G. C. (2021). Seismic swarms produced by rapid fluid injection into a low permeability laboratory fault. *Earth and Planetary Science Letters*, *557*, 116726. https://doi.org/10.1016/j.epsl.2020.116726

Cebry, S. B. L., & McLaskey, G. C. (2024). Heterogeneous high frequency seismic radiation from complex ruptures. *Seismica*, *3*(2). https://doi.org/10.26443/seismica.v3i2.1351

Cebry, S. B. L., Ke, C. Y., & McLaskey, G. C. (2022). The Role of Background Stress State in Fluid-Induced Aseismic Slip and Dynamic Rupture on a 3-m Laboratory Fault. *Journal of Geophysical Research: Solid Earth*, *127*(8), 1–19. https://doi.org/10.1029/2022JB024371

Chang, K. W., & Segall, P. (2016). Injection-induced seismicity on basement faults including poroelastic stressing. *Journal of Geophysical Research: Solid Earth*, *121*(4), 2708–2726. https://doi.org/10.1002/2015JB012561

Cochard, T., Svetlizky, I., Albertini, G., Viesca, R. C., Rubinstein, S. M., Spaepen, F., et al. (2024). Propagation of extended fractures by local nucleation and rapid transverse expansion of crack-front distortion. *Nature Physics*, *20*(4), 660–665. https://doi.org/10.1038/s41567-023-02365-0

Cornelio, C., & Violay, M. (2020). Effect of Fluid Viscosity on Earthquake Nucleation. *Geophysical Research Letters*, *47*(12), 1–9. https://doi.org/10.1029/2020GL087854

Dublanchet, P. (2019). Fluid driven shear cracks on a strengthening rate-and-state frictional fault. *Journal of the Mechanics and Physics of Solids*, *132*, 103672. https://doi.org/10.1016/j.jmps.2019.07.015

Eaton, D. W. (2018). *Passive Seismic Monitoring of Induced Seismicity*. Cambridge University Press. https://doi.org/10.1017/9781316535547

Eaton, D. W., Igonin, N., Poulin, A., Weir, R., Zhang, H., Pellegrino, S., & Rodriguez, G. (2018). Induced Seismicity Characterization during Hydraulic-Fracture Monitoring with a Shallow-Wellbore Geophone Array and Broadband Sensors. *Seismological Research Letters*, *89*(5), 1641–1651. https://doi.org/10.1785/0220180055

Ellsworth, W. L. (2013). Injection-Induced Earthquakes. *Science*, *341*(6142), 1–7. https://doi.org/10.1126/science.1225942

Fasola, S. L., Brudzinski, M. R., Skoumal, R. J., Langenkamp, T., Currie, B. S., & Smart, K. J. (2019). Hydraulic Fracture Injection Strategy Influences the Probability of Earthquakes in the Eagle Ford Shale Play of South Texas. *Geophysical Research Letters*, *46*(22), 12958–12967. https://doi.org/10.1029/2019GL085167

Garagash, D. I. (2021). Fracture mechanics of rate-and-state faults and fluid injection induced slip. *Philosophical Transactions of the Royal Society A: Mathematical, Physical and Engineering Sciences*, *379*(2196), 20200129. https://doi.org/10.1098/rsta.2020.0129

Gori, M., Rubino, V., Rosakis, A. J., & Lapusta, N. (2021). Dynamic rupture initiation and propagation in a fluid-injection laboratory setup with diagnostics across multiple temporal scales. *Proceedings of the National Academy of Sciences*, *118*(51). https://doi.org/10.1073/pnas.2023433118

Grigoli, F., Cesca, S., Rinaldi, A. P., Manconi, A., López-Comino, J. A., Clinton, J. F., et al. (2018). The November 2017 M w 5.5 Pohang earthquake: A possible case of induced seismicity in South Korea. *Science*, *360*(6392), 1003–1006. https://doi.org/10.1126/science.aat2010

Guglielmi, Y., Cappa, F., Avouac, J. P., Henry, P., & Elsworth, D. (2015). Seismicity triggered by fluid injection-induced aseismic slip. *Science*, *348*(6240), 1224–1226. https://doi.org/10.1126/science.aab0476

Ha, S. J., Choo, J., & Yun, T. S. (2018). Liquid CO2 Fracturing: Effect of Fluid Permeation on the Breakdown Pressure and Cracking Behavior. *Rock Mechanics*

and Rock Engineering, *51*(11), 3407–3420. https://doi.org/10.1007/s00603-018-1542-x

Hanks, T. C., & Kanamori, H. (1979). A moment magnitude scale. *Journal of Geophysical Research B: Solid Earth*, *84*(B5), 2348–2350. https://doi.org/10.1029/JB084iB05p02348

Holland, A. A. (2013). Earthquakes Triggered by Hydraulic Fracturing in South-Central Oklahoma. *Bulletin of the Seismological Society of America*, *103*(3), 1784–1792. https://doi.org/10.1785/0120120109

Ishida, T., Chen, Q., Mizuta, Y., & Roegiers, J.-C. (2004). Influence of Fluid Viscosity on the Hydraulic Fracturing Mechanism. *Journal of Energy Resources Technology*, *126*(3), 190–200. https://doi.org/10.1115/1.1791651

Jaeger, J. C., Cook, N. G. W., & Zimmerman, R. (2009). *Fundamentals of Rock Mechanics*. John Wiley & Sons.

Ji, Y., Wang, L., Hofmann, H., Kwiatek, G., & Dresen, G. (2022). High-Rate Fluid Injection Reduces the Nucleation Length of Laboratory Earthquakes on Critically Stressed Faults in Granite. *Geophysical Research Letters*, *49*(23), 1–13. https://doi.org/10.1029/2022GL100418

Kanamori, H., & Brodsky, E. E. (2004). The physics of earthquakes. *Reports on Progress in Physics*, *67*(8), 1429–1496. https://doi.org/10.1088/0034-4885/67/8/R03

Keranen, K. M., Weingarten, M., Abers, G. A., Bekins, B. A., & Ge, S. (2014). Sharp increase in central Oklahoma seismicity since 2008 induced by massive wastewater injection. *Science*, *345*(6195), 448–451. https://doi.org/10.1126/science.1255802

Liu, P., Ju, Y., Gao, F., Ranjith, P. G., & Zhang, Q. (2018). CT Identification and Fractal Characterization of 3-D Propagation and Distribution of Hydrofracturing Cracks in Low-Permeability Heterogeneous Rocks. *Journal of Geophysical Research: Solid Earth*, *123*(3), 2156–2173. https://doi.org/10.1002/2017JB015048

Lockner, D. A. (1995). Rock Failure. In *A handbook of physical constants* (pp. 127–147). https://doi.org/10.1029/RF003p0127

Lockner, D. A., & Byerlee, J. D. (1977). Hydrofracture in Weber Sandstone at high confining pressure and differential stress. *Journal of Geophysical Research*, *82*(14), 2018–2026. https://doi.org/10.1029/JB082i014p02018

Majer, E. L., Baria, R., Stark, M., Oates, S., Bommer, J., Smith, B., & Asanuma, H. (2007). Induced seismicity associated with Enhanced Geothermal Systems.

Geothermics, *36*(3), 185–222. https://doi.org/10.1016/j.geothermics.2007.03.003

Maxwell, S. (2014). *Microseismic Imaging of Hydraulic Fracturing*. Society of Exploration Geophysicists. https://doi.org/10.1190/1.9781560803164

Mclaskey, G. C., & Yamashita, F. (2017). Slow and fast ruptures on a laboratory fault controlled by loading characteristics. *Journal of Geophysical Research: Solid Earth*, *122*(5), 3719–3738. https://doi.org/10.1002/2016JB013681

McLaskey, G. C., Thomas, A. M., Glaser, S. D., & Nadeau, R. M. (2012). Fault healing promotes high-frequency earthquakes in laboratory experiments and on natural faults. *Nature*, *491*(7422), 101–104. https://doi.org/10.1038/nature11512

McLaskey, G. C., Lockner, D. A., Kilgore, B. D., & Beeler, N. M. (2015). A Robust Calibration Technique for Acoustic Emission Systems Based on Momentum Transfer from a Ball Drop. *Bulletin of the Seismological Society of America*, *105*(1), 257–271. https://doi.org/10.1785/0120140170

Mukuhira, Y., Dinske, C., Asanuma, H., Ito, T., & Häring, M. O. (2017). Pore pressure behavior at the shut-in phase and causality of large induced seismicity at Basel, Switzerland. *Journal of Geophysical Research: Solid Earth*, *122*(1), 411–435. https://doi.org/10.1002/2016JB013338

Ozdemirtas, M., Babadagli, T., & Kuru, E. (2009). Experimental and Numerical Investigations of Borehole Ballooning in Rough Fractures. *SPE Drilling & Completion*, *24*(02), 256–265. https://doi.org/10.2118/110121-PA

Paglialunga, F., Passelègue, F., Latour, S., Gounon, A., & Violay, M. (2023). Influence of Viscous Lubricant on Nucleation and Propagation of Frictional Ruptures. *Journal of Geophysical Research: Solid Earth*, *128*(4), 1–16. https://doi.org/10.1029/2022JB026090

Parotidis, M., Shapiro, S. A., & Rothert, E. (2004). Back front of seismicity induced after termination of borehole fluid injection. *Geophysical Research Letters*, *31*(2), 1–5. https://doi.org/10.1029/2003GL018987

Patel, S. M., Sondergeld, C. H., & Rai, C. S. (2017). Laboratory studies of hydraulic fracturing by cyclic injection. *International Journal of Rock Mechanics and Mining Sciences*, *95*(August 2016), 8–15. https://doi.org/10.1016/j.ijrmms.2017.03.008

Permann, C. J., Gaston, D. R., Andrš, D., Carlsen, R. W., Kong, F., Lindsay, A. D., et al. (2020). MOOSE: Enabling massively parallel multiphysics simulation. *SoftwareX*, *11*, 100430. https://doi.org/10.1016/j.softx.2020.100430

Rutqvist, J., & Stephansson, O. (2003). The role of hydromechanical coupling in fractured rock engineering. *Hydrogeology Journal*, *11*(1), 7–40.

https://doi.org/10.1007/s10040-002-0241-5

Scholz, C. H. (2002). *The Mechanics of Earthquakes and Faulting*. Cambridge University Press. https://doi.org/10.1017/CBO9780511818516

Schultz, R., Skoumal, R. J., Brudzinski, M. R., Eaton, D., Baptie, B., & Ellsworth, W. (2020). Hydraulic Fracturing-Induced Seismicity. *Reviews of Geophysics*, *58*(3), 1–43. https://doi.org/10.1029/2019RG000695

Shapiro, S. A., Huenges, E., & Borm, G. (1997). Estimating the crust permeability from fluid-injection-induced seismic emission at the KTB site. *Geophysical Journal International*, *131*(2), F15–F18. https://doi.org/10.1111/j.1365-246X.1997.tb01215.x

Shapiro, S. A., Rothert, E., Rath, V., & Rindschwentner, J. (2002). Characterization of fluid transport properties of reservoirs using induced microseismicity. *Geophysics*, *67*(1), 212–220. https://doi.org/10.1190/1.1451597

Song, J. Y., & McLaskey, G. C. (2024). Laboratory Earthquake Ruptures Contained by Velocity Strengthening Fault Patches. *Journal of Geophysical Research: Solid Earth*, *129*(4), 1–16. https://doi.org/10.1029/2023JB028509

Song, J. Y., Cattania, C., & McLaskey, G. (2025, June 2). Fault healing and asperity partitioning on a frictionally heterogeneous laboratory fault. https://doi.org/10.22541/essoar.174886019.99803345/v1

Stork, A. L., Verdon, J. P., & Kendall, J. M. (2015). The microseismic response at the In Salah Carbon Capture and Storage (CCS) site. *International Journal of Greenhouse Gas Control*, *32*, 159–171. https://doi.org/10.1016/j.ijggc.2014.11.014

Teufel, L. W., & Clark, J. A. (1984). Hydraulic Fracture Propagation in Layered Rock: Experimental Studies of Fracture Containment. *Society of Petroleum Engineers Journal*, *24*(01), 19–32. https://doi.org/10.2118/9878-PA

Wang, L., Kwiatek, G., Rybacki, E., Bonnelye, A., Bohnhoff, M., & Dresen, G. (2020). Laboratory Study on Fluid-Induced Fault Slip Behavior: The Role of Fluid Pressurization Rate. *Geophysical Research Letters*, *47*(6), 1–12. https://doi.org/10.1029/2019GL086627

Wang, L., Kwiatek, G., Renard, F., Guérin-Marthe, S., Rybacki, E., Bohnhoff, M., et al. (2024). Fault roughness controls injection-induced seismicity. *Proceedings of the National Academy of Sciences*, *121*(3), 2017. https://doi.org/10.1073/pnas.2310039121

Wu, B. S., & McLaskey, G. C. (2018). Broadband Calibration of Acoustic Emission and Ultrasonic Sensors from Generalized Ray Theory and Finite Element

Models. *Journal of Nondestructive Evaluation*, *37*(1), 1–16. https://doi.org/10.1007/s10921-018-0462-8

Wu, G., Zhang, K., Wang, C., & Li, X. (2023). Nucleation Mechanism and Rupture Dynamics of Laboratory Earthquakes at Different Loading Rates. *Applied Sciences*, *13*(22), 12243. https://doi.org/10.3390/app132212243

Yang, Y., Yang, H., & Zi, J. (2023). Stress transfer outpaces injection-induced aseismic slip and triggers seismicity. *Scientific Reports*, *13*(1), 1–12. https://doi.org/10.1038/s41598-023-43760-0

Ye, Z., & Ghassemi, A. (2018). Injection-Induced Shear Slip and Permeability Enhancement in Granite Fractures. *Journal of Geophysical Research: Solid Earth*, *123*(10), 9009–9032. https://doi.org/10.1029/2018JB016045

Yuan, C., Cochard, T., Denolle, M., Gomberg, J., Wech, A., Xiao, L., & Weitz, D. (2024). Laboratory Hydrofractures as Analogs to Tectonic Tremors. *AGU Advances*, *5*(1), 1–15. https://doi.org/10.1029/2023AV001002

Zhai, G., Shirzaei, M., Manga, M., & Chen, X. (2019). Pore-pressure diffusion, enhanced by poroelastic stresses, controls induced seismicity in Oklahoma. *Proceedings of the National Academy of Sciences*, *116*(33), 16228–16233. https://doi.org/10.1073/pnas.1819225116

Zhao, Y., Zhang, Y., Yang, H., Liu, Q., & Tian, G. (2022). Experimental study on relationship between fracture propagation and pumping parameters under constant pressure injection conditions. *Fuel*, *307*(May 2021), 121789. https://doi.org/10.1016/j.fuel.2021.121789

Zoback, M. D., Rummel, F., Jung, R., & Raleigh, C. B. (1977). Laboratory hydraulic fracturing experiments in intact and pre-fractured rock. *International Journal of Rock Mechanics and Mining Sciences & Geomechanics Abstracts*, *14*(2), 49–58. https://doi.org/10.1016/0148-9062(77)90196-6

CHAPTER 6

Conclusions

The primary objective of this dissertation was to utilize acoustic emission (AE) monitoring to investigate the mechanisms of fracture and seismicity across scales. The study spanned from detecting and quantifying microstructural defects in additive manufacturing materials to observing stick-slip behavior and rupture propagation in laboratory earthquake faults. AE techniques including signal identification, signal quantification, and source localization were applied to link these observations to underlying physical processes.

Chapter 2 established that AE sensors can reliably detect and quantify cracks in additive manufacturing materials, linking AE signals to physical processes. Chapter 3 demonstrated that AE monitoring distinguishes between aseismic, periodic, and non-periodic slip of a single VW asperity, providing experimental validation for slip modes from the previous simulation studies. Chapter 4 showed that AE recordings capture clustered seismicity across multiple VW patches, revealing back-propagating foreshock sequences, as observed in natural subduction zones, and displaying opposite fault behavior to the commonly observed fault behavior in a single VW patch. Chapter 5 revealed that AE monitoring can differentiate pressure-driven and volume-driven migration of fluid injection-induced seismicity, offering mechanistic insight for fluid injection strategies. While these studies demonstrate the utility of AE monitoring, certain limitations still remain. In additive manufacturing, for example, AE signals from pore formation were not detectable; similarly, in laboratory earthquakes,

observed aseismic slip may correspond to slow slip in natural earthquakes. This limitation could be addressed by using sensors capable of detecting low-frequency signals down to a few Hz, which would likely provide more detailed insights.

Despite these limitations, this dissertation demonstrates that AE monitoring is a versatile technique for investigating failure processes across scales, bridging material science and geophysics. Laboratory earthquake experiments offer insights into earthquake dynamics and potential early warning, while AE monitoring during additive manufacturing highlights opportunities for integrated quality assurance. By advancing methodological approaches and mechanistic understanding, this work establishes AE techniques as a robust tool for failure analysis and provides a foundation for further research in failure assessment and hazard mitigation.